Electron Microscopy and Optical Spectroscopy Analyses of Carbon Nanotube Composite Electrodes for Dye-Sentisized Solar Cells

A. Chindaduang¹, T. Sawatsuk¹, W. Wongsukkab¹, C. Sae-kung² G. Tumcharern¹ and S. Pratonetep^{1*}

National Nanotechnology Center (NANOTEC), NSTDA, 111 Thailand Science Park,
Phathumthani Rd, Klong 1, Klong Luang, Pathumthani 12120, Thailand

Institute of Solar Energy Technology Development (ISET), 111 Thailand Science Park,
Paholyothin Rd, Klong 1, Klong Luang, Pathumthani 12120, Thailand
e-mail: sirapat@nanotec.or.the-mail: sirapat@nanotec.or.th

Abstract

Photovoltaic devices based on dye-sensitized solar cells (DSSCs) have attracted great attention owing to their prospect of high energy conversion efficiency and low production cost. The power conversion efficiency and the long term stability have been reported to be improved by incorporating carbon nanotubes (CNTs) into the front electrode. However, methods to fabricate electrodes made of carbon nanotube composites are often high in cost, e.g. chemical vapour deposition (CVD), or involve some complicated procedures, e.g. functionalization of CNTs with titanium dioxide (TiO₂). Here we report morphological and optical characterizations of DSSC composite electrodes composed of multi-walled carbon nanotubes (MWCNTs) and TiO₂. The composite electrodes were fabricated by a direct mixing method with aid of organic surfactants. The electrodes containing MWCNTs of 0.025% by weight enhanced the power conversion efficiency by a factor of 1.42, under the Air Mass 1.5 illumination standard for an active area of 0.36 cm². The morphology and the composition of the films were characterized by the Field-Emission Scanning Electron Microscope (FE-SEM) as well as the Raman Spectroscopy and Microscopy. The optical transparency of the composite films was revealed by the optical absorption spectroscopy. The SEM results indicate that the increase in the electrode active surface area induced by the MWCNTs is not sufficient to account for the DSSC efficiency improvement, of which the mechanism should be best explained by the improved conductivity of the films from the MWCNTs additives. On the contrary, with MWCNTs additives of over 1%, the conversion efficiency decreases gradually, which seems to result from a poor optical transparency of the composite films.

Background

Carbon nanotubes (CNTs) have been attracting considerable attention due to their unique properties, such as good electrochemical stability, low resistivity and high surface area [1-4]. CNTs play a crucial role in varieties of applications, for example, in field emission displays [5], energy storage devices [6], electrochemical capacitors [7] as well as energy conversion devices such as dyesensitized solar cells (DSSCs) [8].

There has been some interest in the incorporation of CNTs in each component of DSSCs to improve the performance, however, with limited success. The presence of CNTs in TiO_2 matrix [9] or ionic liquid electrolyte [10] shows some improvement in the power conversion efficiency. Most reports in the literature required the well-align carbon nanotubes fabricated by a high cost vacuum-based technique such as reactive sputtering or Chemical Vapour Deposition (CVD) [11].

Here we report a simple method to improve the DSSCs performance by the incorporation of multi-walled carbon nanotubes (MWCNTs) into the front electrode using a direct mixing method. The

morphology of TiO₂-MWCNTs film was observed by Field Emission Scanning Electron Microscope (FE-SEM). The presence of MWCNTs into the film was confirmed by the Raman Spectroscopy and Microscopy. The optical transparency of the composite films was characterized by the optical absorption spectroscopy.

Materials and Methods

All chemicals are commercially available and were used without further purification unless otherwise stated. MWCNTs were kindly provided by Bayers Materials. Indium-doped tin oxide (ITO) conductive glasses were purchased from Bangkok Solar Cell Ltd (sheet resistance: 10 Ω /square). The power conversion efficiency of DSSCs was measured from photocurrent-voltage characteristics with a transient photocurrent under the AM 1.5 irradiation (100 mW cm⁻²). Optical absorption spectra were obtained by the Perkin Elmer Lambda 650. Raman spectra and Raman images were recorded in the direct reflection mode from the sample surface using by the NTMDT Ntegra spectra system with a 632.8 nm excitation.

The images were recorded using a 60X objective. FE-SEM images were taken by the Hitachi S-4700 SEM.

Preparation of TiO₂-MWCNT Electrodes

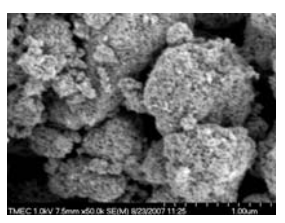
Mixtures of 0-10 wt.% MWCNTs and TiO₂ were dispersed in terpineol by ultrasonication. DSSCs front electrodes were prepared by printscreening the mixtures on ITO glass substrates with an active area 0.36 cm². The TiO₂-MWCNTs composite films were obtained after annealed at 500 °C for 2 hours.

Fabrication of DSSCs using TiO₂-MWCNTs as the Front Electrode

The TiO_2 -MWCNTs films were soaked in an ethanol solution of $Ru(II)L_2(NCS)_2$:2TBA (L = 2,2'-bipyridyl-4,4'-dicarboxylate, TBA = tetrabutylammonium). Pt-coated ITO glass substrates were used as the counter electrode. The acetonitrile solution of LiI, I_2 , 1-methyl-3-propylimidazolium iodide, and 4-*tert*-butylpyridine was used as an electrolyte.

Results and Discussion

Figure 1 displays the FE-SEM images of the annealed TiO2 films with no MWCNT and those with 10 wt.% of MWCNTs. Except for the observation of sparely segregated tubular structures in figure 1 (b), both FE-SEM images display similar porous materials of TiO₂. This implies that the incorporation of MWCNTs does not strongly affect on the surface area of the electrodes. Raman spectra confirm the presence of TiO2 and CNTs in the prepared front electrodes. Three Raman peaks at approximately 395, 518, and 642 cm⁻¹ indicate the anatase form of TiO2, while the other three peaks at approximately 1348 and 1624 cm⁻¹ represent the D and G lines of MWCNTs, respectively (figure 2). Raman images (10 x 10 μm²) of the MWCNTs-TiO₂ composite films were displayed in figure 3.



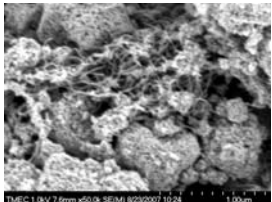


Fig. 1 FE-SEM images of (a) conventional TiO_2 and (b) TiO_2 -MWCNTs (at 10%wt concentration) front electrodes.

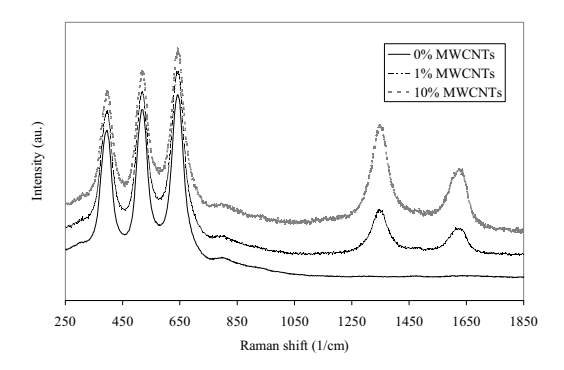


Fig. 2 Raman spectra of conventional ${\rm TiO_2}$ and ${\rm TiO_2}$ -MWCNTs front electrodes.

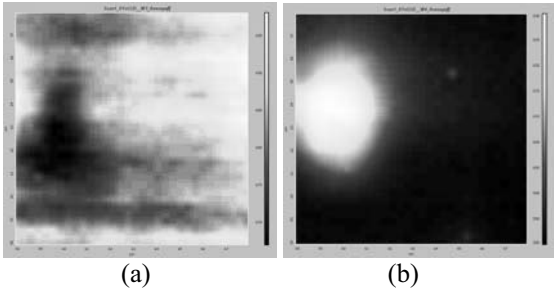


Fig. 3 Raman images of (a) conventional TiO₂ and (b) TiO₂-MWCNTs front electrodes.

The *J-V* characteristics of the DSSCs under the AM 1.5 illumination standard with an active area of 0.36 cm² are reported in Table 1. In the best conditions, the incorporation of MWCNTs at 0.025 wt%) in TiO₂ film increases the conversion efficiency by approximately 50 %, compared to the conventional DSSCs,. Further increase in the amount of MWCNTs resulted in a gradual decrease in the power conversion efficiency, owing to losses in optical transparency of the electrodes as shown by the optical absorption spectra (figure 3).

Table 1. *J-V* characteristics of TiO₂-MWCNTs front electrode of the DSSCs. Voc, Jsc and FF are the open-circuit voltage, the short-circuit current and the filling factor of the DSSCs, respectively.

MWCNTs (Wt.%)	Voc (V)	Jsc (mA/cm ²)	FF	Efficiency (η)
0.000	0.77	5.95	0.73	3.33
0.025	0.80	8.45	0.84	5.67
0.050	0.79	6.40	0.74	3.73
0.075	0.77	6.69	0.67	3.43
0.100	0.76	6.04	0.61	2.79
0.200	0.72	5.01	0.67	2.41
0.300	0.69	6.46	0.53	2.35
0.500	0.68	5.53	0.60	2.26
1.000	0.58	6.14	0.46	1.63
10.000	0.36	2.50	0.39	0.35

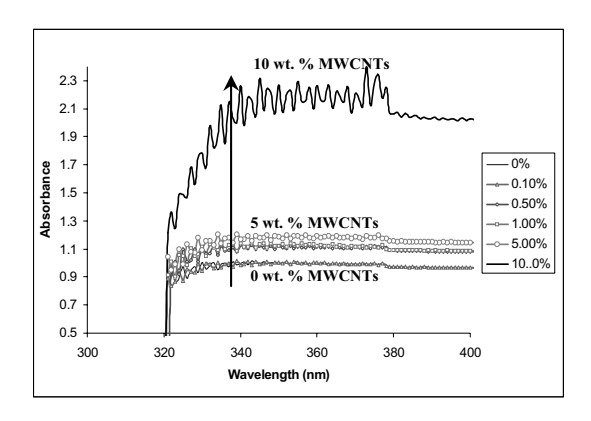


Fig. 3 Optical absorption spectra of TiO_2 films containing 0-10 wt.% of MWCNTs.

Conclusion

We have demonstrated the improvement of the power conversion efficiency of DSSCs by the incorporation of MWCNTs in the TiO_2 front electrode using a direct mixing method. At the best conditions, the TiO2-MWCNTs DSSCs attained in the short-circuit current density of 8.45 mA/cm², leading to the overall power conversion efficiency of 5.67% under the AM 1.5 illumination standard with an active area of 0.36 cm². FE-SEM, Raman spectroscopy as well as Raman microscopy confirmed the presence of MWCNTs in the TiO₂ active layer. The optical absorption measurements of the films suggest that an excess amount of MWCNTs in the electrode lead to degradation of the DSSC performance due to optical transparency losses. Future work should focus on further optimization of the MWCNT DSSC fabrication processes and detailed studies of the mechanisms for the power conversion efficiency enhancement.

Acknowledgment

The authors are grateful for the research funding from the Institute of Solar Energy Development (National Science and Technology Development Agency, Thailand) and also would like to thank Mr. Matthias Hanusch for the supplied of synthezed imidazole.

- 1. Ijima, S. Helical microtubules of graphitic carbon. *Nature* 1991, 354: 56-58.
- 2. Wang, J. Carbon-nanotube based electrochemical biosensors: A review. *Electroanalysis* 2005, 17: 7-14.
- 3. Kay, A. and Grätzel. M. Low cost photovoltaic modules based on dye sensitized nanocrystalline titanium dioxide and carbon powder. *Solar Energy Materials and Solar Cells* 1996, 44: 99-117.
- 4. Kim, H. J., Lee, D. Y. Koo, B. K. Lee, W. J. and Song. J. S. Preparation of CNT electrodes for enhanced electrochemical properties. *Proceedings of the KIEEME Annual Conference* 2004, 17: 1090.
- 5. De Heer, W. A., Châtelain, A. and Ugarte, D. A carbon nanotube field-emission electron source. *Science* 1995, 270: 1179-1180.
- 6. Che, G., Lakshmi, B. B., Fisher, E. R. and Martin, C. R. Carbon nanotube membranes for electrochemical energy storage and production. *Nature* 1998, 393: 346-349.
- Niu, C., Sichel, E. K., Hoch, R., Moy, D., and Tennent, H. High power electrochemical capacitors based on carbon nanotube electrodes. *Applied Physics Letters* 1997, 70: 1480-1482.
- O' Regan, B. and Grätzel. M. A low cost, highefficiency solar cell based on dye sensitized colloidal TiO₂ films. *Nature* 1991, 353: 737-740.
- 9. Vincent, P., Brioude, A., Journet, C., Rabaste, S., Purcell, S. T., Le Brusq, J. and Plenet, J. C. Inclusion of carbon nanotubes in a TiO sol-gel matrix. *Journal of Non-Crystalline Solids* 2002, 311: 130-137.
- 10. Park, N. -G., Van De Lagemaat, J. and Frank, A. J. Comparison of dye-sensitized rutile- and anatase-based TiO solar cells. *Journal of Physical Chemistry B* 2000, 104: 8989-8994.
- 11. Park, Y -J.; Park, S -C.; Jung, W -C.; Nam, J -G.; Kim, H –J. *US patent (Patent application)*, US2006/0137741 A1.

A Microstructural Investigation of Al-doped ZnO Films Prepared by Spray Pyrolysis

Chanipat Euvananont ¹, Supattra Pakdeesathaporn², Pawilas Pratoomwan², Visittapong Yodsri¹,

Yot Boontongkong¹, Chanchana Thanachayanont^{1*}, and Chris Boothroyd³

Abstract

Aluminum-doped ZnO (ZnO:Al) films have been prepared by spray pyrolysis using zinc acetate in methanol as a precursor solution and AlCl₃ as a dopant. It was found that all films exhibited a preferred crystallographic orientation. The average crystallite sizes calculated from X-ray diffraction data ranged from 19 to 22 nm, while dark-field TEM images exhibited individual crystallites ranging from approximately 10 to 100 nm in size. Scanning electron micrographs revealed porous film structures comprising petal-shaped grains, most of which were significantly larger than the calculated crystallite sizes, indicating that such grains comprise multiple crystallites. Any effects of the Al doping concentration on the crystal structure or the microstructure of the ZnO films were not apparent from our current results, however.

Background

During the past few decades, there has been a great demand for transparent conducting oxide (TCO) films, especially from the electronic industry. The TCO films have been used in various applications, e.g. solid state gas sensors, transparent electrodes for displays, heat mirrors, and window layers in heterojunction solar cells [1-4]. Compared with tin oxide (SnO₂) used in dyesensitized solar cells and indium tin oxide (ITO) used in polymer solar cells, zinc oxide (ZnO) is used in amorphous and microcrystalline silicon solar cells due to its stability in hydrogen plasma which is the process environment used for this application [5]. ZnO is an n-type semiconducting oxide of the group II metal zinc, and belongs to the P6₃mc space group [6]. The undoped ZnO has high n-type conductivity due to defects such as oxygen vacancies and Zn interstitials, which form donor levels [7]. Group IIIa elements (Al, Ga, In) have been used to improve the electrical conductivity and thermal stability of ZnO films. For this work, Al3+ substitution on Zn2+ was chosen due to the small ion size of Al^{3+} compared to that of Zn^{2+} ($r_{Al}^{3+}=0.054$ nm and $r_{Zn}^{2+}=0.074$ nm).

Various deposition techniques have been used to grow ZnO thin films, such as sputtering [8], pulsed laser deposition [9], and spray pyrolysis [10]. Among several techniques used to obtain high-quality undoped and doped ZnO thin films, the spray pyrolysis method has the advantages of low cost, ease of operation, and the possibility to coat large surfaces in mass production. The influence of experimental parameters such as precursor concentration, deposition temperature,

deposition time, doping concentration, and growth rate on the morphology, conductivity, and optical transmittance of ZnO films have been investigated in order to obtain thin uniform films of the necessary quality for optoelectronic devices [11,12]. In the present study, the Al doping concentration was varied from 0 to 1.0% in order to investigate the potential effect of the Al content on the microstructure of the ZnO films.

Materials and Methods

ZnO films were prepared by the spray pyrolysis method, using a 0.05M solution of zinc acetate dihydrate (Aldrich, cat. No. 22,335-2) in methanol (MERCK, AR grade) as the precursor [13]. Aluminum-doped series were produced by adding AlCl₃ at concentrations of 0.1, 0.3, 0.5, 0.7 and 1.0 % (atomic) to the precursor solution. Compressed air was used as the carrier gas at a flow rate of 1 liter/min. Prior to deposition, the hot plate-backed substrate was heated to 430°C. The precursor solution was atomized into fine droplets and carried upwards to a heated substrate, which was either glass or a Si wafer (with a native oxide layer as the immediate surface). Spray pyrolysis was then carried out for 1 hour to obtain each film, after which the substrate was allowed to cool to room temperature before further analysis. The crystal structures of the ZnO films were studied with Xray diffraction (Rigaku TTRAX III x-ray diffractometer), employing $CuK_{\alpha 1}$ operating at 50 kV & 300 mA, with a scanning speed of 2°/min at a 2θ step of 0.02°. The microstructures were examined using FE-SEM

¹ National Metal and Materials Technology Center, 114 Thailand Science Park Paholyothin Rd., Klong 1, Klong Luang, Pathumthani 12120, Thailand

² Department of Materials Engineering, Kasertsart University, Bangkok 10900, Thailand

³ Institute of Materials Research and Engineering, 3 Research Link, 117602 Singapore e-mail: chanchm@mtec.or.th

(JEOL-JSM 6301F, 20 keV), TEM (JEOL 2010, 200 keV), and high-resolution TEM (Philips CM300 FEG, 300 keV).

Results and Discussion

The spray pyrolysis process (pyrolytic decomposition of atomized droplets of the precursor solution on a heated substrate) results in the deposition of mostly transparent ZnO films. Figure 1 shows a representative example of the optical transmittance spectra obtained from our ZnO films deposited onto glass substrates.

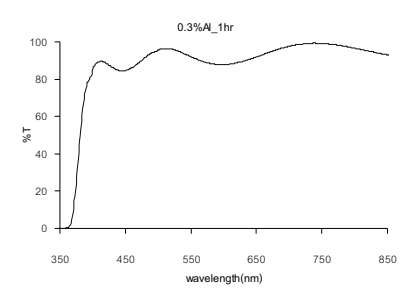


Fig. 1 Optical transmittance of a ZnO film with 0.3% Al doping concentration.

The X-ray diffraction patterns in figure 2 indicate a polycrystalline hexagonal (wurtzite) structure for the deposited films which matches the standard ZnO diffraction pattern [14]. Previous studies have reported the prevalence of the (002) planes observed for undoped and Al-doped ZnO films deposited on glass substrate by spray pyrolysis [15, 16]. Consistently, a preferred orientation of the (002) planes parallel to the substrate was also observed in our ZnO films grown on native oxide-coated Si wafer.

Figure 3 shows the average crystallite sizes of the sample series calculated based on the X-ray diffraction data and calculated using the Scherrer formula:

$$I = \frac{0.9\lambda}{\beta \cos \theta}$$

where β is the observed angular width at half maximum intensity (FWHM) of each diffraction peak located at a peak position 2θ , and λ is the X-ray wavelength. The average crystallite sizes range from 19 nm to 22 nm. However, figure 3 shows no particular trend in crystallite size variation with increasing aluminum doping concentration. This is in contrary to previous reports by Hichou et al. [15] and Allah et al. [17], which showed that a higher doping concentration of Al doping (2-4%) led to decreasing crystallite sizes.

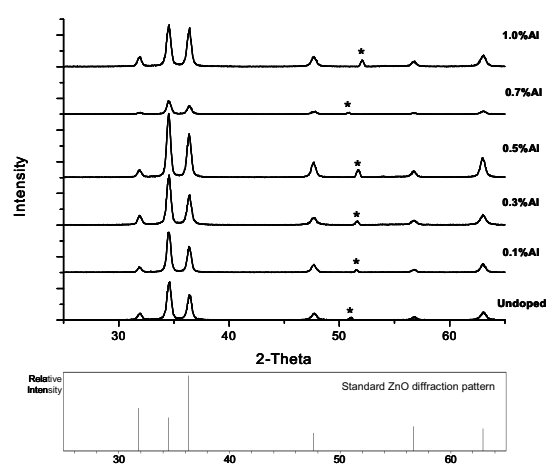


Fig. 2 X-ray diffraction patterns from pure and Al-doped ZnO films (top) and the standard ZnO diffraction pattern (bottom). (* Designates peaks from the silicon substrate.)

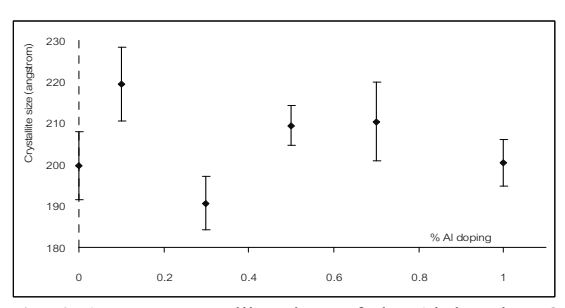


Fig. 3 Average crystallite sizes of the Al-doped ZnO films series calculated from the respective X-ray diffraction patterns.

Plan-view SEM investigation (figure 4) reveals a porous structure of the ZnO films with Al doping concentrations of 0, 0.1, 0.3, 0.5, 0.7, and 1.0at%, respectively. Petal-shaped grains of various sizes were observed all samples. The majority of these grains appear several times larger than the average crystallite sizes calculated from X-ray diffraction data (19-22 nm); thus, indicating that most of the grains comprise multiple crystallites. No systematic variation in the microstructure of the ZnO films as a function of the doping concentration was detected.

Figure 5 shows bright-field and dark-field TEM images taken from an undoped ZnO film. The crystallites within the undoped ZnO film are not uniform, with sizes varying from around 10 to 100 nm, whereas the average crystallite size obtained from XRD result is 20 nm. Similarly non-uniform crystallite sizes were observed for all other doped samples in the series, see figure 6 for example. Figure 7 shows a high-resolution transmission electron micrograph of the 1% Al-doped ZnO sample, wherein overlapping crystallites of various sizes are present.

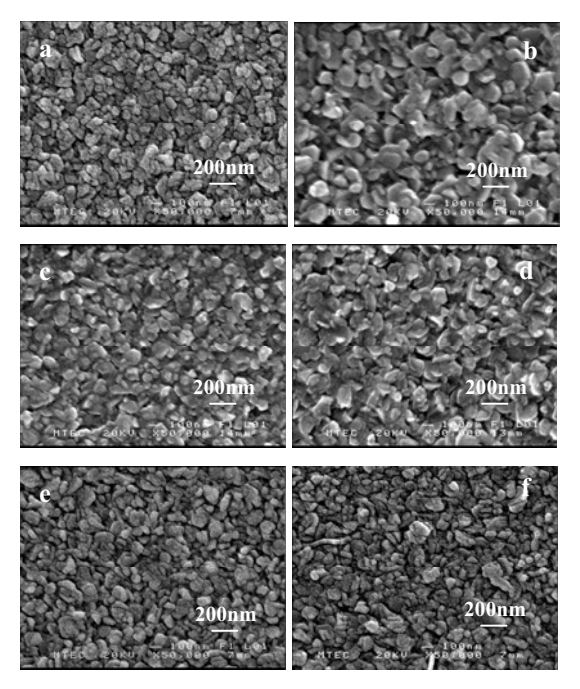


Fig.4 Plan-view scanning electron micrographs of ZnO films containing (a) 0%, (b) 0.1%,(c) 0.3%, (d) 0.5%, (e) 0.7%, and (f) 1.0% Al.

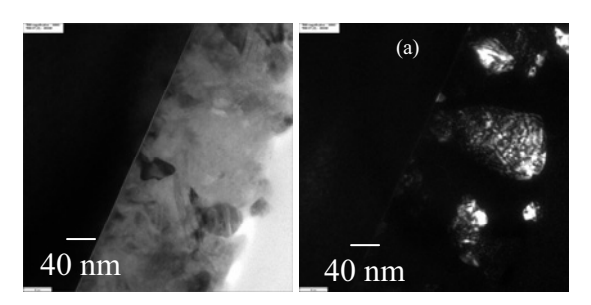


Fig. 5 (a) bright-field and (b) dark-field TEM micrographs from the undoped ZnO film.

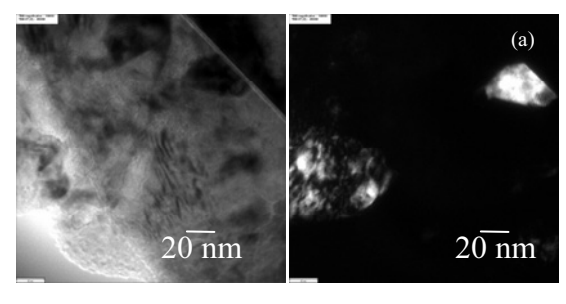


Fig. 6 (a) bright-field and (b) dark-field TEM micrographs from the 0.5% Al-doped ZnO film.

Conclusion

Aluminum-doped ZnO films with Al concentrations up to 1.0% have been prepared by spray pyrolysis from zinc acetate solutions in methanol, using AlCl₃ as the dopant. X-ray diffraction indicates a preferred c-axis orientation perpendicular to the substrate in all samples of the series, while the calculated average crystallite sizes range from 19 to 22 nm. SEM micrographs reveal porous film structures comprising petal-shaped

grains that are significantly larger than the calculated crystallite sizes. However, no apparent effects of the Al doping concentration on the crystal structure or the microstructure of the ZnO films were found. Further work is underway to investigate the reproducibility of our current results, as well as to characterize the electrical properties of these Al-doped ZnO films.

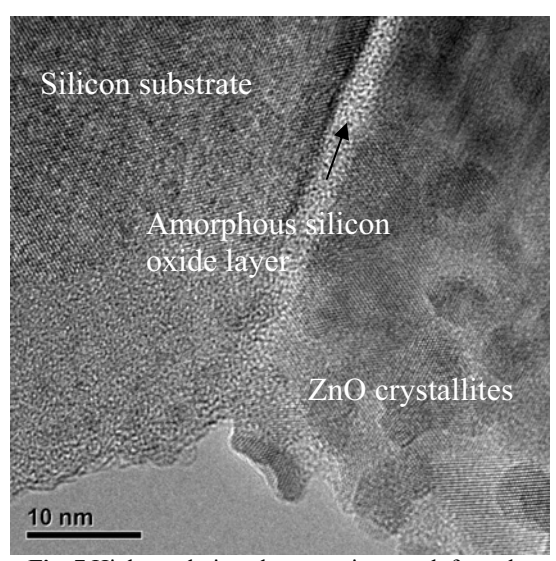


Fig. 7 High-resolution electron micrograph from the 1.0% Al-doped ZnO film.

Acknowledgment

The authors would like to thank the National Metal and Materials Technology Center for financial support (MTEC Grant No. MT-B-48-CER-07-187-I) and Miss Onuma Santawitee for her help with SEM imaging.

- 1. Stambolova I, Konstantinov K, Vassilev S, Peshev P, Tsacheva T S. High transmittance and low resistive AZO films for thin film solar cells. *Mater. Chem. Phys.* 2000, 63: 104-108.
- 2. Chen M, Pei Z L, Sun C, Gong J, Huang R F, Wen L S. ZnO: an attractive potential substitute of ITO in flat display panels. *Mater. Sci. Eng. B* 2001, 85: 212-217.
- 3. Chopra K L, Major S, Pandya D K. Properties of InGaN deposited on Glass at Low Temperature. *Thin Solid Films* 1983, 102: 1-46.
- 4. Jin Z-C, Hamberg I, Gradqvist C G, Sernelius B E, Berggren K-F. Reactively sputtered AZO films for energy-efficient windows. *Thin Solid Films* 1988, 164: 381-386.
- 5. Major S, Kumar S, Bhatnagar M and Chopra K L. Effect of hydrogen plasma treatment on transparent conducting oxides. *Appl. Phys. Lett.* 1986, 49: 394-396.
- 6. Steiner, T. Semiconductor Nanostructures for Optoelectronic Applications, *Artech House, Inc.*, 2004.

- 7. Look D C, Hemsky J W, Sizelove J R. Residual Native Shallow Donor in ZnO. *Phys. Rev. Lett.* 1999, 82: 2552-2555.
- 8. Tominaga K, Umezu N, Mori I, Ushiro T, Moriga T, Nakabayashi I. Transparent conductive ZnO film preparation by alternating sputtering of AZO and Zn or Al targets. *Thin Solid Films* 1998, 334: 35-39.
- 9. Khandelwal R, Singh A P, Kapoor A, Grigorescu S, Miglietta P, Evgenieva N S, Perrone A. Effects of deposition temperature on the structural and morphological properties of thin ZnO films fabricated by pulsed laser deposition. *Optics & Laser Technology* 2008, 40: 247–251.
- 10. Ootsuka T, Liu Z, Osamura M, Fukuzawa Y, Kuroda R, Suzuki Y, Otogawa N, Mise T, Shinan W, Hoshino Y, Nakayama Y, Tanoue H, Makita Y. Studies on aluminum-doped ZnO films for transparent electrode and antireflection coating of h-FeSi2 optoelectronic devices. *Thin Solid Films* 2005, 476: 30–34.
- 11. Choi B G, Kim I H., Kim D H, Lee K S, Lee T S, Cheong B, Baik Y-J., Kim W M. Electrical, optical and structural properties of transparent and conducting ZnO thin films doped with Al and F by rf magnetron sputter. *Journal of the European Ceramic Society* 2005, 25: 2161–2165.
- 12. Joseph B, Manoj P K, Vaidyan V K. Studies on the structural, electrical and optical properties of Al-doped ZnO thin films prepared by chemical spray deposition. *Ceramics International* 2006, 32: 487–493.

- 13. Lokhande B J, Patil P S, Uplane M D. Studies on structural, optical and electrical properties of boron doped zinc oxide films prepared by spray pyrolysis technique. *Physica B* 2001, 302-303: 59-63
- 14. Powder Diffraction File, Data Card 5-644, 3c PDS International Center for diffraction Data, Swartmore, PA. +6.
- 15. Hichou A El, Addou M, Bougrine A, Dounia R, Ebothe J, Troyon M and Amrani M. Cathodoluminescence properties of undoped and Al-doped ZnO films deposited on glass substrate by spray pyrolysis. *Mat. Chem. Phys.* 2004, 83: 43-47.
- 16. Romero R, Leinen D, Dalchiele E A, Ramos-Varrado J R and Martin F. The effects of zinc acetate and zinc chloride precursors on the preferred crystalline orientation of ZnO and Aldoped ZnO thin films obtained by spray pyrolysis. *Thin Solid Films* 2006, 515: 1942-1949.
- 17. Allah F K, Abe S. Y, Nunes C M, Khelil A, Cattin L, Morsli M, Bernede J C, Bougrine A, del Valle M A and Diaz F R. Characterisation of porous doped ZnO thin films deposited by spray pyrolysis technique. *Applied Surface Science* 2007, 253: 9241-9247.
- Rozati S M and Asesteh S M. Characterization of ZnO:Al thin films obtained by spray pyrolysis technique. *Materials Characterization* 2007, 58: 319-322.

Phase Formation and Microstructure of Ba(Zr_{0.20}Ti_{0.80})O₃ Ceramics Prepared via Solid State Reaction Method

T. Bongkarn^{1*}, N. Phungjitt¹, N. Vittayakorn²

¹ Department of Physics, Faculty of Science, Naresuan University, Phitsanulok, Thailand

² Department of Chemistry, Faculty of Science, King Mongkut's Institute of Technology Ladkrabang, Bangkok, Thailand

e-mail: researchcmu@yahoo.com

Abstract

In this work, effects of calcination and sintering temperatures on phase formation and the microstructure of $Ba(Ti_{0.80}Zr_{0.20})O_3$ (BZT) ceramics were investigated. The BZT powders were prepared via a solid state reaction method under various calcination and sintering temperatures. X-ray diffraction (XRD) was used to evaluate the optimum condition for calcinations. Microstructure was studied by using scanning electron microscopy (SEM). It was found that the pure perovskite phase of BZT powder was obtained at a calcination condition of 1250 °C for 4 h. Sintered pellets showed a pure peroverskite cubic phase in all samples. Lattices parameter (a) tended to increase with increasing calcination temperatures. Microstructures of the powders exhibited an almost-spherical morphology and had a porous agglomerated form. Average particle sizes and average grain sizes increased from 0.27 to 1.48 μ m and 15.06 to 60.30 μ m when increasing calcination and sintering temperatures from 800 to 1350 °C and from 1400 to 1600 °C, respectively. Dielectric constant was relative with the density of the sintered ceramic.

Background

Barium titanate (BaTiO₃, BT) is well known as a fundamental ferroelectric perovskite oxide [1] and is often used in multilayer ceramic capacitors (MLCs) due to its high dielectric constant [2]. The BaTiO₃ displays dielectric anomalies at 130, 0, and -90 °C with respective transformations in symmetry from cubic to tetragonal, from tetragonal to orthorhombic orthorhombic, and from rhombohedral, respectively. Those anomalies are accompanied by a high dielectric constant near the phase transition [3]. Nature and phase transition temperature of BT can be modified via partial substitution of either Ba ions (A-site doping) or Ti ions (B-site doping). A-site doping with cations of the same valence as Ba causes the Curie temperature (T_c) (~ 130 °C) to either decrease (Sr substitution) or increase (Pb substitution) without any significant broadening of the transition [4]. With B-site doping, ferroelectric domains, which are associated with a cooperative off-center displacement of Ti⁴⁺ ions in their TiO₆ octahedra, are disrupted, which often lead to a broadening of the transition at T_c. Partial replacement of titanium by tin or hafnium generally leads to a reduction in T_c and an increase in the permittivity maximum with dopant content [5].

Barium zirconate titanate ($Ba(Zr_xTi_{1-x})O_3$, BZT) is obtained by substituting ions at the B site of $BaTiO_3$ with Zr ions. This substitution results in a

decrease in the temperature and a broadening of the permittivity maximum [6]. Brajer and Kulscar showed that, as the zirconium content increases, the orthorhombic-tetragonal phase transition temperature increases and the tetragonal-cubic phase transition temperature decreases [7,8]. At a Zr/Ti ratio greater than 0.10, the three dielectric constant peaks coalesce into a single broad maximum [9]. Moreover, the transition temperature of the BZT shifts to a lower temperature region with the increase of the Zr contents. The dielectric study of the Ba(Zr_xTi_{1-x})O₃ ceramics with x=0.20 and 0.25 showed a normal ferroelectric with weak diffuse phase transition behaviors [10]. Diffuse phase transition and a relaxor-like behavior were found at higher Zr contents (x=0.30 and 0.35). High tunability and dielectric loss of the $Ba(Zr_xTi_{1-x})O_3$ with x=0.20 ceramic, measured at room temperature under the biasing field 20 kV/cm, are 82% and 0.0034, respectively [11]. This makes the Ba(Zr_{0.20}Ti_{0.80})O₃ ceramics a promising material for ceramic capacitors. However, to the author's best knowledge, no phase formation and microstructure of BZT ceramics prepared by the solid state reaction method have been reported yet. Therefore, in the present work, the phase formation and the microstructure of the Ba(Zr_{0.20}Ti_{0.80})O₃ ceramics prepared via solid state reaction method was studied.

Materials and Methods

Starting materials were commercially available barium carbonate, BaCO₃ (99%) titanium (IV) oxide, TiO₂ (99%) and zirconium (IV) oxide, ZrO₂ Barium (99%). zirconate titanate (Ba(Zr_{0.20}Ti_{0.80})O₃, BZT) powder was synthesized solid state reaction of thoroughly ground mixtures of BaCO₃, TiO₂ and ZrO₂ powders by a ball milling procedure (zirconia milling media under ethanol for 24 h). Drying was carried out at 120 °C for 4 h. After sieving, various calcination temperatures, ranging from 800 to 1350 °C, with a dwell time of 4 h. and heating/cooling rate of 5 °C/min, were performed. The calcined powders were then pressed into disks with a diameter of 15 mm at a pressure of 40 MPa. The pellets were sintered from 1400 to 1600 °C for 2 h and cooled in a furnace. For electrical measurements, silver paste was fired on both sides of the polished samples at 500 °C for 30 min and used as electrodes.

X-ray diffractometer (XRD; Philip PW3040/60 X' Pert Pro) were employed to identify the phase formed and optimum temperature of the BZT powders and ceramics. Morphologies of the calcined powders and sintered ceramics were imaged using scanning electron microscope (SEM; LEO 1455 VP). Densities of the sintered ceramics were measured by the Archimedes method and average grain size was determined by using a mean linear intercept method. Capacitance was measured with a LCR meter (Agilent 4263B) at room temperature. Dielectric constant (\mathcal{E}_r) calculated using the geometric area and thickness of the discs.

Results and Discussion

The XRD patterns of the BZT powders formed with different calcination temperatures are given in figure 1. After calcination at 800 °C, the crystalline phase of BZT was accompanied with BaCO3 and ZrO₂ as separate phases, whose X-ray peaks matche the JCPDS file number 41-0373 [12] and 24-1165 [13]. As the temperature increased to 1000 °C, the peaks corresponding to the raw materials disappeared, while the intensity of the BaTiO₃, BaZrO₃ and Ba₂ZrO₄ peaks became minor phases, which can correlate with JCPDS file number 03-0726 [14], 06-0399 [15] and 24-0130 [16] respectively. After calcination at 1200 °C, the peaks corresponding to BaTiO3, BaZrO3 and Ba₂ZrO₄ were not detectable. Evidently, a single phase of BZT is formed by calcination at 1250 °C.

The strongest reflections in the majority of the XRD patterns indicate the formation of the perovskite phase of BZT, which can be matched with the JCPDS file number 36-0019 [17]. To a first approximation, this phase is a cubic perovskite type structure.

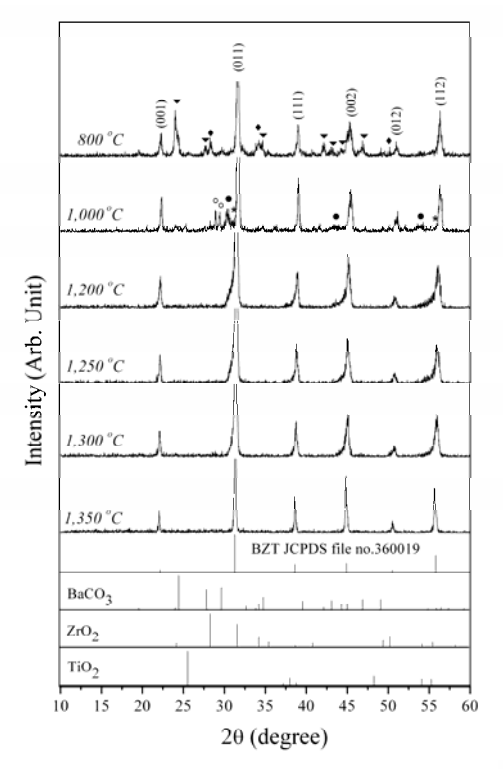


Fig.1 XRD patterns of $Ba(Zr_{0.20}Ti_{0.80})O_3$ powders: (\checkmark) $BaCO_3$; (\checkmark) ZrO_2 ; (\bullet) $BaZrO_3$; (\circ) Ba_2ZrO_4 ; (*) $BaTiO_3$.

Percentage of the perovskite phase of BZT powders as a function of calcination temperatures was calculated. The perovskite phase of 800 to 1200 °C calcined samples does not reach a hundred percent. The single phase of perovskite of the calcined samples at a temperature higher than 1250 °C is formed. The percentage of the BZT perovskite phase was increased with the increase of calcination temperatures listed in Table 1.

SEM photographs of BZT powders calcined between 800 and 1350 °C are shown in figure 2. These powders exhibit an almost spherical morphology and have a porous agglomerated form. As the temperature increased, more agglomerate particles could be observed. The average particle size tended to increase as calcination temperature increased as shown in Table 1.

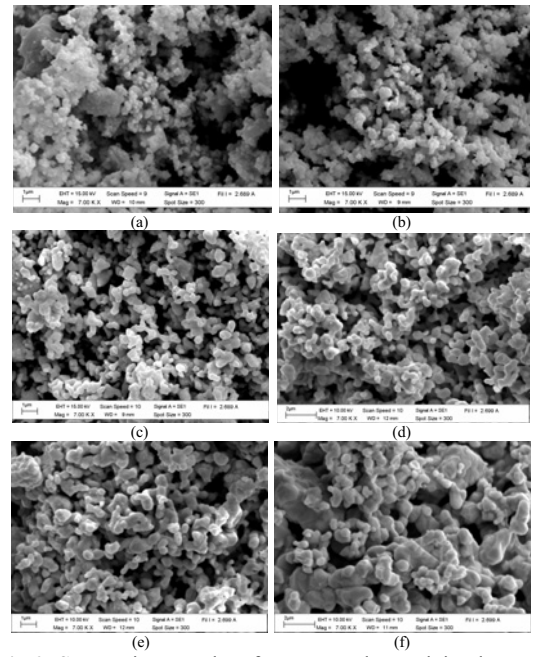


Fig.2 SEM micrographs of BZT powders calcined at (a) 800 °C, (b) 1000 °C, (c) 1200 °C, (d) 1250 °C, (e) 1300 °C and (f) 1350 °C.

Table 1 Percentage of perovskite phase and the average particle size of BZT powders.

particle size of BZT pe	711 4015.	
calcination temperature	% perovskite	average particle size
(°C)	phase	(µm)
800	70	0.3
1000	74	0.4
1200	94	0.8
1250	100	0.9
1300	100	1.1
1350	100	1.5

The phase formation behavior of the sintered ceramics is revealed by the XRD method. The XRD pattern of the BZT ceramics, with varied sintering temperatures, is shown in figure 3. This confirms that all samples were free of minor phase peaks. The BZT ceramics are identified as a single phase with a perovskite structure which has a cubic symmetry, as reported in previous investigations [18,19].

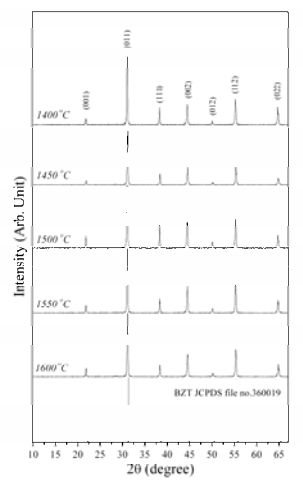
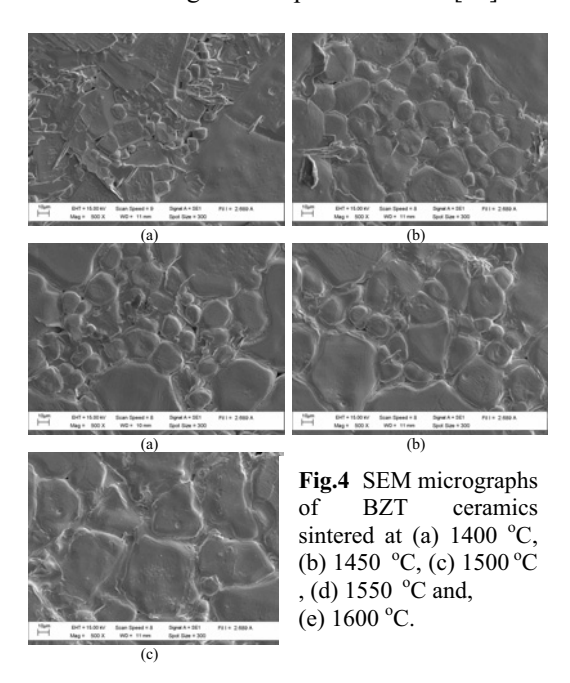


Fig.3 XRD patterns of Ba(Zr_{0.20}Ti_{0.80})O₃ ceramics.

The SEM photographs in figure 4 shows the surface of BZT ceramics at various sintering temperatures from 1400 to 1600 $^{\circ}$ C. The average grain sizes increased from 15.1 to 60.3 μ m with an increase in sintering temperature and the results also show a nonuniform distribution of grain size. These results agree with previous work [20].



The measured density and the dielectric constant at room temperature with a variation of the sintering temperatures are shown in figure 5. It can be seen that both the density and dielectric constant were first increased by sintering temperature and reached a maximum at 1500 °C and then both values were dropped when the sintering temperature was higher than 1500 °C. These results indicated that the dielectric constant is relative to the density of the ceramic.

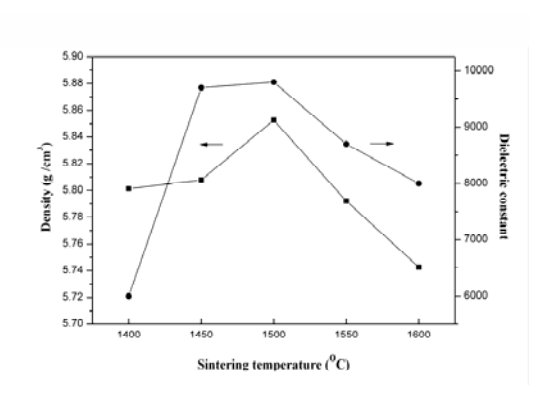


Fig. 5 Variation of dielectric constant at room temperature and density of BZT ceramics with various of sintering temperatures.

Conclusion

BZT powders can be formed through the reaction of barium carbonate, titanium (IV) oxide and zirconium (IV) oxide via calcined temperature at 1250 °C. The resulting of the BZT powders were more agglomerated as the calcination temperature increased. The BZT ceramic was identified by XRD as a single phase with a perovskite structure having cubic symmetry. The average grain size increased with an increase in sintering temperature. The maximum density and maximum dielectric constant were achieved from the ceramics sintered at 1500 °C.

Acknowledgment

This work was financial supported by the Thailand Research Fund (TRF), Faculty of Science, Naresuan University and King Mongkut's Institute of technology, Ladkrabang (KMITL). Thanks are also to the Science Lab Center, Faculty of Science, Naresuan University for facilities supporting. Acknowledgement is also given to Mr. Don Hindle for his helpful comments and correction of the manuscript.

- Clabaugh, W.S., Swiggard, R. and Gilchrist, R. Preparation of Barium Titanyl Oxalate Tetrahydrate for Conversion to Barium Titanate of High Purity. *J. Res. Nat. Bur. Stds.* 1956, 56: 289-291.
- Sakabe, Y., Minai, K. and Wakino, K. High-Dielectric Constant Ceramics for Base Metal Monolithic Capacitors. *Jpn. J. Appl. Phys. Suppl.* 1981, 20: 147-150.
- 3 Jaffe, B., Cook J., W. R. and Jaffe, H. Piezoelectric Ceramics, in Nonmetallic Solid: Series of Monographs No.3. *Academic Press, London, U.K.*, 1997, 53-57.
- 4 Nemoto, H. and Oda, I. Direct Examinations of PTC Action of Single Grain Boundaries in Semiconducting BaTiO₃ Ceramics. *J. Am. Ceram. Soc.* 1980, 63: 398-401.
- 5 Kuwabara, M., Morimo, K. and Matsunaga, T. Singer-Grain Boundaries in PCT Resistors. *J. Am. Ceram. Soc.* 1996, 79: 997-1001.
- 6 Ulrich, W., Georg, G., Ulrich, B., Sophie, W., Detlev, H. and Rainer, W. Dielectric Properties of Ba(Zr,Ti)O₃-Based Ferroelectrics for Capacitor Applications. *J. Am. Ceram. Soc.* 2001, 84: 759-766.

- 7 Brajer, E. J. Polycrystalline Ceramic Materials. U.S. Pat, 1955, No. 2 708 243.
- 8 Kulscar, F. Fired Ceramic Barium Titanate Body. U.S. Pat, 1956, No. 2 735 024.
- 9 Hennings, D., Schnell, A. and Simon, G. Diffuse Ferroelectric Phase Transitions in Ba(Ti_{1-y}Zr_y)O₃ Ceramics. *J. Am. Ceram. Soc.* 1982, 65: 539-544.
- Tang, X.G., Chew, K.H. and Chan, H.L.W. Diffuse Phase Transition and Dielectric Tunabilibty of Ba(Zr_yTi_{1-y})O₃ Relaxor Ferroelectric Ceramics. *Acta Mater.* 2004, 52: 5177-5183.
- Tang, X.G., Chew, K.H. and Chan, H.L.W. Effect of Grain Size on the Dielectric Properties and Tunabilies of Sol-Gel Derived Ba(Zr_{0.2}Ti_{0.8})O₃ Ceramics. Solid State Commun. 2004, 131: 163-168.
- 12 Powder Diffraction File No. 41-0373. International Center for Diffraction Data, Newton Square, PA, 2003.
- Powder Diffraction File No. 24-1165. International Center for Diffraction Data, Newton Square, PA, 2003.
- 14 Powder Diffraction File No. 41-0726. International Center for Diffraction Data, Newton Square, PA, 2003.
- 15 Powder Diffraction File No. 06-0399. International Center for Diffraction Data, Newton Square, PA, 2003.
- 16 Powder Diffraction File No. 24-0130. International Center for Diffraction Data, Newton Square, PA, 2003.
- 17 Powder Diffraction File No. 36-0019. International Center for Diffraction Data, Newton Square, PA, 2003.
- 18 Kbune, M., Yamakawa, K. and Yazawa, T. Barium Zirconate Titanate-Based Inorganic Dielectric Material with High Permittivity as a Lead-Free Insulator for Semiconductor Application. *Integr. Ferroelectr.*. 2005, 77: 69-78.
- 19 Verbitskaia, T.N., Zndanov, G.S., Venevtsev, I.N. and Solviev, S.P. Electrical and X-Ray Diffraction Studies of the BaTiO₃-BaZrO₃ System. *Crystallography* 1958, 3: 186-196.
- 20 Liang, R.H., Dong, X.L., Chen, Y., Cao, F. and Wang, Y.L. Dielectric Properties and Tunability of Ba(Zr_xTi_{1-x})O₃ Ceramics Under High DC Electric Field. *Ceram. Int.* 2007, 33: 957-961.

Microstructures of Dip-coated TiO₂ Thin Film Capacitor

Chanipat Euvananont¹, Jirawat Doungratsamee², Chabaiporn Junin¹, Tossapol Tippo³ and Chanchana Thanachayanont^{1*}

¹National Metal and Materials Technology Center, 114 Thailand Science Park

Paholyothin Rd., Klong 1, Klong Luang, Pathumthani 12120, Thailand

Abstract

In this paper, we investigated the effect of number of dip coating times between 1, 2 and 3 times to the capacitance properties of TiO_2 thin film capacitors. The TiO_2 thin films were directly deposited on Si substrates using dip coating technique. Single phase anatase TiO_2 dense and smooth films with small grain sizes were obtained after calcination at 450 °C for 4 hours in air. The maximum electrical capacitance obtained was 1.178 nF at 4.0 V applied voltage.

Background

Thin film capacitors are widely used in multilayer ceramic capacitors (MLCCs) and electronic integrated circuits, where they perform essential functions such as storing electric charges and blocking leakage current. For example, the MLCCs consist of ceramic dielectric layers and inner metal electrodes [1-3], which are piled up alternately leading to an equivalent circuit of several capacitors in parallel. In recent years, thin film capacitors have been predominantly used as passive component materials in electronic circuits and, in particular, they are used in most compact electronic devices, such as laptop computer, mobile phone and modern electronic gadgets.

To fabricate the dielectric thin films for thin film capacitors, titanium dioxide is a very interesting material in both of physical and chemical properties [4]. A high dielectric constant makes the material a good insulator. Stability of TiO₂ in harsh environment and elevated temperatures makes it an attractive transparent oxide semiconductor for many microelectronic applications. There have been previous attempts to prepare TiO₂ films using sol-gel technique [5-7]. In this study, the sol-gel technique via dip coating method was selected to fabricate TiO2 dielectric thin film due to main advantages of being cheap and easy to control microstructures of the films. In this study, thin TiO2 film capacitors were prepared from titanium precursor solution with various number of dipping cycles from 1 to 3 times to compare differences in film morphologies, thicknesses and its capacitive properties.

Materials and Methods

Preparation of Sol-TiO₂ Precursor Solution for Dip Coating

To obtain a stable TiO₂ sol, a precursor solution was prepared following Legrand-Buscema et al. [8]. Firstly, 0.3 M titanium- isopropoxide (TTIP, Fluka) was dissolved in isopropanol (IPA, Fluka) and stirred at room temperature for 30 mins. Then, acetylacetone (Acac, Merck) was added to make 10:3 molar ratio of titanium isopropoxide to acetylacetone. The mixture was used as chelating agent to stabilize the solution. The mixture was then stirred for 30 minutes more. Acetic acid (Labscan) was added afterwards to help initialize hydrolysis by creating esterification reaction with isopropanol. Transparent yellow solution was obtained.

Dip Coating Method Procedure

The TiO₂ precursor was used for film fabrication by dip coating technique. (1 0 0) Silicon wafer (cut into 15 x 20 x 1.5 mm³ size) was used as a substrate. The Silicon wafer pieces were ultrasonicated in DI water, acetone, ethanol and isopropanol for 15 minutes each, respectively, before dip coating in TiO₂ precursor with 1 mm./sec withdrawal speed 1, 2 and 3 times, respectively. The coated films were dried at 60 °C for 30 minutes before calcinination at 450 °C for 4 hours in air [9]. Figure 1 summarizes the film fabrication process. Aluminium electrodes were deposited using thermal evaporation both side of the TiO₂ thin film for C-V analysis measurement. Reasonably smooth and uniform TiO₂ film with the

²Department of Electronic Engineering, Mahanakorn University of Technology, Thailand

³Department of Electronic Engineering, King Mongkut Institute of Technology Ladkrabang, Thailand e-mail: chanchm@mtec.or.th

highest capacitance was selected for characterization.

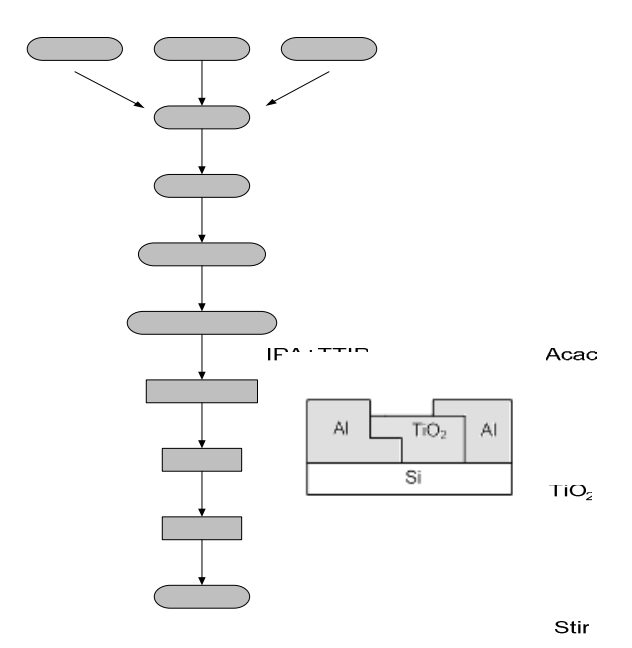


Fig. 1 Flow chart for preparation procedure of TiO_2 thin film via dip coating technique and structure of TiO_2 thin film capacitor.

Characterization

Coating Solution

Capacitive properties of TiO2 thin film capacitors were measured using C-V analyzer (Keithley CV Analyzer model 590). Morphological Eletrodes of the TiO₂ films were investigated using tapping mode Atomic Force Microscopy (AFM, Seiko instrument SPA 400) and field emission Scanning Electron Microscopy (JEOL 6321F). Film thicknesses were measured using a Dektak 3st Coating profilometer confirmed and surface Transmission Electron Microscopy (TEM, JEOL 2010FX). Crystal structures of the TiO₂ films were studied using Rigaku TTRAX III X-Drawing diffractometer (XRD). The CuKa radiation was operated at 50 kV.

Results and Discussion

Capacitance Properties

Firing

Dielectric properties of sol-gel coated TiO₂ films were studied by plotting the variation of capacitance, C, at different applied bias voltages film from 0 to 20 V with 0.05 V stepping and a frequency of 100 Hz applied across the samples. The C-V plots of the films dipped 1,2 and 3 times are shown in figure 2.

From figure 2, maximum capacitances obtained from each film were 1.072nF at 5.1 Volt, 1.060nF at 3.5 Volt and 1.178 nF at 4.0 Volt for number of dip coating 1, 2 and 3 times, respectively. The capacitance values of all the TiO_2 films are not very different because the thickness of the TiO_2 films increases only slightly with increasing

dipping cycle. The 3-time dip coated TiO₂ film was selected for characterization due to its highest maximum capacitance among the three samples.

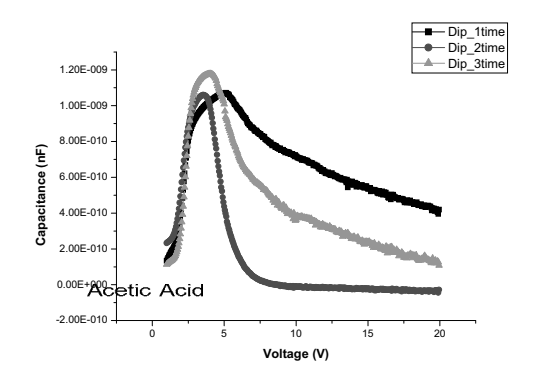


Fig.2 C-V plot of TiO₂thin film with different number of coating times

Microstructure and Thickness of the TiO₂ Films

Figure 3 shows the XRD pattern of the 3-time dip coated TiO_2 film. The result indicates that the film consists of only pure anatase phase after calcination at 450°C for 4 hours in air atmosphere. Figures 4 and 5 show surface morphologies of 3-time dip coated TiO_2 film using AFM and SEM, respectively. Uniform grain size within a range of 20-30 nm and very smooth dense film having roughness of around 1 nm were obtained.

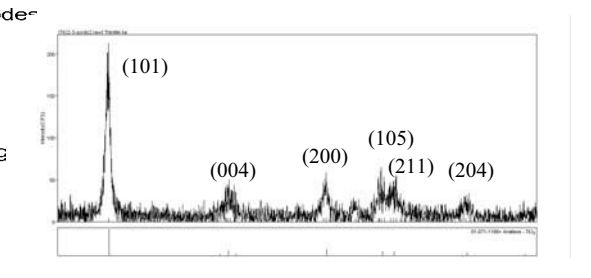


Fig.3 XRD pattern of TiO_2 film dip coating 3times after calcine at 450 °C for 4 hrs.

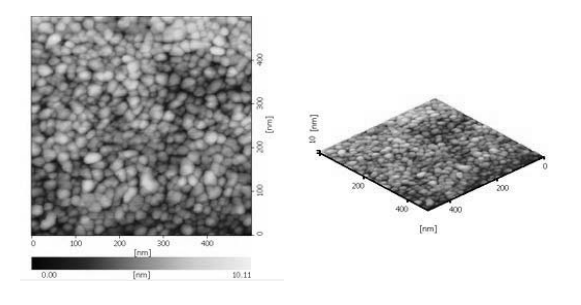


Fig.4 AFM images of surface of 3-time dip coated TiO₂ film after calcination at 450 °C.

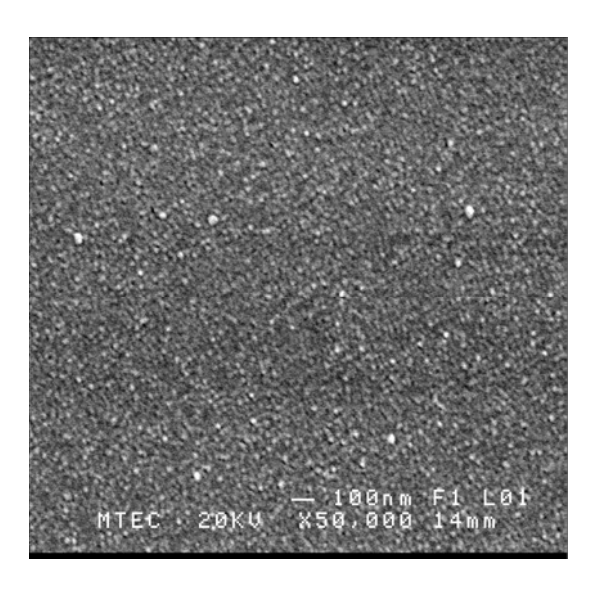


Fig.5 An SEM micrograph of the surface of 3-time dip coated TiO₂ film after calcinination at 450 °C for 4 hrs.

Figure 6 shows a cross-sectional TEM micrograph of the 3-time dip coated TiO_2 film. The result indicates that dipping titanium dioxide precursor 3 times provides single uniform TiO_2 layer after calcination. The film thickness of 78 nm was obtained. Unfortunately, we could not increase the capacitance by dipping more than 3 times to increase the film thickness because the TiO_2 film cracked and may cause leakage current when performing as a dielectric layer of the thin film capacitors.

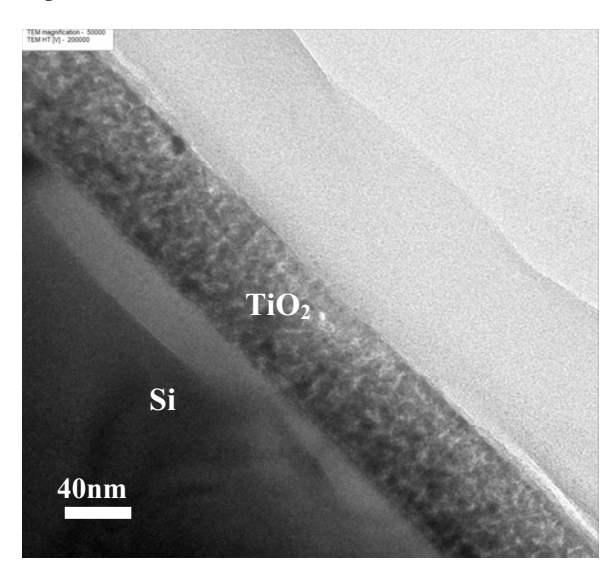


Fig.6 A cross-sectional TEM image of 3-time dip coated TiO₂ film after calcinination at 450 °C for 4 hrs.

Conclusion

Dielectric TiO_2 thin film capacitors have been prepared successfully by dip-coating the TiO_2 films from TiO_2 sol-gel precursor. The maximum capacitance was obtained from 3-time dip coated TiO_2 film because of the pure phase, thick, uniform and smooth microstructure.

Acknowledgment

Authors would like to thank the National Metal and Materials Technology Center for financial support (MTEC Grant No. MT-B-48-CER-07-187-I) and Miss Viyaporn Krongtong for her help on SEM imaging.

- 1. Hino T, Matsumoto N, Nishida M, Araki T. PLD of X7R for thin film capacitors. *Applied Surface Science* 2007, doi:10.1016/j.apsusc.2007.10.001.
- 2. Juan P C et al. The effect of annealing temperature on the electrical properties of metal-ferroelectric (PbZr0.53Ti0.47O3)-insulator (ZrO2)-semiconductor (MFIS) thin-film capacitors. *Micro Electronic Engineering* 2007, 84: 2014-2017.
- 3. Lin-Jung Wu, Jenn-Ming Wu, Thickness-dependent dielectric properties of nanoscale Pt/(Pb,Ba)ZrO₃/BaPbO₃ capacitors. *Journal of Crystal Growth*. article in press. accepted 30 August 2007.
- 4. Mo S D, Ching W Y, Electronic and optical properties of three phases of titanium dioxide: Rutile, anatase, and brookite. *Phys. Rev.* 1995, B 51 (19): 13023-13032.
- 5. Young Jin Yun et al. Low-temperature coating of sol-gel anatase thin films. *Materials Letter* 2004, 58: 3703-3706.
- 6. Cui H, Shen H S, Gao Y-M, Dwight K and Wold A. Photocatalytic properties of titanium (IV) oxide thin films prepared by spin coating and spray pyrolysis. *Materials Research Bulletin* 1993, 28 (3): 195-201.
- 7. Gao Y M, Shen H S, Dwight K and Wold A. Preparation and photocatalytic properties of titanium(IV) oxide films. *Materials Research Bulletin* 1992, 27 (9): 1023-1030.
- 8. Legrand–Buscema C, Malibert C and Bach S. Elaboration and characterization of thin films of TiO₂ prepared by sol-gel process. *Thin Solid Films* 2002, 418: 79-84.
- 9. Guillard C, Debayle D, Gagnaire A and Jaffrezic H. Physical properties and photo catalytic efficiencies of TiO₂ films prepared by PECVD and sol-gel methods. *Materials Research Bulletin* 2004, 28: 1445-1458.

Collagen Measurement and Staining Pattern of Wound Healing Comparison with Fixations and Stains

S. Ukong¹, S. Ampawong^{2*}, and K. Kengkoom³

e-mail: a sumate@hotmail.com

Abstract

Several studies have measured collagen fiber with advance imaging techniques. Unfortunately these are performed by complicated methods and with specific tools. In seeking out the easier ways in routine histopathological laboratory, collagen measurements and staining patterns of wound healing comparison with fixatives (10% Neutral Buffer Formalin; NBF and Bouin's solution) and stains (Hematoxylin & Eosin; H&E and Masson's trichrome) were observed in Sprague Dawley rat. Wound characteristics were measured running under image analysis program, ImageJ, NIH. The result showed that moderate effects of fixatives on staining intensity of collagen fiber and staining pattern were observed in healing wound. 10% NBF fixed specimens were stained on collagen fiber less intensely than Bouin's solution. However there were no effects of fixatives on basic architecture such as size and length of neovascularied vessels and epithelial tongue respectively. We preliminarily conclude that Bouin's fixative is appropriate to fix tissue for measuring collagen fiber because of its color enhancement property. The most important of our results is used to application for assessment the pharmacological products which promote new collagen fibers formation and wound healing.

Background

Histopathological studies of wound healing process are normally used for evaluation the efficacy of pharmacological products which promote dermal skin substitutes (Truong N.T and et al., 2005; Bae and et al., 2005; Roh and et al., 2006; Rao and et al., 2007). Those studies are related to phases of cutaneous wound repairing which have been divided into three phases: inflammation (early and late), proliferation, and remodeling (Clark 1996; Martin 1997). Several wound characteristics are considered to determine the level of histopatological changing e.g. the depth length of healed wound, epithelial incorporation of the stratification, substitute, degree of neutrophil, macrophage, fibroblast, and foreign body giant (FBG) cell infiltration, extent of elastin formation (Truong N.T and et al., 2005). One of the most important wound characteristic to be measured was collagen fiber (Gogly and et al., 1997; Ballas & Davidson 2001; Truong N.T and et al., 2005; Rao and et al., 2007). Because of its property, plays a dominant role in maintaining the structural integrity and healing wound (Myllyharju & Kivirikko 2001). Many studies attempt to quantify the amount of collagen changing and orientation in any stages of wound healing, epipolarization microscope

picrosirius red-stained (Noorlander and et al., 2002), computer vision analysis of collagen fiber bundles (Elbischger and et al., 2004; Elbischger and et al., 2005), Fourier Transform Infrared (FTIR) spectral imaging (Potter and et al., 2001), and laser scanning confocal microscopy (Taylor and et al., 2002). However, all of these methods are complicate steps, using some special equipments and non available in routine histopathology laboratory unit.

The aim of this study was to measure the wound characteristics with imaging analysis program, ImageJ NIH (Girish & Vijayalakshmi 2004; Irving and et al., 2007) as a tool to quantify the area of interest especially collagen. This software package is accessible online at http://www.sbes.vt.edu/tools.htm. All of specimens were fixed both in 10% NBF and Bouin's solution in any difference stains, H&E and Masson's Trichrome.

Materials and Methods

Animals and Surgery

Six male outbred Sprague Dawley rat (8 weeks, 250±10 g) were used. The study was reviewed and approved by the Institutional Animal Care and Use

¹Department of Biology, Faculty of Science, Silpakorn University, Nakhon Pathom, Thaliland

²Quality Development Division, National Laboratory Animal Centre, Mahidol University (NLAC-MU), Nakhon Pathom, Thailand

³Production and Service Division, National Laboratory Animal Centre, Mahidol University (NLAC-MU), Nakhon Pathom, Thailand

Committee. Attending veterinarian care program was performed to reach the animal welfare acts. Animal were housed under clean conventional system in suspended cages/wire bottom and fed adlibitum. All survival surgery was performed using aseptic technique. Anesthesia consisted of Zoletil® (30 mg/kg) administered intramuscularly needed maintain deep anesthesia. to Standardized full thickness 15×15 mm² skin wounds (removing the subcutaneous layer) were excised both sides of the anterior dorsum of each anesthetized rat. Wound dressing with Tegaderm[®], clean with normal saline and betadine[®], were take placed everyday.

Specimens Processing

Healing wounds were collected after euthanized with over dose intraperitoneally of Thiopentone on day 7th. Divided healing wounds of both sides were fixed in 10% NBF 8hr, room temperature and Bouin's solution 48hr, room temperature (Presnell and Schreibman, 1997). The tissues were embedded in paraffin and sectioned at 6-7 μm . Alternate slides of each specimen were submitted to H&E stain (Harris, 1900) and Masson's Trichrome (Masson, 1929) for terminology collagen.

Gross and Histologic Measurements and Assessments

From each specimen, colour images of 640x480 pixel resolution were acquired with a light microscope (BX51, Olympus®) and digital camera (Moticam 1000, Moticam®) running under imaging analysis program (ImageJ, NIH). The collagen fiber intensity, surface area of neovascularization, and staining pattern of epithelial layer of skin and subcutaneous muscle were measured for comparison between fixations and stains. All of wound characteristics were quantified by Red-Blue-Green; RBG color histogram (figure 1A) and measure mode (figure 1B).

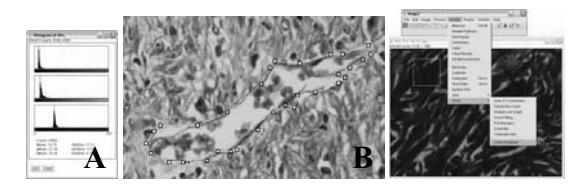


Fig.1 [A] The collagen fiber intensity was measured by color histogram mode, the red, blue, and green color intensity was showed as a result. Blue:green ratio was calculated as the comparison criteria. [B] Quantify the surface area of neovascularization was measured by analyse- area measure mode; Masson's Trichrome staining, 400x magn.

Data Analysis

Data are presented as mean values \pm SEM were calculated. The normality of the data was analyzed by the Kolmogorov – Smirnov test. Statistical comparisons with fixations were made by Student's t test in normal data. The non-parametric test Mann-Whitney was applied in non-normal data. The level of significance accepted was p < 0.05.

Results and Discussion

Skin wound full thickness had developed to proliferation and/or early remodeling phase after 7 days. As obviously could be seen the new vascularized vessels and collagen fibers formation. Under conventional light microscope, the collagen fibers had under clearly observation in both normal skin and wound area (figure 2). The arrangement of the collagen visible in the sections showed that the intensity and width in wound area are less than normal skin. Together with the collagen fiber plays a dominant role in maintaining the structural integrity and healing wound (Myllyharju & Kivirikko 2001). By this reason, several studies have been normally measured collagen content to quantified dermal wound recovering for application to pharmacological products as toxicity and efficacy test (Truong N.T and et al., 2005; Bae and et al., 2005; Roh and et al., 2006; Rao and et al., 2007).

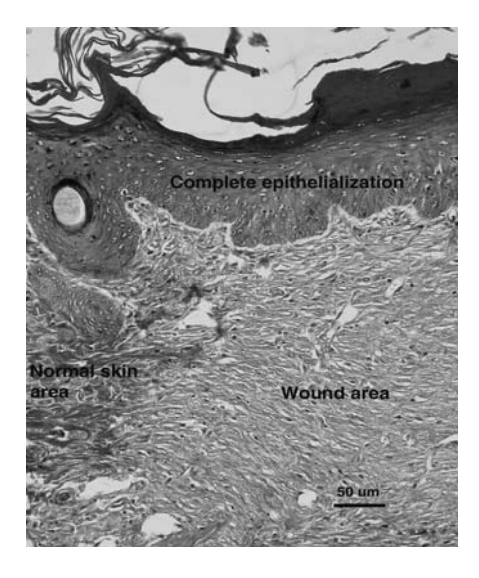


Fig.2 Photomicrograph of the complete epithelialization of wound with Masson's Trichrome staining, 100X magn., note that collagen intensity (blue) in wound area is less than normal skin area.

Staining intensity in epithelial layer of skin and subcutaneous muscle is shown in Table 1. Under H&E and Masson's trichrome, epithelial layer staining pattern which fixed in 10% NBF were less intensely than Bouin's solution. According to the intensity of RBG color, eosinophilic shade of red color on epithelial layer and keratinized material in

Bouin's solution is significantly higher than 10% NBF (figure 3; A-D). Similar to the result of the collagen measurement, in both normal skin and wound had low intensity in 10% NBF (figure 4; A-F). The blue shade of aniline blue on collagen fiber in Bouin's solution is significantly higher than 10% NBF. However there was no difference intensity of muscle fiber between both fixatives. The intensity of acidic dye of Biebrich scarlet on subcutaneous muscle in both fixatives was not difference (figure 3; E-F). The results are showed that there was moderate fixative effect on the staining pattern and color intensity because of its enhancement properties (Presnell and Schreibman, 1997).

The results are shown that there was no fixative effect on the basic architecture. The length of epithelial tongue was not significant different, between both fixatives (figure 4; G-I). Resemble to the magnitude, there was no difference on the size of neovascularized vessel at any sections direction, except longitudinal once (figure 4; J-L). We should be measured neovascularization, numerous capillaries arise from blood vessels adjacent to the

wound that invade the wound neodermis, because the formation of new blood vessels is necessary to sustain the newly formed granulation tissue (Madri and et al., 1996).

Dielectric TiO_2 thin film capacitors have been prepared successfully by dip-coating the TiO_2 films from TiO_2 sol-gel precursor. The maximum capacitance was obtained from 3-time dip coated TiO_2 film because of the pure phase, thick, uniform and smooth microstructure.

Further study, we intend to measure other wound characteristics which perform by image analysis program on analyzed particle mode such as (1) monocytes & neutrophils counting since they are the source of pro-inflammatory cytokines that probably serve as some of the earliest signals to activate local fibroblasts and keratinocytes (Pierce and et al., 1991; Hubner and et al., 1996) (2) macrophages since they are essential for effective wound healing (Leibovich and et al., 1975) (3) fibroblasts are responsible for the synthesis, deposition and remodelling of the extracellular matrix (Singer & Clark 1999).

Table 1 Staining pattern of epithelial and subcutaneous muscle in difference staining between 2 fixatives.

Stain	Zone	Fixative	Red intensity		p value	I	Blue inten	sity	p value	
			n	Mean	SEM		n	Mean	SEM	
H&E	Epithelial	Bouin's	20	1.59	0.01	0.000	20	1.47	0.01	0.98
		10%NBF	13	1.42	0.02		13	1.47	0.04	
	Epithelial	Bouin's	14	1.93	0.12	0.005	14	1.52	0.10	0.007
Trichrome		10%NBF	19	1.55	0.05		19	1.20	0.05	
	Muscle	Bouin's	18	1.9	0.06	0.15	18	1.11	0.03	0.69
		10%NBF	20	2.1	0.08		20	1.30	0.04	

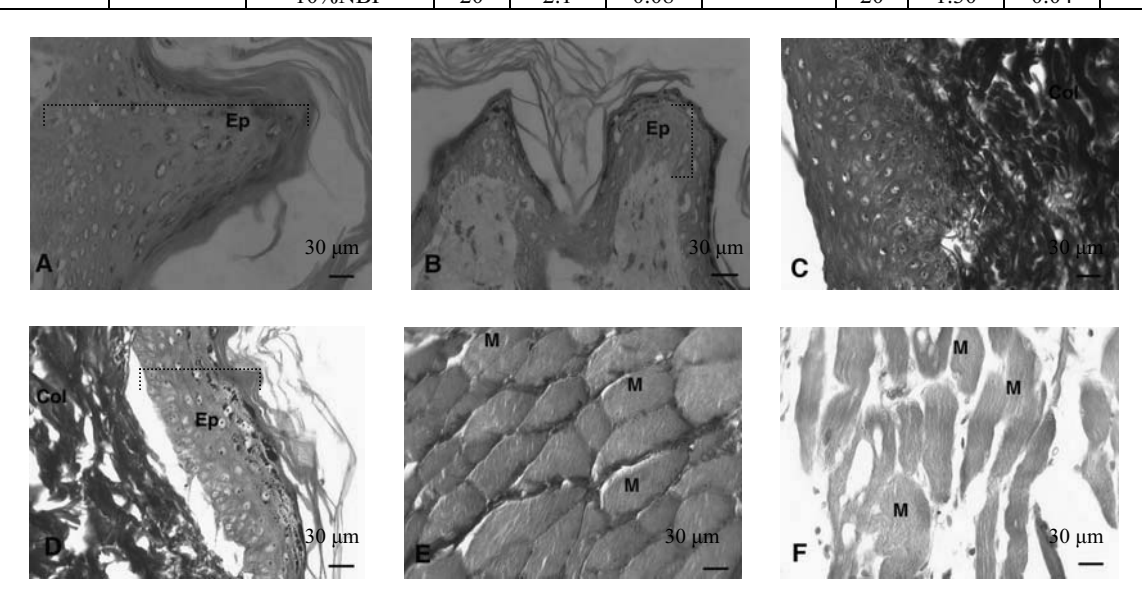


Fig. 3 The photomicrograph of staining pattern, 400X magn, epithelial layer with H&E staining in Bouin's solution **[A]** and 10% NBF **[B]**. Epithelial layer and subcutaneous muscle with Masson's Trichrome staining, in Bouin's solution **[C,E]** and 10% NBF **[D,F]**.Ep; epithelial layer, Col; collagen fiber, M; subcutaneous muscle.

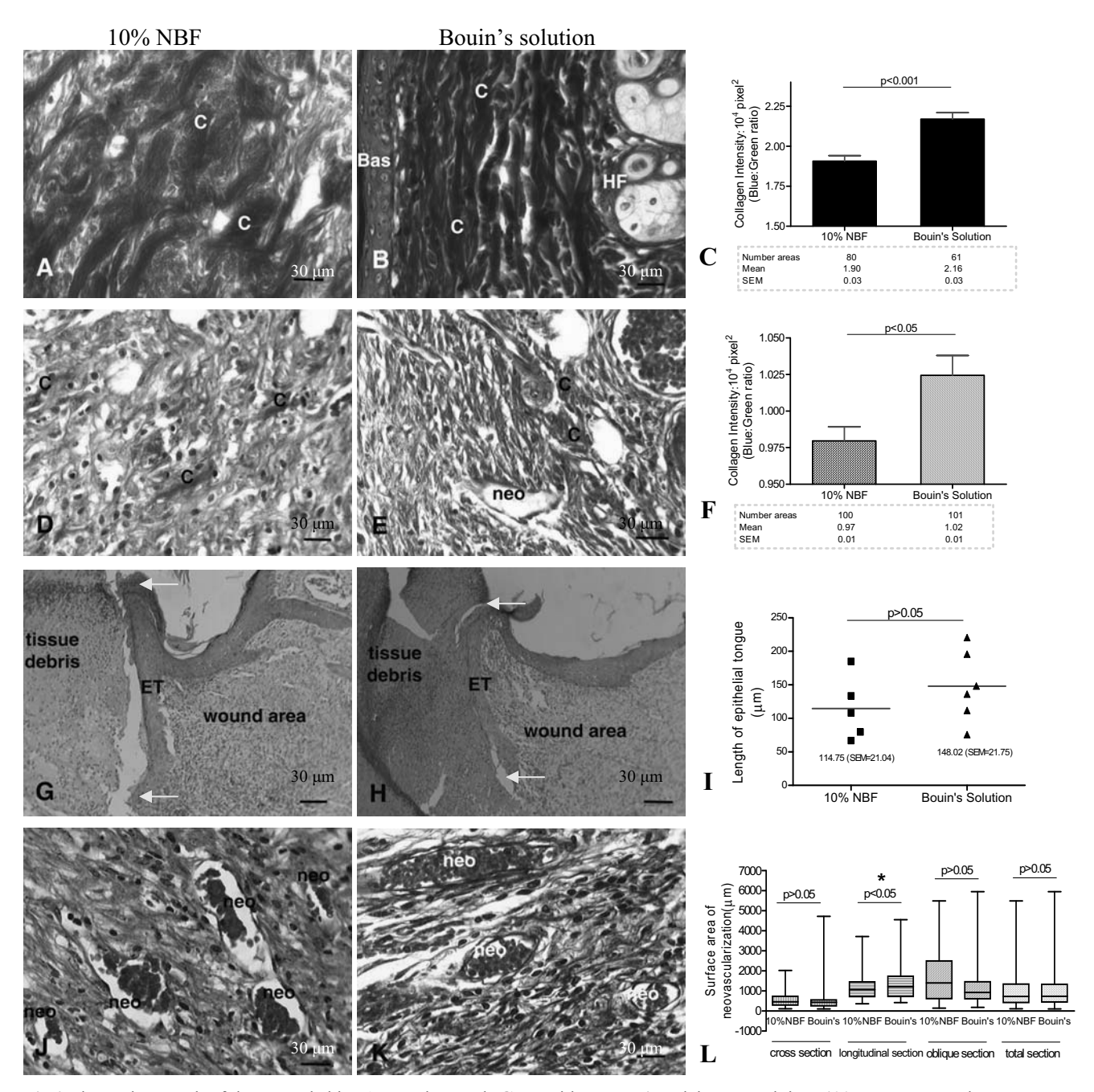


Fig.3 Photomicrograph of the normal skin **[A,B]** and wound **[G,H]** with Masson's Trichrome staining, 400X magn, note that 10% NBF **[A,D]** exhibit collagen (C) intensity lower than Bouin's solution **[B,E]**. HF; hair follicle, Bas; stratum basale, **[G,H]** Photomicrograph of the wound with H&E staining, 400X magn, showed that the length of epithelial tongue between both fixatives is equal, arrow indicate epithelial tongue (ET) edge. **[J,K]** Photomicrograph of the wound with Masson's Trichrome staining, 400X magn, exhibit surface area of neovascularization (neo) between both fixatives is equal.

Conclusion

Collagen measurement is normally used for application to pharmacological products as toxicity and efficacy test. Measurement by image analysis program, ImageJ, NIH provided an efficient tool for morphometric study and could be performed in routine histopathological laboratory with no more complicated methods and special tools except conventional light microscope. There was no fixatives effect on the basic architecture. Conversely, there was moderate fixatives effect on

the staining pattern and color intensity. Bouin's fixative is appropriate to fix tissue for measuring collagen fiber because of its enhancement property.

Acknowledgment

We would like to thank and deep appreciate to Colonel Dr. Piboon Phunyarit, Pathological Institute, Phramongkutklao Medical Centre Division, The Royal Thai Army Medicine Department that kindly provided some cytochemistry dyes.

- 1. Bae, J.S., Jang, K.H., Park, S.C. and Jin, H.K. Promotion of dermal wound healing by polysaccharides isolated from Phellinus gilvus in rats. *J. Vet. Med. Sci.*, 2005, 67(1):111-114.
- Ballas, C.B. and Davidson, J.M. Delayed wound healing in aged rats is associated with increased collagen gel remodeling and contraction by skin fibroblasts, not with differences in apoptotic or myofibroblast cell populations. Wound Repair Regen., 2001, 9(3):223-237.
- 3. Elbischger, P. J., Bischof, H., Regitnig, P., and Holzapfel, G. A. Automatic analysis of collagen fiber orientation in the outermost layer of human arteries. *Pattern Anal. Applic.*, 2004, 7: 269–284.
- 4. Elbischger P.J., Bischof, H., Holzapfel, and G.A., Regitnig, P. Computer vision analysis of collagen fiber bundles in the adventitia of human blood vessels. *Stud. Health Technol. Inform.*, 2005, 113:97-129.
- Girish, V. and Vijayalakshmi, A. Affordable image analysis using NIH Image/ImageJ. *Indian J. Cancer*, 2004, 41(1):47.
- Gogly, B., Godeau, G., Gilbert, S., Legrand, J. M., Kut, C., Pellat, B. and Goldberg, M. Morphometric analysis of collagen and elastic fibers in normal skin and gingiva in relation to age. Clin. Oral Invest., 1997, 1: 147–152.
- 7. Harris, H.F. Haematoxylin into haematein in staining reactions. *Appl. Microsc. Lab. Meth.*, 1900, 3:777-780.
- 8. Irving, B.A., Weltman, J.Y., Brockm, D.W., Davis, C.K., Gaesser, G.A. and Weltman, A. NIH ImageJ and Slice-O-Matic computed tomography imaging software to quantify soft tissue. *Obesity (Silver Spring)*, 2007, 15(2):370-376.
- 9. Leibovich, S.J. and Ross, R. The role of the macrophage in wound repair. A study with hydrocortisone and antimacrophage serum. *Am. J. Pathol.*, 1975, 78(1):71-100.
- Madri, J.A., Sankar, S. and Romanic, A.M. Angiogenesis. In: Clark RAF, ed. *The Molecular and Cellular Biology of Wound Repair*. New York: Plenum Press., 1996, p. 355.
- 11. Masson, P. Some histological methods. Trichrome staining and their preliminary

- technique. *Bulletin of the International Association of Medicine*, 1929, 12:75.
- 12. Myllyharju, J. and Kivirikko, K.I. Collagens and collagen-related diseases. *Ann. Med.*, 2001, 33(1):7-21.
- 13. Noorlander, M.L., Melis, P., Jonker, A. and Van Noorden, C.J. A quantitative method to determine the orientation of collagen fibers in the dermis. *J. Histochem. Cytochem.*, 2002, 50(11):1469-1474.
- Pierce, G.F., Mustoe, T.A., Altrock, B.W., Deuel, T.F., and Thomason, A. Role of platelet-derived growth factor in wound healing. *J. Cell Biochem.*, 1991, 45(4):319-326.
- Potter, K., Kidder, L.H., Levin, I.W., Lewis, E.N., and Spencer, R.G.S. Imaging of Collagen and Proteoglycan in Cartilage Sections Using Fourier Transform Infrared Spectral Imaging. Arthritis & Rheumatism., 2001, 44(4):846-855.
- Presnell, J.K. and Schreibman, M.P. Fixative. Humason's Animal tissue techniques.
 Baltimore: Johns Hopkins University Press. 1997, 14 – 28.
- 17. Rao, K.S., Patil, P.A. and Malur, P.R. Promotion of cutaneous wound healing by famotidine in Wistar rats. *Indian J. Med. Res.*, 2007, 125(2):149-154.
- Roh, DH, Kang, S.Y., Kim, J.Y., Kwon, Y.B., Young Kweon, H., Lee, K.G., Park, Y.H., Baek, R.M., Heo, C.Y., Choe, J. and Lee, J.H. Wound healing effect of silk fibroin/alginateblended sponge in full thickness skin defect of rat. J. Mater Sci Mater Med., 2006, 17(6):547-52.
- 19. Singer, A.J. and Clark, R.A. Mechanisms of Disease: Cutaneous Wound Healing. *N. Engl. J. Med.*, 1999, 341: 738-745.
- Taylor, M.D., Roberts, J.R., Hubbs, A.F., Reasor, M.J. and Antonini, J.M. Quantitative image analysis of drug-induced lung fibrosis using laser scanning confocal microscopy. *Toxic. Sci.*, 2002, 67:295-302.
- 21. Truong, N.T., Vern, A.K., Latenser, B.A., Wiley, D.E., and Walter, R.J. Comparison of Dermal Substitutes in Wound Healing Utilizing a Nude Mouse Model. *J. Burns Wounds.*, 2005, 14;4:e4:72-82.

Effect of Polysaccharide from *Phellinus ignarius* (L.) Quél. on Hematological Values and Blood Cell Characteristics in Diabetic Rats

C. Talubmook*

Faculty of Environment and Resource Studies and Department of Biology, Faculty of Science, Mahasarakham University, Maha Sarakham 44150, Thailand e-mail: chusri.t@msu.ac.th

Abstract

The effect of polysaccharide from *Phellinus ignarius* (L.) Quél. (PI) on the packed cell volume, hemoglobin concentration, red and white blood cell counts, and also the blood cell characteristics was investigated in streptozotocin-induced diabetic rats. PI at a dose of 100 mg/kg b.w. was injected venously daily to the diabetic rats for seven weeks. The results showed that PI decreased the pack cell volume, hemoglobin concentration, red blood cell count, and diameter of red blood cells but not white blood cell count. In addition, PI showed some alteration of the blood cell characteristics in diabetic rats. These data indicated that long term administration of PI changed some hematological values and some characteristics in diabetic rats.

Background

Diabetes mellitus is a metabolic disorder disease characterized by high blood glucose levels, which result from defects in pancreatic insulin and/or impaired target-cell secretion responsiveness to insulin [1]. This disease is characterized by chronic hyperglycaemia and other metabolic abnormalities and sometimes accompanied by symptoms of polydipsia, polyuria, polyphagia complications affecting various organs in the body such as the eye, kidney, nervous system and blood vessels. Hematological complications consist mainly of abnormalities in the function, morphology and metabolism of erythrocytes, leukocytes and platelets [2]. Treatment of diabetes mellitus and its complications in the recent context have focused on the usage of plant extracts [3]. Antihyperglycaemic activities of plant extracts and an extract from Phellinus ignarius (L.) Quél., mushroom, a member of Hymenochaetaceae, have been reported. However, the safety of extract in such treatment is still unclear whether it has any side effect(s). Moreover, the effect of the extract from PI. on hematology has not yet been demonstrated. Therefore, the effect polysaccharide from PI. on hematological values and blood cell characteristics in diabetic rats was carried out.

Materials and Methods

Preparation of PI

The polysaccharide from PI was kindly given by Frankie Chan from Thai-Korea Natural Phellinus Mushroom Research Center. On the day of experiment, polysaccharide at a given dosage was dissolved in 2 ml normal saline before intravenous injection to the diabetic rats.

Animals

Animals used in this study were male albino Wistar rats weighting 150-220 g purchased from the Animal Resource, National Research Council Thailand. The rats were acclimatized in an air conditioned room at 22-28 °C for five days and given a standard chow and watered *ad libitum* prior to the commencing experiments. The rats were maintained in accordance with the guidelines of the Committee on Care and Use of Laboratory Animal Resource, National Research Council Thailand. The experiments performed on the rats were performed in accordance with the advice of the Institutional Animal Care and Use Committee MSU.

Induction of Diabetes

The rats were injected intraperitonealy with a single dose of 65 mg/kg b.w. streptozotocin (STZ, Sigma Chemicals, St. Louis, MO) freshly dissolved in 20 mM citrate buffer adjusted pH to 4.5. After STZ injection, they were provided with a 2% sucrose solution as their drink for 48 hours to alleviate the severity after initial hypoglycemic phase. Blood glucose levels were assessed three days after STZ injection to confirm the diabetic stage. Rats with blood glucose level of at least 200 mg/dl were used in the experiment [4].

Experimental Design

The experiment consisted of 4 groups;

Group 1: Control rats received 2 ml normal saline

Group 2: Diabetic rats received 2 ml normal saline

Group 3: Diabetic rats received 0.25 mg/kg b.w. glibenclamide

Group 4: Diabetic rats received 100 mg/kg b.w. PI

The rats were administered once daily for seven weeks. At the end of the experiment, the rats were anesthetized with ether. Blood samples obtained from the tail vein of animals were used for the determination of hematological values. The blood cell characteristics and ultrastructure were also monitored.

Hematological Values

Hematological values were examined in according with the protocol used by Chomko and Talubmook [5]. Blood sample was filled in heparinised capillary tube and centrifuged at 1,500 rpm for 5 min. After centrifugation, the capillary tube was placed in microhematocrit reader and the packed cell volume (PCV) was determined. The hemoglobin concentration was determined using Sahli method, hematin obtained from the reaction of hemoglobin and hydrochloric acid was compared with the standard hematin. Total red and white blood cell counts were examined manually using hemocytometer after the blood was diluted. The diluting solution for red blood cell was Gower's solution but for the white blood cell was Turk's solution.

Light Microscopic Specimen Preparation

Blood smear was fixed in methanol and stained with Wright-Giemsa stain for morphological study of white blood cells.

Ultrastructure of Blood Cells

Investigation of ultrastructure of blood cells was performed with the aid of the Scanning Electron Microscope. Specimens were fixed in Karnovsky's fixative, and dehydrated in an acetone series. Dried specimens were mounted on stubs, coated with gold and viewed in Scanning Electron Microscope (JEOL6460LV) [6].

Statistical Analysis

The results of hematological values and the length and width of blood cells were presented as the mean \pm SEM. Comparisons were made between control and treatment groups using one-way analysis of variance (ANOVA) followed by

Duncan's New Multiple Range Test. Values of p < 0.05 were regarded as statistical significant.

Results and Discussion

The homological values of controls, diabetic controls and diabetic rats treated with PI were shown in Table 1.

The packed cell volume from PI treated rats was not different from diabetic control and glibenclamide treated rats but was significantly (p<0.05) less than that from normal controls. The hemoglobin concentration was also significantly (p<0.05) less than the control, diabetic control and glibenclamide treated rats. In addition, the red blood cell count was significantly (p<0.05) less than normal controls and glibenclamide treated rats. In contrast, the white blood cell count was significantly (p<0.05) higher than the controls and glibenclamide treated rats. Nevertheless, the red and white blood cell counts were not different from the diabetic controls.

Table 1 Hematological values of controls, diabetic controls, diabetic rats treated with glibenclamide, and diabetic rats treated with PI.

Groups	PCV (%)	Hb (g/dl)	RBC (x10 ⁶ cell/µl)	WBC (x10³cell/µl)
control	53.00 <u>+</u> 1.06 ^b	21.33 <u>+</u> 0.21	8.67 <u>+</u> 0.37 ^b	5.63 <u>+</u> 0.22 ^a
Control	ab		ab	b
diabetic control	51.00 <u>+</u> 0.89 ab	21.16±0.47	7.85±0.30 ab	7.11 <u>±</u> 0.53 ^b
glibenclamide	50.50 <u>+</u> 1.58 ^{ab}	20.66 <u>+</u> 0.49	8.58 <u>+</u> 0.34 ^b	4.41 <u>+</u> 0.62 ^a
	40.50 1.70 8	10 22 10 22	(51:0748	7.62+0.50 b
Phellinus ignarius	48.50 <u>+</u> 1.72 ^a	19.33 <u>+</u> 0.33	6.51 <u>+</u> 0.74 ^a	7.62 <u>+</u> 0.50 ^b

Means \pm SEM within the same column followed by the different letters are significantly different at p<0.05. Abbreviations: PCV packed cell volume, Hb hemoglobin, RBC red blood cell, WBC white blood cell.

Table 2 Diameter of the red blood cells in of controls, diabetic controls, diabetic rats treated with glibenclamide, and diabetic rats treated with PI.

Groups	Diameter of red blood cell (µm)
control	5.40 <u>+</u> 0.10 ^{ab}
diabetic control	5.62 <u>+</u> 0.10 ^b
glibenclamide	5.57 <u>+</u> 0.11 ^b
Phellinus ignarius	5.17+0.12 ^a

Means \pm SEM within the same column followed by the different letters are significantly different at p<0.05.

Table 2 showed that the diameter of red blood cells from PI treated rats was significantly (p<0.05) smaller than those from controls, diabetic controls and glibenclamide treated rats. Figure 1 presented different characteristics of the young and old red blood cells from controls, diabetic controls, glibenclamide treatment and diabetic rats treated with PI. The red blood cells of all rats were non-nucleated biconcave disk. The old ones were small and had a prominent central pallor. However, the

red blood cell characteristics from all experimental rats were not significantly different. Figure 2 showed the smooth membrane red blood cells and the knobby white blood cells. Nevertheless, the red and white blood cells of all experimental rats were not different. Figure 3 illustrated the white blood cells; lymphocytes, monocytes, neutrophils, and eosinophils. Significant differences of all types of white blood cells from experimental rats were not found.

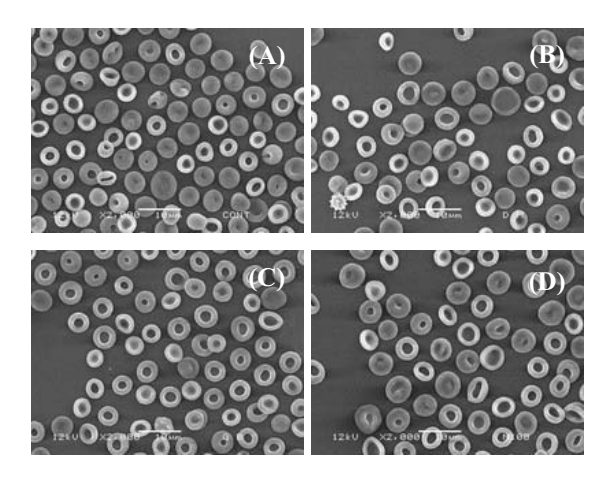


Fig. 1 Scanning electron micrographs of red blood cells from controls (A), diabetic controls (B), diabetic rats treated with glibenclamide (C), and diabetic rats treated with PI (D).

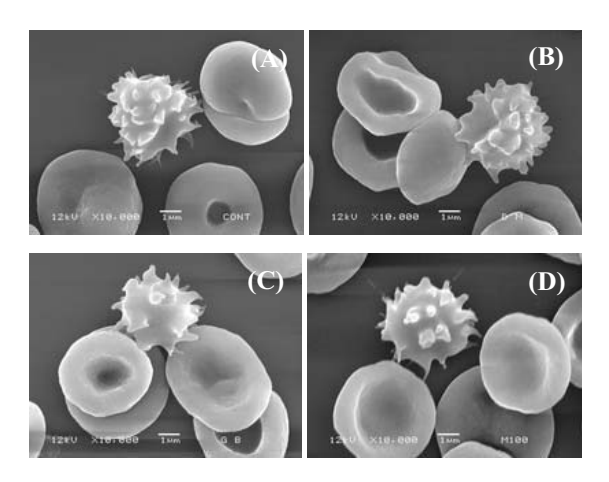


Fig. 2 Scanning electron micrographs of red and white blood cells from controls (A), diabetic controls (B), diabetic rats treated with glibenclamide (C), and diabetic rats treated with PI (D).

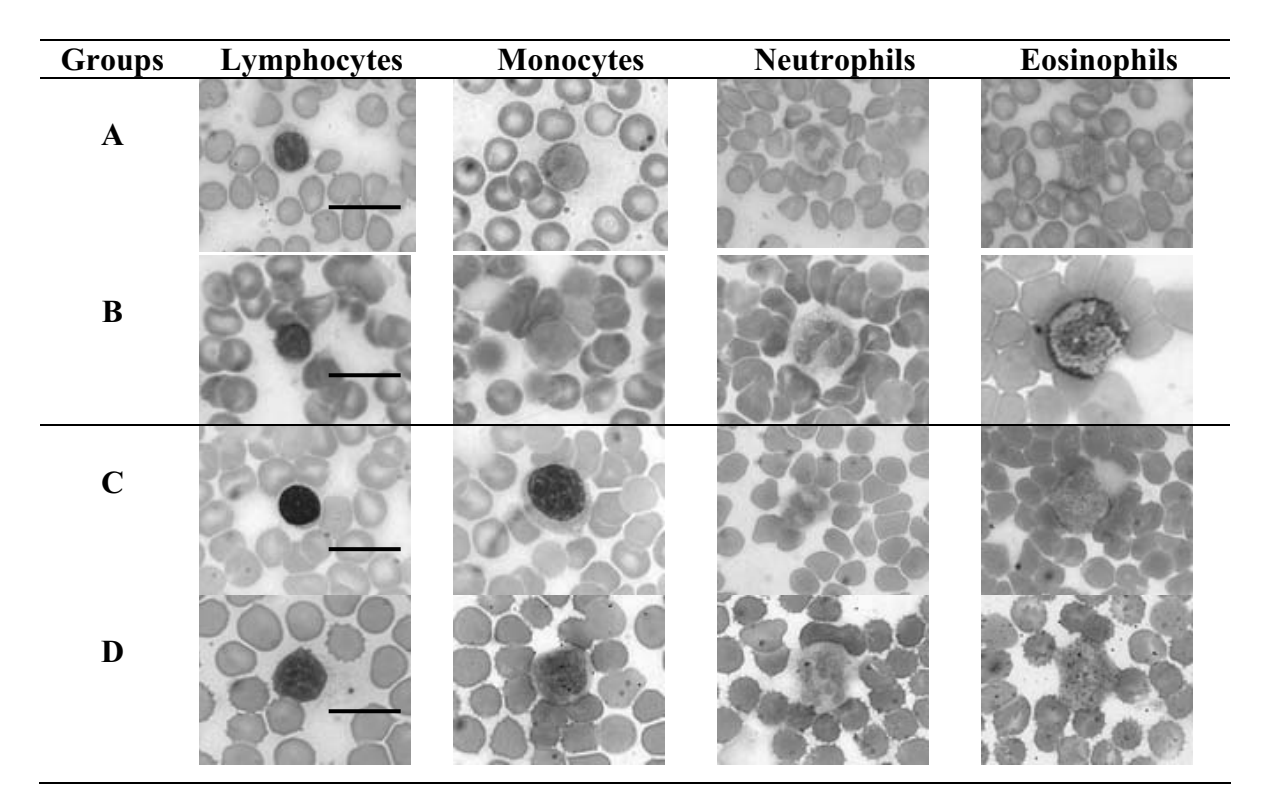


Fig. 3 White blood cells from controls (A), diabetic controls (B), diabetic rats treated with glibenclamide (C), and diabetic rats treated with PI (D). bars = $10 \mu m$

Conclusion

In conclusion, the overall results showed that long-term treatment of PI altered some hematological values but not ultrastructure of blood cells in diabetic rats.

Acknowledgment

This research was supported by grant from the development research division and Faculty of Science, Mahasarakham University, Thailand. The author would like to thank Dr. Savittree Wongtangthintarn for her help. Thank also go to Areeya Suchantabud and Thanutchaporn Mahanarm for technical assistance.

References

1. Talubmook, C. The influence of elevated glucose levels and the diabetic state on neuromuscular function in the gut, Hatfield: University of Hertfordshire, 2002, (Ph.D. thesis).

- Comazzi, S., Spagnolo, V. and Bonfanti, U. Erythrocyte changes in canine diabetes mellitus: in vitro effects of hyperglycaemia and ketoacidosis. *J Comp Clin Path.* 2004, 12: 199-205.
- 3. Kamalakkannan, N. and Mainzen, P.S. Rutin improves the antioxidant status in streptozotocin-induced diabetic rat tissues. *J Mol Cell Biochem.* 2006, 293: 211-219.
- 4. Talubmook, C., Forrest, A. and Parsons, M. Streptozotocin-induced diabetes modulates presynaptic and postsynaptic function in the rat ileum. *Eur J Pharmacol*. 2003, 469: 153-158.
- 5. Chomko, S. and Talubmook, C. Effect of leaf extracts from *Morus alba* and *Annona squamosa* on hematological values in diabetic rats. *J Sci and Technol. MSU*. 2007, 26: 167-173.
- Ponsen, S., Narkkong, N-A. and Angwanich, W. Morphological and ultrastructural observations on the blood cells of Sand Lizards (*Leiolepis* belliana Rubritaeniata) Mertens 1961. J Anim Vet Adv. 2007, 6(4): 522-527.

Microscopy and Image Analysis Techniques for Quality Control in Food Industry: A Case Study of Wheat Grain Cooking Process

K. Srikaeo*

Food Science and Technology Program, Faculty of Food and Agricultural Technology, Pibulsongkram Rajabhat University, Muang, Phitsanulok, Thailand

e-mail: khongsak@psru.ac.th

Abstract

A variety of microscopy techniques have been applied in food industry for quality control purposes. This paper demonstrates the use of a scanning electron microscope (SEM) and a light microscope (LM) in conjunction with image analysis for investigation of starch granules, in order to judge the quality of starch gelatinization in wheat grain cooking process. Both SEM and LM with image analysis are proved to be a useful tool. The present study shows that the swelling and melting of starch granules are influenced by the cooking process. The use of LM with subsequent image analysis provided a simple method for observation of starch gelatinization and quantitation. This study also demonstrates that SEM and LM are useful for the investigation of starch granules in cooked wheat grains without prior starch isolation.

Background

The cooking of wheat grains with steam under pressure is an initial process for some breakfast cereals. This process is important as it develops the grain properties necessary for the development of the product characteristics such as texture, flavor and color - primarily by gelatinization of the starchy grain fractions [1]. Microscopy techniques be used for examination of starch gelatinization. Recently, a variety of microscopy techniques have been applied into food industry for quality control purposes, particularly in cereal products [2]. This study demonstrates the use of scanning electron microscope (SEM) and a light microscope (LM) to observe the gelatinization of intact starches within the whole grain system during the cooking process. Microscopy images were used to judge the quality of starch gelatinization in cooked wheat grains.

Materials and Methods

Mixed varieties of soft wheat grains, 10% protein content, were used. Wheat samples (100 g) were cooked in a steam pressure cooker (45 L volume and 413 kPa maximum pressure). The cooking conditions included cooking at the same temperature (120 °C) for 20, 40, 60, 80, 100 and 120 min, and cooking for the same time (40 min) at 110, 130 and 140 °C.

For the SEM analysis, the cooked wheat samples from various conditions were cut in cross section and then frozen instantly using liquid nitrogen. Frozen samples were dried using a freeze drier (Dynavac Freeze Drier). Dried samples were mounted onto aluminum stubs using metal adhesive glue and then coated with gold (SPI Gold

Sputter Coater) before observed by the SEM (Phillips XL30). SEM images of each sample were taken at 1,000x magnification.

For the LM study, cooked wheat grains after cooling down and equilibration to room temperature were dried in a vacuum oven at 40 °C for about 24 hr. This low temperature drying should limit the effect of heat on the remaining starches. Dried samples were ground using a laboratory mill (LM 3100, Perten Instruments, 0.8 mm sieve). This provided the cooked-wheat flour which was then used for the LM observations. Suspensions of cooked-wheat flour (1g/25mL distilled water) were prepared in the test tube, iodine stained and mixed thoroughly before being analyzed by direct LM (Kyowa Medilux-12) at 40x magnification. Notably that the suspensions were sampled immediately after mixing using a dropper and then smeared on slides before covered with cover glasses. The sampling was conducted with the minimized time to ensure the uniformity of starch in the suspensions. LM images were captured by the digital camera (Pulnix TMC-6) attached with the microscope using the resolution at 640 x 480 pixels for all samples. The images obtained were then analyzed for the number and size of the starch granules (determined from the dark particles in the captured LM images) using Image-Pro Plus Version 1.3.2 (Media Cybernetics U.S.). Notably that this study assumed the darkblue spots found in the LM images to be starch granules. However, they might not be all starches since the samples were cooked wheat flour, other component e.g. protein embedded with starch granules could also be counted.

Results and Discussion

The SEM images of samples cooked at the same temperature (120 °C) for different times are shown in figure 1. In addition, figure 2 represents the SEM images of wheat grains cooked at different temperatures for the same time (40 min).

The SEM provides a clear view of changes of intact starch granules in cooked wheat samples. For the experiment on the same cooking temperature (figure 1), when cooking for a short time e.g. 20 min, the lentil-shaped and circular starch granules of various sizes (both A and B types), protein matrix, and adhesive protein areas attached to starch granules were clearly observed. However, when cooking for a longer period, starch gelatinization increased, resulting in swelling and melting which led to strong deformation of the granules and ultimately the molten granules connected with one another. Other components of the grains such as protein, pentosan and gluten also absorbed water and could be denatured when exposed to heat for a longer period. The combination of these factors resulted in the changes of starch microstructure which were progressively more shapeless or mud-like structure. For the experiment on the same cooking time (figure 2), as expected, samples exposed to higher temperatures e.g. 130-140 °C developed more mud-like structure than those exposed to lower temperatures e.g. 110-120 °C.

SEM observation of starch granules during gelatinization has been well documented but mainly in systems of pure starches with water. This study showed that SEM could be used to observe the starch granules in the whole grain system without the need for starch isolation. Although, the SEM images are not as clear as in isolated or pure starch systems, they provide similar patterns. For qualitative purposes or product quality control in food manufacturing, the results should be acceptable.

Figure 3 shows the LM images of wheat samples cooked at the same temperature (120 °C) for various times (20-120 min). Similar patterns were obtained for the experiment of cooking at the same time (40 min) but different temperatures (110-140 °C), the images are not shown.

It is well known that gelatinized starch granules become bigger in size and granule shape turns to be a honeycomb-like structure. Figure 4 shows the average area sizes of the starch granules, determined from the dark-blue spots and calculated by the image analysis software. It appears that, with the increased cooking time or temperature, the area of starch granules increased as a result from swelling and structural changes of starch granules together with the connection to each other and other components.

LM with iodine staining is a simple and well established technique for the observation of starch granules. This study demonstrated the use of LM and computer-based image analysis for quantitative investigation of starch granules. A cooked-wheat flour system without prior isolation of starches was investigated. Such a simple preparation could be beneficial in practices or for industrial uses as starch isolation is a complicated and time-consuming procedure especially isolation of starch from cereal products.

Conclusion

Both SEM and LM could be used for investigation of starch gelatinization in the whole grain system without the need for prior isolation of starches. These simple methods could be practical for food industries for the quality control of their products, particularly in cereal products in which starch gelatinization is the main processing step. The enhancement of image analysis in conjunction with traditional LM techniques provides a simple method for investigation of starch granules with quantitative results. However, it should be kept in mind that the microscopic methods used in this study are limited for some purposes e.g. for industrial use. The results should be used with great care.

- Caldwell, E.F., Fast, R.B., Levolella, J., Lauhoff, C., Levine, H., Miller, R.C., Slade, L., Strahm, B.S. and Whalen, P.J. Cooking of ready-to-eat breakfast cereals. Cereal Foods World. 2000, 45: 246-252.
- Srikaeo, K., Furst, J.E., Ashton, J.F. and Hosken, R.W. Microstructural changes of starch in cooked wheat grains as affected by cooking temperatures and times. LWT. 2006, 39: 528-533.

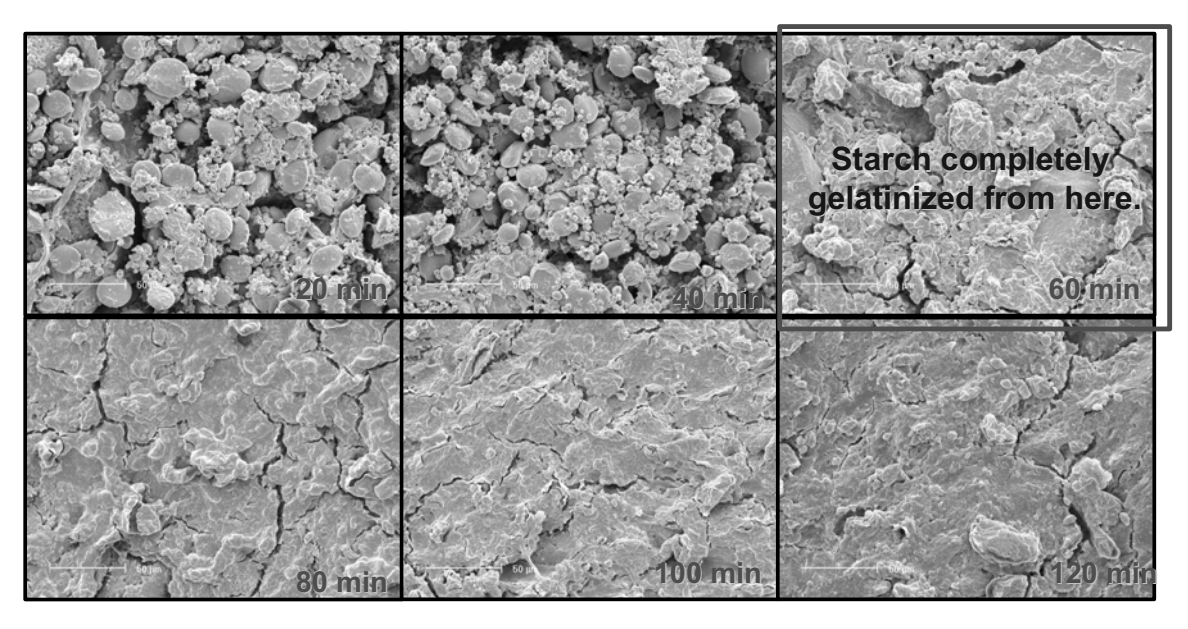


Fig. 1 SEM images of wheat grains cooked at 120 °C for 20, 40, 60, 80, 100 and 120 min

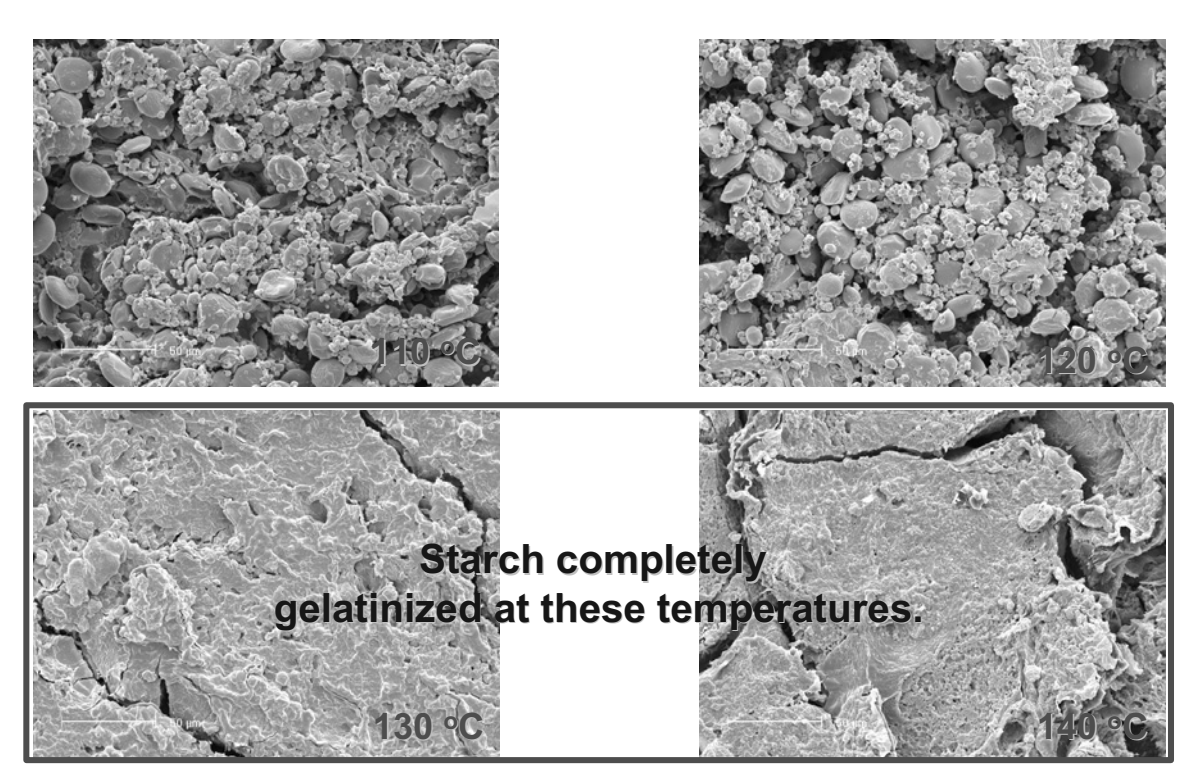


Fig. 2 SEM images of wheat grains cooked at 110 - 140 $^{\rm o}{\rm C}$ for the same time (40 min).

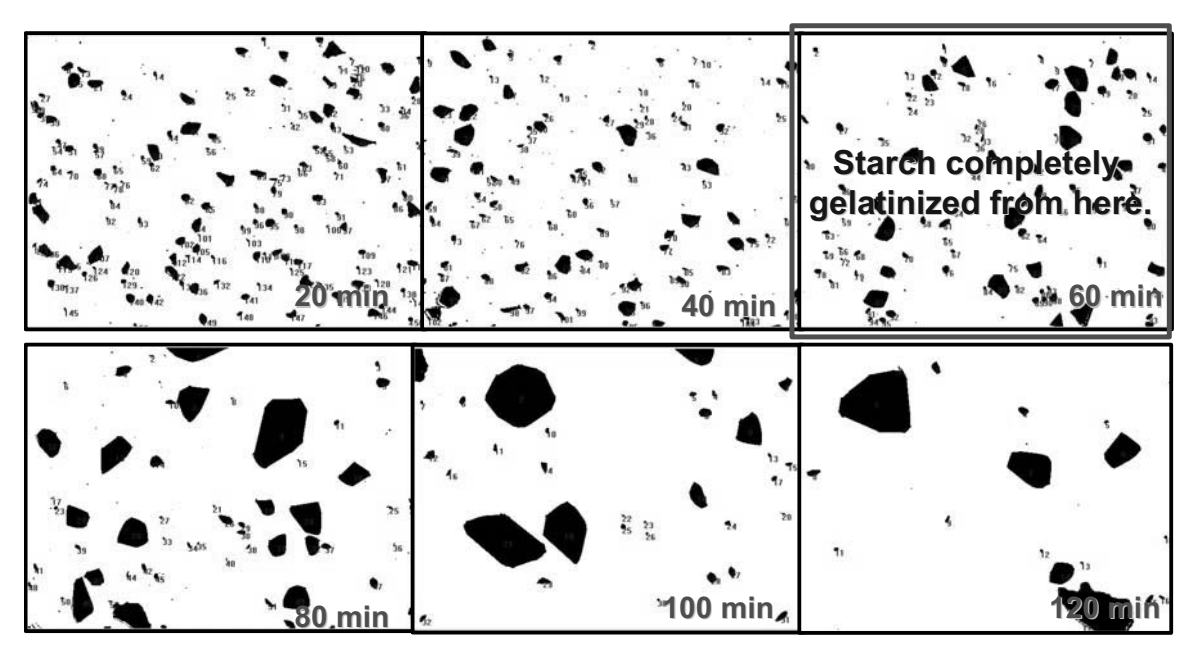


Fig. 3 LM images of wheat grains cooked at 120 °C for 20, 40, 60, 80, 100 and 120 min.

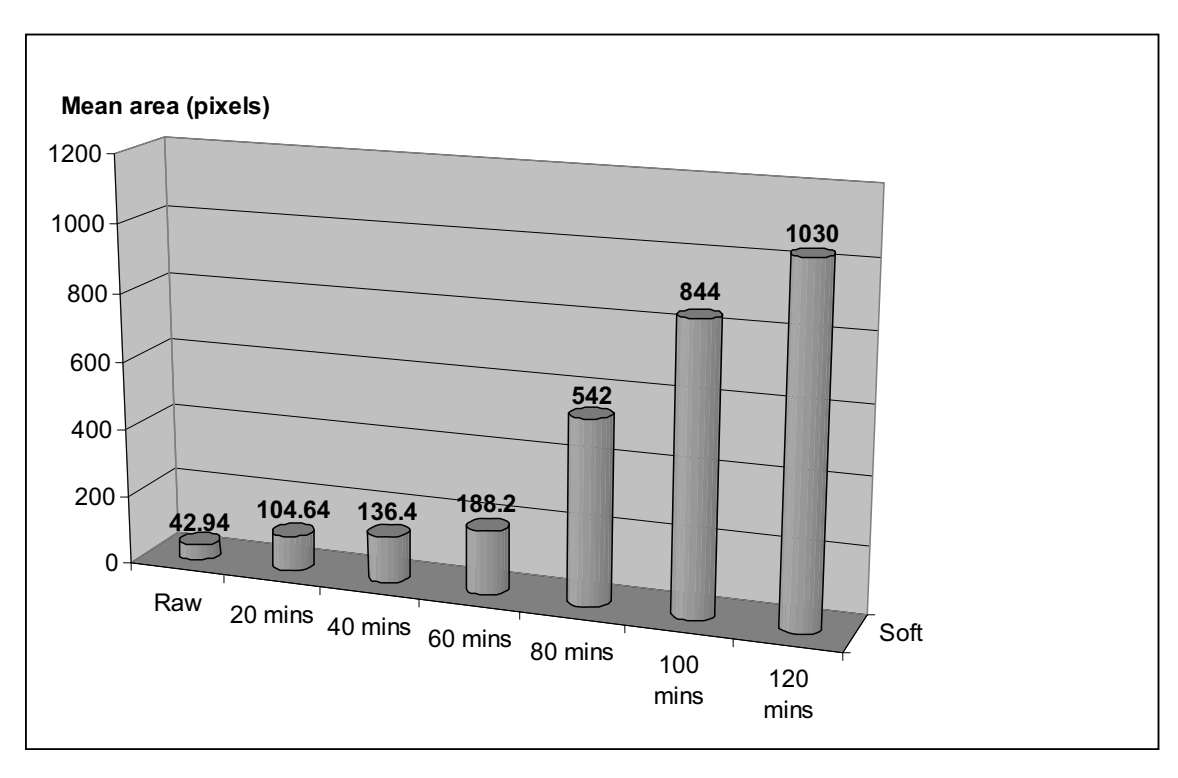


Fig. 4 Average area sizes of starch granules of raw wheat and wheat grains cooked at 120 °C for 20, 40, 60, 80, 100 and 120 min (calculated by image analysis software)

Neuronal Sprouting Following Spared Nerve Injury in Rats Studied by Cholera Toxin B Subunit Immunoreactivity

Supin Chompoopong^{1*}, Kanyarat Bamrungsuk¹, Kanokwan Tilokskulchai² and Tulaporn Wongtawatchai¹ Department of Anatomy and ²Department of Physiology, Faculty of Medicine, Siriraj Hospital, Mahidol University, Bangkok 10700, Thailand

e-mail: siscm@mahidol.ac.th

Abstract

Objective: The aim of this study was to determine whether spared nerve injury (SNI) alters the laminar terminations of A-beta fibers in rat spinal dorsal horn.

Materials and Methods: Twenty six adult male rats weighing 250-300 grams were randomly assigned into two groups (n=13 each). One group underwent SNI. Another group was subjected to sham operation. The SNI was performed on the right hind limb by transected the tibial and common peroneal nerves leaving the sural nerve intact. Three days before sacrifice of rat, the sciatic nerve proximal to injury site was injected with cholera toxin B subunit (CTB) that effectively labels both peripheral and central A-beta axons. The effect of SNI was evaluated by analyzing the extent of CTB (CTBir) and substance P (SPir) immunoreactivities with confocal microscopy in L4-L6 dorsal root ganglia (DRG) and spinal dorsal horn at five weeks after surgery. The intensity of SPir were analysed as the percentage changes in mean grey level by using ImageTool program 3.0 and compared between SNI and sham groups.

Results: Following SNI, SPir in DRG and spinal dorsal horn were significantly increased with respect to sham, p < 0.001. On the basis of the use of CTB as a selective tracer for A-beta fibers, neuronal sprouting was studied in the spinal dorsal horn. In sham operation group, CTBir was present in laminae III and IV. In SNI group, CTBir distributed in laminae III and IV and dispersed into lamina II, a region that normally receives only C-fiber input. In addition, CTBir was shown co-localization with SPir in medium- and large-size DRG neurons.

Conclusions: The present results showed that the increase of SPir in DRG and spinal dorsal horn may due to elevated NGF levels from Schwann and other endoneurial cells involved in Wallerian degeneration following SNI. It was also shown that the central terminals of cutaneous myelinated afferents, including the large A-beta fibers from the medium- and large- DRG neurons, sprout into lamina II of spinal dorsal horn. This lamina that normally receives nociceptive input was activated by tactile stimuli. It was suggested that this structural reorganization in the central nervous system may contribute to mechanical allodynia associated with neuropathic pain. Therefore, this phenomenon may also help to explain the pain mediated by A-fiber following peripheral nerve injury in patients.

Background

Neuropathic pain represents a major clinical problem because in contrast to nociceptive pain, it is largely resistant to the methods that are presently available for pain relief. There is the evidence that this type of pain is mediated by large myelinated (A-beta) afferents (1, 2). Because stimulation of these afferents does not normally produce pain, it is believed that changes within the CNS must be involved (3).

It is clear that in DRG, most large and medium diameter neurons possess large myelinated axons (A-beta fibers). Small neurons exhibit axons with either no myelination (C-fibers) or thinly myelinated axons (A-delta fibers). The central projections of DRG neurons convey functionally distinct information to the spinal dorsal horn in a laminar-specific manner. Small diameter slowly conducting DRG neurons with C-fibers and A-delta fibers are principally nociceptive with central projections to laminae I and II of the spinal cord

dorsal horn (4). Large diameter neurons with Abeta fibers have central terminations in laminae III–VI (5).

Following peripheral nerve injury, the neuronal sprouting can be defined as the growth of intact axons into neighboring denervated territory. There was the evidence that the nerve lesion such as partial denervation results in the peripheral sprouting of both small (6) and large (7) intact primary sensory axons. The central sprouting of uninjured primary sensory neurons in the spinal dorsal horn which denervated by transection of adjacent dorsal roots was first suggested by Liu and Chambers (1958) (8). Since then, the notion that denervation alone is sufficient to induce sprouting of the central axons of uninjured primary sensory neurons has been both supported (9, 10) and disputed (11, 12).

To date, it is still controversial what are responsible for the central sprouting of those primary afferents. Recently, the cholera toxin B subunit (CTB) that effectively labels both peripheral and central A-beta axons has been used to study in sciatic nerve section or crush models. The mechanism of A-fiber sprouting has been thought to involve this injury (13). Since there is evidence indicating that SNI rat model closely mimic many features of clinical neuropathic pain (14). It has been proposed as a useful tool for identifying the development of mechanisms involved in the production of neuropathic pain and as an additional model for screening the efficacy of new treatments. Therefore, in this study, the CTB was injected into the injured nerve to determine whether SNI alters the laminar terminations of Abeta fibers in rat spinal dorsal horn.

Materials and Methods

All experiments were performed on adult Sprague Dawley male rats (average weight 250-300g). During the experimentation period, the rats were housed in individual cages with free access to food and water and at a controlled room temperature (22±2°C) with a twelve-h light/dark cycle. All procedures complied with the ethical guidelines for pain experimentation on awake animals (15) and were approved by the Ethical Committee on Animal Experiments of Mahidol University. This study was based on results obtained from 26 rats randomly distributed into two groups (n= 13 each). One group underwent spared nerve injury (SNI) and another group was subjected to sham operation (Sham)

Nerve Injury Surgical Procedure

Peripheral neurophathy following Decosterd and Woolf (14) model was induced in the SNI group. Briefly, under pentobarbital sodium anesthesia (40 mg/kg, i.p.), the skin on the lateral surface of the right thigh was incised and a section made directly through the biceps femoris muscle exposing the sciatic nerve and its three terminal branches: the sural, common peroneal and tibial nerves. The common peroneal and the tibial nerves were transected close to the position that nerves enter the muscles and leaving the sural branch intact. Great care was taken to avoid any contact with or stretching of the intact sural nerve. Muscle and skin were closed with 3-0 silk in two layers. The wound was then covered with topical antibiotics. In sham controls the right sciatic nerve and its branches were identically exposed without any lesion. In both groups, the contralateral thigh remained unoperated.

Tracing of A-beta Projections to the Dorsal Horn

Cholera toxin B-subunit (CTB) have been used to map the central rojections of cutaneous

myelinated primary afferents in the spinal dorsal horn of rats (16). Three days before sacrifice, all animals were anesthetized with sodium pentobarbital (40 mg/kg i.p.). Right sciatic nerves were reexposed and injected proximal to the injury site with small volumes (2.5–3 microlitre) of CTB (sigma, 1% dissolved in distilled water) by using Hamilton microsyringes.

Tissue Preparation and Immunofluorescent Staining

SP and CTB were determined in SNI and Sham rats by immunofluorescent histochemistry. Five weeks after surgery, all animals were anesthetized with sodium pentobarbital (50 mg/kg i.p.) and perfused transcardially with 100 ml saline followed by 500 ml ice cold 4% paraformaldehyde in 0.1 M phosphate buffer (PB) at pH 7.4. The L4-L6 spinal cord and DRG were removed, placed in the same fixative overnight at 4°C, and transferred to 30% sucrose (w/v) in 0.1 M PB for three days for cryoprotection. Serial coronal section of spinal cord and DRG at a thickness of 40 µm and 15 µm, respectively were prepared in a Leitz cryostat and mounted on gelatin coated slides. The sections were treated with phosphate-buffered saline (PBS, 0.1M, pH 7.2) containing 1% BSA and 0.05% Tween-20 for 30 min at room temperature. The primary antiserum, goat polyclonal antiserum directed against SP (1:50; Santa Biotechnology) and rabbit anti-cholera toxin B (1:1000, Sigma) in 0.1M PBS containing 1% BSA and 0.05% Tween-2 was used for the incubation with the sections for overnight at 4°C. The sections were washed in 0.1 M PBS and then incubated in the secondary antiserum, FITC-conjugated donkey anti-goat IgG (1:500; Santa Crus Biotechnology) and 1.5% Texas Red anti-rabbit IgG (Vector laboratories) for 3 h at room temperature. After several rinses in 0.1 M PBS, sections were cover slipped with Vectashield (Vector) and observed under a Carl Zeiss Confocal Laser Scanning microscope.

Image Analysis

Image analysis of SPir staining was performed on five nonadjacent sections of DRG and spinal dorsal horn from each animal. To determine changes in SPir in the SNI and sham groups, the density of SPir was quantified using a computerbased image analysis system (the free UTHSCSA ImageTool program, 3.00) (17). While viewing the monitor, upper and lower thresholds of grey level density were set such that only specific SP product immunoreaction was accurately discriminated from the background in the outlined lamina I-IV of the dorsal horn and DRG. The pixel-by-pixel was read by the computer (18).

Subsequently, the total area of discriminated pixels was divided by the area of the outlined dorsal horn. The mean grey level values from the five random sections were averaged for each animal and expressed as mean \pm S.E.M. Since the staining on the contralateral side was equivalent to that seen in unoperated animals, the percentage change in DRG and spinal dorsal horn was calculated as ipsilateral/contralateral X 100. The changes in SPir staining in DRG and spinal dorsal horn were compared by using independent sample t-test. Differences were considered significant if p < 0.001.

Results

General Observations

The majority of rats subjected to SNI displayed evident signs of neuropathy in the hind paw ipsilateral to the nerve injury. This was clearly present 24 h after the surgery. These signs included abnormal position of the paw (inversion) and signs of spontaneous pain such as shaking and licking. No autotomy or body weight loss was observed. It is worth noting here that rats without evident signs of neuropathy were not included in this study.

SP and CTB Immunofluorescent Localization

SP and CTB were located in DRG and spinal dorsal horn of rats by immuno-fluorescent staining. As shown in table 1, the percentage changes of mean grey level of SPir were analyzed and compared between SNI and sham groups. Following five weeks surgery, SNI rats demonstrated a significant increase of SPir in DRG and spinal dorsal horn on the operated side, as compared with the same side in sham, p < 0.001.

Using retrograde labelling with CTB to identify A-beta fibers, CTBir was shown co-localization with SPir in medium- (30-50 micrometer) and large-size (> 50 micrometer) DRG neurons five weeks after SNI (figure 1A). But only SPir was shown in small-size (< 30 micrometer) DRG neuron. In addition, neuronal sprouting was studied in the spinal dorsal horn. In sham operation group, CTBir was present in laminae III and IV (data not shown). In figure 1B, it was shown that SNI results in the sprouting of numerous CTBir- labeled large myelinated sensory axons. These A-beta fibers sprout from their normal termination site in laminae III and IV into lamina II, a region that normally receives only C-fiber input.

Discussion

As proposed previously by Decosterd and Woolf (2000), SNI is well-established methods that are available to measure thermal and mechanical sensitivity in awake behaving rats for studying the neuropathic pain. The purpose of this investigation was to determine whether SNI alters the laminar

terminations of A-beta fibers in rat spinal dorsal horn. In this study, it was demonstrated that the transected tibial and common peroneal nerves leaving the sural nerve intact in this SNI model could result in a significant increase of SPir in DRG and spinal dorsal horn five weeks after injury. In contrast, the previous report was shown that complete sciatic nerve injury reduces SP expression in primary sensory neurons of the L4 and L5 DRG and spinal dorsal horn, due to loss of target-derived nerve growth factor (NGF) (19-21). But the present study in line with the report by Noguchi and Kawai (22) that SPir was increased in the gracile nucleus and large myelinated fibers in the dorsal root two weeks after unilateral sciatic nerve transection. In addition, Ma and Bisby (23) reported that partial sciatic nerve injury elevated SP levels in spared DRG neurons. They also suggested that the elevated of SP might be involved in the development of neuropathic pain, which commonly follows partial nerve injury. One possible explanation is that the increase of SPir in the present study may be the result of the activation of spared sural nerve and it's spared DRG neurons after exposing to elevated NGF levels. Moreover, there has been proposed interaction between injured and intact nerve fibers that the degeneration of axons is likely to alter Schwann cells supporting intact axons (24). Therefore, the elevated of NGF may be released from Schwann and other endoneurial cells involved in Wallerian degeneration of injured tibial and common peroneal nerves (25). SP is believed to be a neuromediator of nociception in the spinal dorsal horn. SP prescursor is synthesized in the small DRG neurons and transported via axoplasmic transport to the nerve terminal where it is stored and released as SP. This increase in SP may be the result of increased electrical activity due to activation of small C-fibers (26). Although lowthreshold myelinated (A-beta) afferent axons do not normally synthesize neuropeptides, it is well established that they can upregulate neuropeptideY (NPY) after peripheral axotomy (27). The present results also demonstrated the co-localization of CTBir and SPir in medium- and large-size DRG neurons that possess large myelinated axons (Abeta fibers). Therefore, both C- and A-beta fibers in intact sural nerve may be involved in the increase of SP in the spinal dorsal horn after SNI.

On the basis of the use of CTB as a selective tracer for A-beta fibers, neuronal sprouting was shown in the spinal dorsal horn. The present results demonstrated that following SNI, large myelinated (A-beta) primary afferent axons terminate in the spinal dorsal horn, occupying an area that extends from laminae III and IV up to lamina II. There was the sprouting of these A-beta fibers into the spinal territory (lamina II) where postsynaptic targets usually receive only small (C-fiber) afferent fibers.

This study agreed with the previous reports that the sprouting depends on the type and location of axonal injury (3, 13). It was proposed that the sprouting of intact A-fibers may be induced by two phenomena. The first is the injury to those sensory C-fibers that terminate in lamina II and the presence of vacant synaptic sites within the superficial dorsal horn as a consequence of transganglionic degeneration of C-fibers (28, 29). The second is the peripheral axonal injury and the induction of a regenerative capacity in the injured neurons (30), presumably because of upregulation of developmentally regulated growth-related proteins such as GAP-43 (31). GAP-43 is transported to central terminals of injured sensory neurons in lamina II (32). Therefore, peripheral nerve injury may induce both the molecular machinery necessary for growth and provide a denervated area (space) in lamina II (substantia gelatinosa) for the sprouts of A-beta fibers to grow into. This type of growth has been termed conditioned collateral sprouting (3). In this study, it could not conclude that SNI induces the sprouting of injured or intact A-beta fibers because the CTB injection was performed in the sciatic nerve proximal to injury site. Therefore, it's better to inject CTB into the intact sural nerve. However, based on these phenomena, it was also suggested that the sprouting may contribute to neuropathic tactile allodynia (touch-evoked pain) after SNI. In addition, finding of A-beta sprouting in SNI model also supports evidence for using as a direct way of investigating changes in both injured primary sensory neurons and in neighboring intact sensory neurons in the same level (L4-L6) of dorsal root ganglion. It could explain the contribution to the pathophysiology of neuropathic pain. It permits behavioral testing of the noninjured (sural nerve) skin territories adjacent to the denervated (tibial and common peroneal nerves) areas.

Conclusion

The present results indicate that, SNI increased SPir in the DRG and spinal dorsal horn at five weeks after injury. It may due to elevated NGF levels from Schwann and other endoneurial cells involved in Wallerian degeneration. It was also shown that following SNI, the central terminals of cutaneous myelinated afferents, including the large A-beta fibers from the medium- and large- DRG neurons, sprout into lamina II of spinal dorsal horn. This lamina that normally receives nociceptive input was activated by tactile stimuli. It was suggested that this structural reorganization in the central nervous system may contribute to mechanical allodynia associated with neuropathic pain. Therefore, this phenomenon may provide evidence that SNI might be a suitable neuropathic model that may help to explain the pain mediated

by A-fiber following peripheral nerve injury in patients.

Acknowledgment

We would like to express our sincere thanks to Sansanee Noisakorn, PhD for her valuable advice in Confocal microscope at Medical Biotechnology Unit, Siriraj Hospital.

Table 1 The percentage change of mean grey level of SPir expressed as mean \pm SEM from 5 random sections of L4-L6 DRG and spinal dorsal horn per rat was measured by ImageTool analysis program 3.0. Comparison between sham and SNI group was demonstrated. (*Statistical significant at p < 0.001)

Sections	SI	<i>p</i> -value	
	Sham	SNI	P
DRG	100.0±5.5 (10±2.1)	282.0±6.0* (28.2±8.1)	0.000
Spinal dorsal horn	100.0±5.6 (61.4±0.2)	224.8±9.0* (138±2.3)	0.000

- 1. Campbell, J.N., Raja, S.N., Meyer, R.A. and Mackinnon, S.E. Myelinated afferents signal the hyperalgesia associated with nerve injury. *Pain* 1988, 32: 89-94.
- Koltzenburg, M., Torebjork, H.E. and Wahren, L.K. Nociceptor modulated central sensitization causes mechanical hyperalgesia in acute chemogenic and chronic neuropathic pain. *Brain* 1994, 117 (Pt 3): 579-591.
- 3. Woolf, C.J., Shortland, P., Reynolds, M., Ridings, J., Doubell, T. and Coggeshall, R.E. Reorganization of central terminals of myelinated primary afferents in the rat dorsal horn following peripheral axotomy. *J Comp Neurol* 1995, 360: 121-134.
- 4. Leem, J.W., Willis, W.D., Weller, S.C. and Chung, J.M. Differential activation and classification of cutaneous afferents in the rat. *J Neurophysiol* 1993, 70: 2411-2424.
- 5. Grant, G. Projection patterns of primary sensory neurons studied by transganglionic methods: somatotopy and target-related organization. *Brain Res Bull* 1993, 30: 199-208.
- Diamond, J., Holmes, M. and Coughlin, M. Endogenous NGF and nerve impulses regulate the collateral sprouting of sensory axons in the skin of the adult rat. *J Neurosci* 1992, 12: 1454-1466.
- 7. Doubleday, B. and Robinson, P.P. Nerve growth factor depletion reduces collateral sprouting of cutaneous mechanoreceptive and tooth-pulp axons in ferrets. *J Physiol* 1994, 481 (Pt 3): 709-718.

- 8. Liu, C.N. and Chambers, W.W. Intraspinal sprouting of dorsal root axons; development of new collaterals and preterminals following partial denervation of the spinal cord in the cat. *AMA Arch Neurol Psychiatry* 1958, 79: 46-61.
- 9. LaMotte, C.C. and Kapadia, S.E. Deafferentation-induced terminal field expansion of myelinated saphenous afferents in the adult rat dorsal horn and the nucleus gracilis following pronase injection of the sciatic nerve. *J Comp Neurol* 1993, 330: 83-94.
- McNeill, D.L., Carlton, S.M., Coggeshall, R.E. and Hulsebosch, C.E. Denervation-induced intraspinal synaptogenesis of calcitonin generelated peptide containing primary afferent terminals. *J Comp Neurol* 1990, 296: 263-268.
- 11. McMahon, S.B., Lewin, G. and Bloom, S.R. The consequences of long-term topical capsaicin application in the rat. *Pain* 1991, 44: 301-310.
- 12. Pubols, L.M. and Bowen, D.C. Lack of central sprouting of primary afferent fibers after ricin deafferentation. *J Comp Neurol* 1988, 275: 282-287.
- 13. Woolf, C.J., Shortland, P. and Coggeshall, R.E. Peripheral nerve injury triggers central sprouting of myelinated afferents. *Nature* 1992, 355: 75-78.
- Decosterd, I. and Woolf, C.J. Spared nerve injury: an animal model of persistent peripheral neuropathic pain. *Pain* 2000, 87: 149-158.
- 15. Zimmermann, M. Ethical guidelines for investigations of experimental pain in conscious animals. *Pain* 1983, 16: 109-110.
- Woodbury, C.J., Ritter, A.M. and Koerber, H.R. On the problem of lamination in the superficial dorsal horn of mammals: a reappraisal of the substantia gelatinosa in postnatal life. *J Comp Neurol* 2000, 417: 88-102.
- 17. Wilcox, C.D., Dove, S.B., McDavid, W.D. and Greer, D.B. UTHSCSA ImageTool 3.00 ed. San Antonio, Texas: The University of Texas Health Science Center 2002.
- 18. Imbe, H., Okamoto, K., Kadoya, T., Horie, H. and Senba, E. Galectin-1 is involved in the potentiation of neuropathic pain in the dorsal horn. *Brain Res* 2003, 993: 72-83.
- 19. Barbut, D., Polak, J.M. and Wall, P.D. Substance P in spinal cord dorsal horn decreases following peripheral nerve injury. *Brain Res* 1981, 205: 289-298.
- Hokfelt, T., Zhang, X. and Wiesenfeld-Hallin,
 Z. Messenger plasticity in primary sensory neurons following axotomy and its functional implications. *Trends Neurosci* 1994, 17: 22-30.
- 21. Jessell, T., Tsunoo, A., Kanazawa, I. and Otsuka, M. Substance P: depletion in the dorsal horn of rat spinal cord after section of the peripheral processes of primary sensory neurons. *Brain Res* 1979, 168: 247-259.

- Noguchi, K., Kawai, Y., Fukuoka, T., Senba, E. and Miki, K. Substance P induced by peripheral nerve injury in primary afferent sensory neurons and its effect on dorsal column nucleus neurons. *Journal of Neuroscience* 1995, 15: 7633-7643.
- Ma, W. and Bisby, M.A. Increase of preprotachykinin mRNA and substance P immunoreactivity in spared dorsal root ganglion neurons following partial sciatic nerve injury. Eur J Neurosci 1998, 10: 2388-2309
- Murinson, B.B., Hoffman, P.N., Banihashemi, M.R., Meyer, R.A. and Griffin, J.W. C-fiber (Remak) bundles contain both isolectin B4binding and calcitonin gene-related peptidepositive axons. *J Comp Neurol* 2005, 484: 392-402
- 25. Heumann, R., Lindholm, D., Bandtlow, C., Meyer, M., Radeke, M.J., Misko, T.P., Shooter, E. and Thoenen, H. Differential regulation of mRNA encoding nerve growth factor and its receptor in rat sciatic nerve during development, degeneration, and regeneration: role of macrophages. *Proc Natl Acad Sci U S A* 1987, 84: 8735-8739.
- Robert, M.K., Barry, D.G. and Margaret, L.K. Regulatory mechanisms for subtance P in the dorsal horn during a nociceptive stimulus: Axoplasmic transport vs electrical activity. *Brain Research* 1986, 385: 282-290.
- 27. Zhang, X., Meister, B., Elde, R., Verge, V.M. and Hokfelt, T. Large calibre primary afferent neurons projecting to the gracile nucleus express neuropeptide Y after sciatic nerve lesions: an immunohistochemical and in situ hybridization study in rats. *Eur J Neurosci* 1993, 5: 1510-1519.
- Himes, B.T. and Tessler, A. Death of some dorsal root ganglion neurons and plasticity of others following sciatic nerve section in adult and neonatal rats. *J Comp Neurol* 1989, 284: 215-230.
- Kapadia, S.E. and LaMotte, C.C. Deafferentation-induced alterations in the rat dorsal horn: I. Comparison of peripheral nerve injury vs. rhizotomy effects on presynaptic, postsynaptic, and glial processes. *J Comp Neurol* 1987, 266: 183-197.
- 30. Skene, J.H. Axonal growth-associated proteins. *Annu Rev Neurosci* 1989, 12: 127-156.
- 31. Chong, M.S., Fitzgerald, M., Winter, J., Hu-Tsai, M., Emson, P.C., Wiese, U. and Woolf, C.J. GAP-43 mRNA in Rat Spinal Cord and Dorsal Root Ganglia Neurons: Developmental Changes and Re-expression Following Peripheral Nerve Injury. *Eur J Neurosci* 1992, 4: 883-895.
- 32. Woolf, C.J. and King, A.E. Dynamic alterations in the cutaneous mechanoreceptive fields of dorsal horn neurons in the rat spinal cord. *J Neurosci* 1990, 10: 2717-2726.

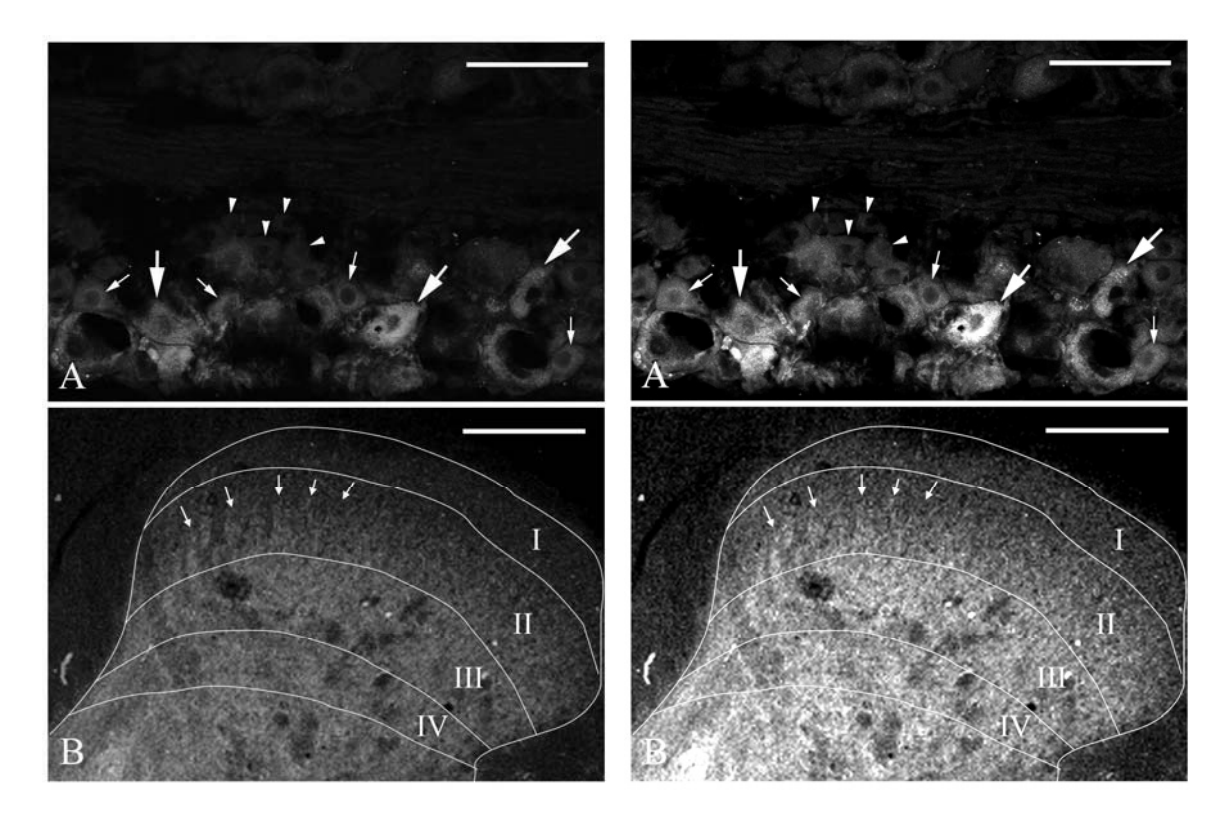


Fig. 1 The confocal merge - image of SPir (green) and CTBir (red) in the rat DRG (fig. 1A) and spinal dorsal horn (fig. 1B) at five weeks after SNI. Co-localization of SP and CTB were demonstrated in medium- (small arrows) to large-sized (large arrows) DRG neurons but not in small- (arrow head) DRG neurons (fig. 1A). Neuronal sprouting was studied in the spinal dorsal horn. In sham operation group, CTBir was present in laminae III and IV (data not shown). In fig.1B, it was shown that SNI results in the sprouting of numerous CTBir- labeled large myelinated sensory axons into laminae II (small arrows), a region that normally receives only C-fiber input. Scale bar: 100 micrometer.

Light and SEM Studies on Leaf Litter Fungi

Leka Manoch¹*, Onuma Jeamjitt¹, Amnat Eamvijarn¹, Tida Dethoup¹, Jitra Kokaew¹, Yupadee Paopun², Pachongchit Poochinya² and Patcharee Umrung²

Department of Plant Pathology, Faculty of Agriculture, Kasetsart University, Bangkok 10900, Thailand

e-mail: agrlkm@ku.ac.th

Abstract

Diversity of leaf litter fungi from various fallen leaves was carried out. Thirteen samples of nine different plants were collected from various locations. The moist chamber, direct isolation and dilution plate methods were used. Fungi were cultivated on 3% malt extract agar and half strength potato dextrose agar. Identification was based on morphological study examined under stereo, light and scanning electron microscopes (Jeol: JSM 5600 LV).

Twenty-nine species of leaf litter were found, including Arthrinium phaeospermum, Bipolaris maydis, Beltrania rhombica, Chaetospermum camelliae, Cladosporium cladosporioides, Colletotrichum capsici, Corynespora sp., Curvularia eragrostidis, Cylindrocladium sp., Ellisiopsis gallesiae, Fusarium semitectum, Gilmaniella humicola, Gyrothrix sp. Helicomyces sp., Lophodermium sp., Memnoniella echinata, Myrothecium verrucaria, Nigrospora sphaerica, Periconia digitata, Pestalotiopsis guepinii, Pithomyces sp., Pseudorobillarda sp., Stachybotrys nephrospora, S. kampalensis, Tetraploa aristata, Torula herbarum, Volutella concentrica and Wiesneriomyces javanicus.

Background

The study on diversity of leaf litter fungi from various host plants were reported (Bills and Polishook 1994, Saravanan, 2004; Tokumasu *et al.*, 1997). Some fungi are common on leaf litter in many studies, while many new fungal taxa have been described from decaying leaves and dead wood (Hughes, 1989). Several species of microfungi can produce bioactive compounds very useful in phamaceutical and agriculture.

Recent contributions of leaf litter fungi in Thailand have been carried out. Manoch al. (2006 a) reported diversity of leaf litter fungi from 7 plants collected from different locations. found 26 genera 31 species of Hyphomycetes, 8 species of Coelomycetes and 5 species of Ascomycetes. Leaf litter fungi have been used as biological control agent against plant pathogenic fungi in vitro. Manoch et al. (2006 a) found that two leaf litter fungi, Myrothecium verrucaria and Ciliochorella sp. could inhibit growth of Alternaria alternata, Colletotrichum capsici, Curvularia lunata and oxysporum in vitro. In addition, morphological study of 42 genera 48 species leaf litter fungi was reported using light microscope (Manoch et al., 2006 b).

Six new species of dematiaceous hyphomycetes from dead wood and bark in New Zealand were illustrated and described (Hughes, 1989).

Microfungi are very important in producing secondary metabolites very useful in agriculture, medicine and pharmaceutical. Saparrat *et al.* (2002) reported laccase activity in *Tetraploa aristata* (

Hyphomycetes) isolated from crude oil-polluted organic matter in Santiago river, Buenose Aires, Aegentina. Namata *et al.* (1997) reported pericosines A, B and macrosphelides from *Periconia byssoides* isolated from seahare (*Aplysia kurodai*). This compound proved to be antitumour to the patient, Kim *et al.* (2004) recorded *Periconia* sp. as a source of bioactive compound, periconisin A, B which is bacteria inhibitor.

In Thailand, Rukachisirikul *et al.*, 2005 found that *Beltrania rhombica* on leaf litter from Tone Nga-Chang water fall, Songkha, produced secondary metabolites which inhibited *Staphylococcus aureus* and *Candida albica*. It is thus very interesting to investigate leaf litter fungi in this tropical region.

The purposes of this study were: 1) to study diversity of leaf litter fungi 2) to isolate and identify leaf litter fungi using morphological features.

Materials and Methods

Thirteen samples of leaf litter were collected from different locations (Table 1). For isolation techniques, the moist chamber, direct isolation, dilution plate methods were used. Fungi were cultivated on 3% malt extract agar and half strength potato dextrose agar. Identification was based on morphological study examined under stereo (Olympus SZ-PZ), light (Olympus BH) and

² Scientific Equipment Center, Kasetsart University Research and Development Institute (KURDI), Bangkok 10900, Thailand

scanning electron microscopes (Manoch et al., 2006 a).

For SEM study, several pieces of decaying leaf tissue with fungal spores on the surface were dissected (5x5 mm²). They were prefixed with 25% glutaraldehyde in 0.1 M potassium phosphate buffer, pH 7.2 for overnight in a refrigerator. They were postfixed with 1% osmium tetroxide in distill water for 2 hours at room temperature, then dehydrated with a series of ethyl alcohol at 10%, 30%, 50% and 100% followed by critical point drying method using liquid carbon dioxide (Hitachi model HCP-2). The treated plant samples with fungal spores were placed on aluminum stub using carbon tape. They were coated with gold and examined under SEM (Jeol: JSM 5600 LV) operating at 10 kV (Paopun et al., 2006).

The preparation for SEM study for resistant or hard-walled spore, small pieces (5x5 mm²) of agar blocks containing mycelium and fungal spores from the culture media were put in an electric dessicator for overnight. They were placed on aluminium stub using carbon tape, coated with gold and examined under SEM (Manoch *et al.*, 2007).

Results and Discussion

Twenty nine genera of microfungi from thirteen samples of nine different fallen leaves namely bamboo, jack fruit, lan thom , banana, Kaffir lime (ma-krut), star gooseberry , Pra du, rose apple, Java plum (wha) were reported (Table 2).

Most species of leaf litter fungi are similar to the previous report (Manoch *et al.*, 2006 a, b). Four new species are recorded, including *Ellisiopsis gallesiae*, *Tetraploa aristata* (figures 5, 6), *Helicomyces* sp. (figure 1) and *Lophodermium* sp. isolated from jack fruit leaf, bamboo leaf and unidentified plant respectively.

Tetraploa aristata was isolated from bamboo leaf sheath, Saraburi province (figures 5-6). It is the first record for Thailand. Saparrat et al. (2002) reported laccase activity in Tetraploa aristata (Hyphomycetes) isolated from crude oil-polluted organic matter in Santiago river (Buenose Aires province, Aegentina). Laccases have been used for transforming and polymerizing or degrading different aromatic pollutants causing environmental damage. Laccases catalyze the direct oxidation of aromatic amines, a wide number of phenolic compounds, including lignin phenolic unit, melanin precursors, chlorophenols, anthraquinone dyes and some polycyclic aromatic hydrocarbon (PHA) such as anthracene.

Wiesneriomyces javanicus was isolated from babana leaf, Saraburi province (figures 2-4). Ellis (1971) reported *W. javanicus* on rotten leaves and twigs; Java. This species is widely distributed in the tropics.

Rukachisirikul *et al.*, 2005 found that the isolate of *Beltrania rhombica*_ on leaf litter from Tone

Nga-Chang water fall, Songkha, southern Thailand could produce new active compound sesquiterpenes, such as beta-eudesmol, pterocarpol, longilobol chrysanthemol, and 5 beta hydroxy-beta-eudesmol that could inhibit *Staphylococcus aureus* and *Candida albica*.

Arthrichitin from *Arthrinium phaeospermum* could decompose chitin, which is the component of hypha and insect. As a result this compound can be developed to fungicide and insecticide (Vijayakumar *et al.*, 1996).

Saravanan (2004) studied fungus diversity on *Neolitsea scrobiculata* (Lauraceae) leaf litter in India. A total of 199 genera and 360 species of microfungi were reported comprising 17 undescribed taxa which include 4 new genera and 13 new species.

Conclusion

Twenty nine genera of leaf litter fungi were found on 9 different host plants. Some species are common leaf litter fungi, whereas 4 genera are new records for Thailand including *Ellisiopsis gallesiae, Helicomyces* sp., *Lophodermium* sp., *Tetraploa aristata*..

Acknowledgment

The authors acknowledge the support from Kasetsart University Research Development Institute for the project "Diversity of microfungi from soil, leaf litter and their applications"

- Bills, G.F. and J.D. Polishook. 1994. Abundance and diversity of microfungi in leaf litter of a lowland rain forest in Costa Rica. Mycologia 86: 187-198.
- 2. Ellis, M.B. 1971. Dematiaceous Hyphomycetes. Commonwealth Mycological Institute,
 - Kew, Surrey, England. 608 p.
- 3. Ellis, M.B. 1976. More Dematiaceous Hyphomycetes. Commonwealth Mycological Institute, Kew, Surrey. 507 p.
- 4. Hughes, S.J. 1989. New Zealand fungi 33. Some new species and new record of dematiaceous hyphomycetes. New Zealand Journal of Botany. 27: 449-459.
- Kim, S., D. Shin, T. Lee and K. Oh. 2004. Periconicins, two new fusicoccane diterpenes produced by an endophytioc fungus *Periconia* sp. with antibacterial activity. J. Nat. Prod. 37: 448-450.
- Manoch, L., J. Kokaew, O. Jeamjitt and T. Dethoup. 2006 a. Leaf litter fungi and studies on antagonistic effect against plant pathogenic fungi *in vitro*. pp. 771-780. *In* The Proceedings of 44th Kasetsart University Annual

- Conference, Subject: plants. Kasetsart University, Bangkok. 30 January 2 February 2006.
- Manoch, L., O. Jeamjitt J. Kokaew and T. Dethoup. 2006 b. Morphological study of leaf litter fungi. Journal of Microscopy Society of Thailand 20(1): 231-232.
- 8. Manoch, L., O. Jeamjitt T. Dethoup, J. Kokaew, A. Eamvijarn, P. Poochinya and Y. Paopun. 2007. Morphological study of some noteworthy fungi from soil and plant. Journal of Microscopy Society of Thailand 21(1): 158-159.
- Paopun, Y., P. Poochinya, P. Umrung and C. Kongpukdee. 2006. Electron microscopic techniques for pollen ornamentation of *Oryza* sativa L. Journal of Microscopy Society of Thailand 20(1): 233-234.
- Rukachaisirikul, V., C. Kaewbumrung, S. Phongpaichi and Z. Hajiwangoh. 2005.
 Eudesmane sesquiterpene from the aquatic fungua *Beltrania rhombica*. Chem. Pharm. Bull. 53(2): 238-240.

- Saparrat, M.C.N., M.N. Cabello and A.M. Arambarri. 2002. Extracellular laccase activity in *Tetraploa aristata*. Biotechnology Letters 24: 1375-1377.
- Saravanan, T. 2004. Studies on the Biodiversity of Microfungi in the Eastern Ghats of Tamilnadu, India. Ph.D. Thesis. University of Madras. India. 201 p.
- Tokumasu, S., Tubaki, K. and Manoch, L. (1997). Microfungal communities on decaying pine needles in Thailand. In:
 Tropical Mycology (eds. K.K. Janardhanan, K.R. Natarajan and D.L. Hawksworth). Science Publishers Inc, USA: 93-106.
- Vijayakumar, E.K.S., K. Roy, S.Chatterjee, S.K. Deshmukh, B.N.Ganguli.,H.W. Fehlhaber and H. Kogler.1996. Arthrichitin, a new cell wall active metabolite from Arthrinium phaeospermum. J. Org. Chem. 61: 6591-6593.

Table 1 Various fallen leaf samples collected from different locations

No	Substrate	Location	Date of	No.	Substrate	Location	Date of
			collection				collection
1	bamboo leaf 1	KU, Bangkok	1 / 6 / 07	8	Java plum leaf	KU, Bangkok	1 / 6 / 07
2	bamboo leaf 2	Angthong	5 / 6 / 07	9	Kaffir lime leaf	Angthong	5 / 6 / 07
3	bamboo leaf 3	Saraburi	14 / 6 / 07	10	Pra du leaf	Angthong	5 / 6 / 07
4	jack fruit leaf	Angthong	5 / 6 / 07	11	bamboo leaf sheath	Saraburi	14 / 6 / 07
5	rose-apple leaf	Bangsue, Bangkok	5 / 6 / 07	12	lan thom leaf	KU, Bangkok	1 / 6 / 07
6	star-gooseberry	Angthong	5 / 6 / 07	13	unidentified plant	Nakhon Si	19 / 10 / 07
7	banana leaf	Saraburi	14 / 6 / 07			Thammarat	

bamboo *Bambusa* sp., banana *Musa sapientum* Pra du *Pterocarpus indicus* jack fruit Artocarpus heterophyllus, Kaffir lime (ma-krut) Citrus hystrix rose apple Eugenia malaccensis, lan thom *Plumeria acuminata*, star gooseberry *Phyllanthus distichus*, Java plum (wha) *Syzygium cumini*

Table 2 Leaf litter fungi isolated from various fallen leaves at different locations

No.	Fungal species	Substrate	No.	Fungal species	Substrate
110.				υ 1	
1	Arthrinium phaeospermum	bamboo leaf 1	16	Lophodermium sp.*	unidentified plant
2	Bipolaris maydis	bamboo leaf 2	17	Memnoniella echinata	Pra du leaf
3	Beltrania rhombica	jack fruit leaf	18	Myrothecium verrucaria	bamboo leaf 3
4	Chaetospermum camelliae	rose apple leaf	19	Nigrospora sphaerica	bamboo leaf 2
5	Cladosporium cladosporioides	jack fruit leaf	20	Periconia digitata	bamboo leaf 3
6	Colletotrichum capsici	star gooseberry	21	Pestalotiopsis guepinii	Java plum leaf
7	Corynespora sp.	banana leaf	22	Pithomyces sp.	bamboo leaf sheath
8	Curvularia eragrostidis	bamboo leaf 1	23	Pseudorobillarda sp.	jack fruit leaf
9	Cylindrocladium sp.	Java plum leaf	24	Stachybotrys nephrospora	lan thom leaf
10	Ellisiopsis gallesiae *	jack fruit leaf	25	Stachybotrys kampalensis	lan thom leaf
11	Fusarium semitectum	Kaffir lime leaf	26	Tetraploa aristata *	bamboo leaf sheath
12	Gilmaniella humicola	bamboo leaf 3	27	Torula herbarum	banana leaf
13	Gyrothrix sp.	bamboo leaf 2	28	Volutella concentrica	bamboo leaf 1
14	Helicomyces sp.*	unidentified plant	29	Wiesneriomyces javanicus	banana leaf
15	Humicola grisea	bamboo leaf 2			

^{*} indicated new record for Thailand

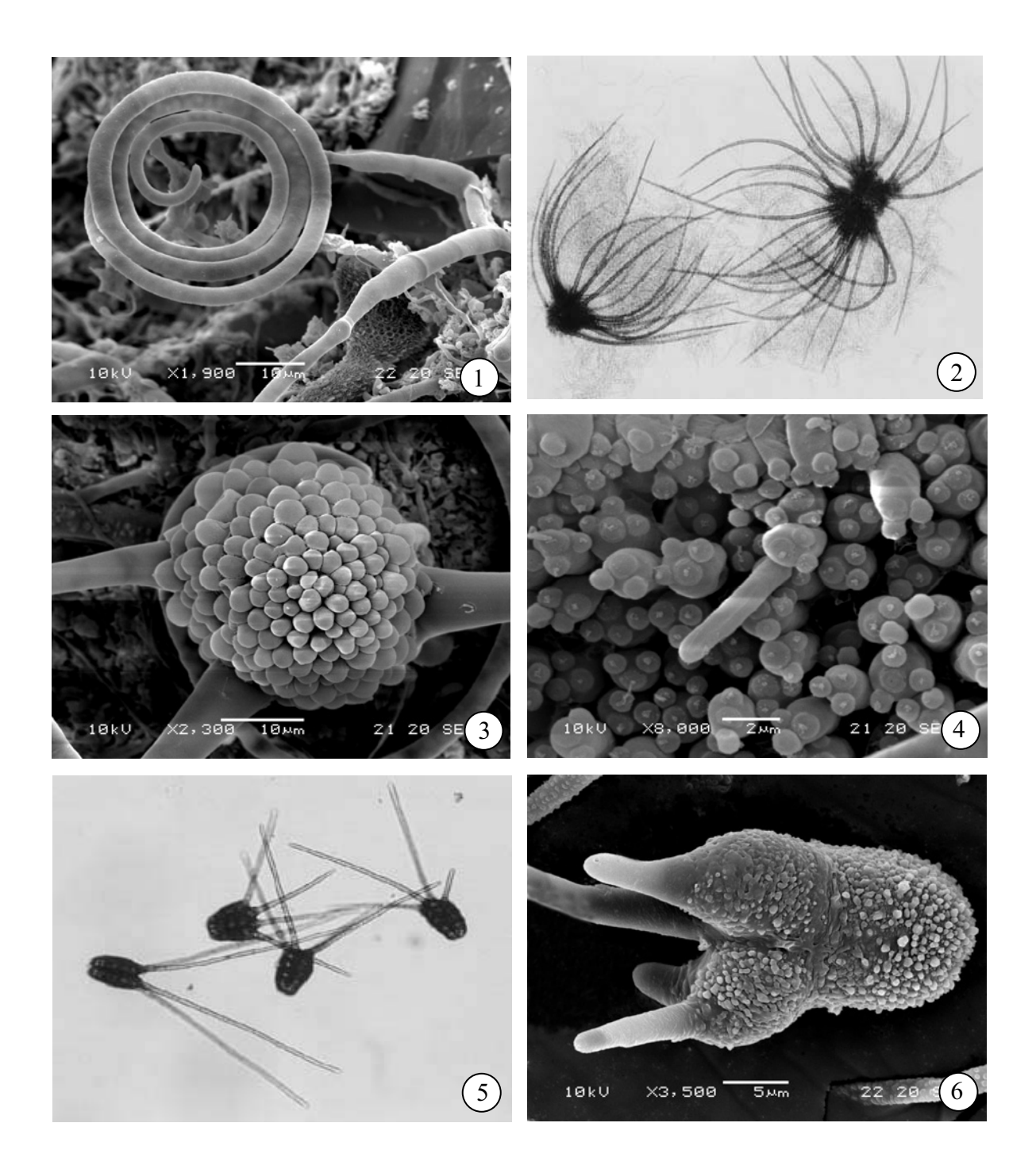


Fig. 1-6 Light and scanning electron microscope photomicrographs of 1. Helicomyces sp. conidiophore and helicoconidium

- 2-4. Wiesneriomyces javanicus conidiophore, conidia and setae
- **5,6.** Tetraploa aristata conidium

Diversity of Arbuscular Mycorrhizal Fungi in Forest Restoration Area of Doi Suthep-Pui National Park, Northern Thailand

Patipan Nandakwang^{1*}, Stephen Elliott² and Saisamorn Lumyong^{2*}

¹Applied Biology Programme, Faculty of Science and Technology, Pibulsongkram Rajabhat University, Phitsanuloke, 65000, Thailand

²Department of Biology, Faculty of Science, Chiang Mai University, Chiang Mai, 50200, Thailand e-mail: patipan263@hotmail.com; scboi009@chiangmai.ac.th

Abstract

Arbuscular Mycorrhizal (AM) fungal diversity was surveyed in the forest restoration area of Doi Suthep-Pui National Park, northern Thailand. Twenty four indigenous tree species, used for forest restoration in a degraded watershed area were examined. Rhizosphere soil samples were collected and AM spores were counted and identified morphologically. AM spores were found in the rhizosphere soils of all tree species. Twenty one AM species were identified: *Acaulospora* (6 species), *Glomus* (12 species) and *Scutellospora* (3 species). AM fungi belonging to the genera *Glomus* and *Acaulospora* were dominant. Abundant species present were *Acaulospora elegans*, *Glomus multicaule* and *Scutellospora pellucida*. These results showed that all 24 indigenous tree species were associated with AM fungi and some AM species had a broad host range.

Background

The tropical forests of Doi Suthep-Pui National Park are one of the most important watershed areas which composed of a number of indigenous tree species. Deforestation within the national park has had adverse consequences on biodiversity and environmental quality. One method of forest restoration, which involves planting mixtures of several indigenous tree species, has been used to counteract this problem (Goosem and Tucker, 1995; FORRU, 2006). Many indigenous species were selected and tested in the experimental plot, established in the north of national park (Elliott et al., 2003). AM fungi are one of the beneficial soil microorganisms that play a crucial role in the mineral nutrition of forest trees (Koide and Mosse, 2004). Information on the capacity of indigenous tree species in association with AM fungi is very important to forest restoration. The purpose of this study was to obtain information on the diversity of AM fungi associated with indigenous tree species in the forest restoration plot.

Materials and Methods

Among the planted tree species in forest restoration plot, 24 potential indigenous species were selected for study. All tree species are reported to be multipurpose and suitable for acceleration of the forest regeneration. Rhizosphere soil samples (about 500 g) of each indigenous species were collected and stored at 4°C until analyzed. AM spores were extracted from 100 g air-dried soil samples by wet-sieving and 50% sucrose centrifugation (Brundrett *et al.*, 1996). Spores were recovered by filtering through a 53 μm sieve onto filter paper. The intact spores on filter

paper were counted under a stereomicroscope (Olympus SZ40). Spores were mounted on microscopic slides in polyvinyl lactic acid (PVA), with or without Melzer's reagent (Morton, 1988) and identified according to morphological characteristics of the originally published species descriptions under a light microscope (Olympus CH30). Light microscopic photographs were taken under an Olympus BX61.

Results and Discussion

The results of our study on the AM fungal diversity in the forest restoration area of Doi Suthep-Pui National Park showed that all 24 indigenous tree species are associated with AM fungi. Spores of AM fungi were found in the rhizosphere soils of all individual tree species. This reflects the mycotrophic nature of the plant species studied and the ability of AM fungi in soils to associate a wide range of host species. It has been reported that many tree species are highly associated with AM fungi (Janos, 1980; Onguene and Kuyper, 2001). Twenty one AM species were identified based on morphological characteristics of their spores according to published descriptions (Table 1). The diversity of AM species was varied among the different tree species (Table 2). Most of the isolated species belonged to the family Glomaceae, all of which were Glomus (12 species, 49.3%). Abundant species present was G. multicaule (14.2%) (figure 1). Six species were in the family Acaulosporaceae, all of which were in the genus Acaulospora (43.6%). Abundant species present was A. elegans (39.2%) (figure 2). Three species were members of

Gigasporaceae and belonged to the genus Scutellospora (7.1%). Abundant species present was S. pellucida (5.5%) (figure 3). Species in the genera Archaeospora, Paraglomus, Entrophospora and Gigaspora were not found. AM fungi belonged to the genera Glomus and Acaulospora were dominant. This fact must be related to their sporogenous characteristics, i.e. Glomus and Acaulospora species usually take a short time to produce small spores, compared with the large spores of Gigaspora and Scutellospora species in the same environment (Hepper, 1984; Bever et al., 1996). A. elegans, G. multicaule and S. pellucida were the most commonly encountered species. This suggests that these species have a widespread and broad host range.

Conclusion

In the forest restoration area of Doi Suthep-Pui National Park, all surveyed indigenous tree species were associated with AM fungi. The AM fungal diversity in the plant rhizospheres was variable among the different tree species. Twenty one AM species were identified as 3 genera and 12 species of *Glomus*, 6 species of *Acaulospora* and 3 species of *Scutellospora*. *Glomus* and *Acaulospora* were the dominant genera. The present study obtains the information on the AM association of 24 potential indigenous trees used to restore tropical forest of Doi Suthep-Pui National Park.

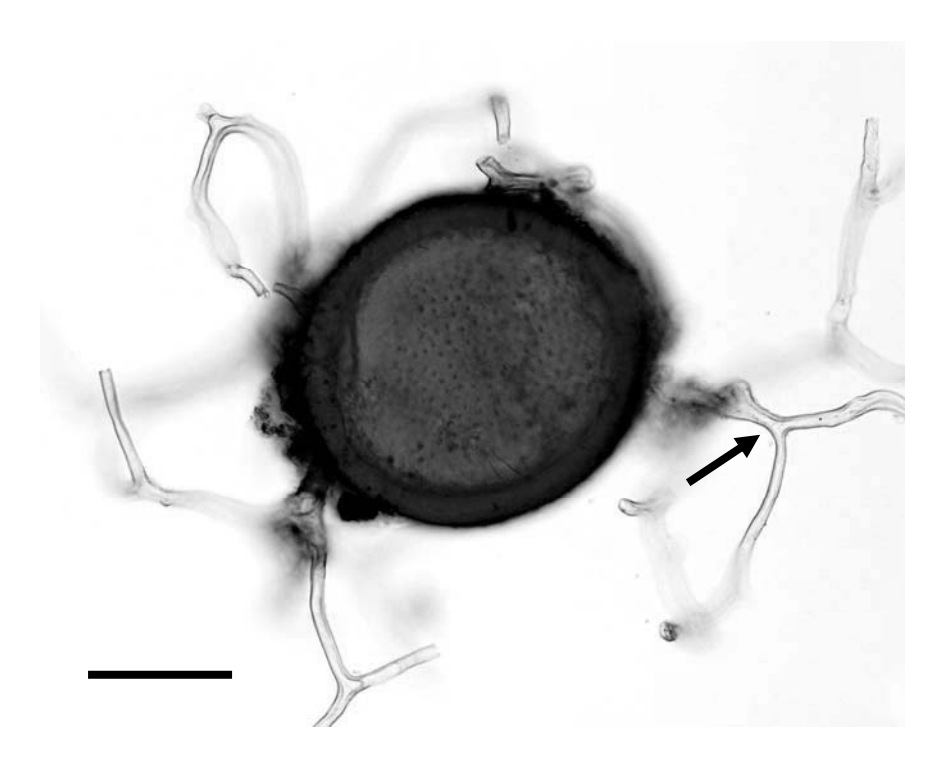
Acknowledgment

This research was partially supported by Pibulsongkram Rajabhat University. We thank Mr. Cherdsak Kuarak and volunteers for helping collect the samples.

References

1. Bever JD, Morton JB, Antonovics J, Schultz PA. Host-dependent sporulation and species diversity of arbuscular mycorrhizal fungi in a mown grassland. *J. Ecol* 1996, 84: 71-82.

- Brundrett M, Bougher N, Dell B, Grove T, Malajczuk N. Working with Mycorrhizas in Forestry and Agriculture. ACIAR Monograph 32, ACIAR, Canberra, Australia 1996, pp: 374.
- 3. Elliott S, Navakitbumrung P, Kuarak C, Zangkum S, Anusarnsunthorn V, Blakesley D. Selecting framework tree species for restoring seasonally dry tropical forests in northern Thailand based on field performance. *For. Ecol. Manage* 2003, 184: 177-191.
- 4. FORRU. How to Plant a Forest: The Principles and Practice of Restoring Tropical Forests. Forest Restoration Research Unit. 1st Edn., Biology Department, Science Faculty, Chiang Mai University, Thailand 2006, pp: 200
- 5. Goosem SP, Tucker NIJ. Repairing the Rainforest-Theory and Practice of Rainforest Re-establishment in North Queensland's Wet Tropics. *Wet Tropics Management Authority, Cairns* 1995, pp. 71.
- Hepper CM. Isolation and Culture of VA Mycorhizal (VAM) Fungi. In: VA Mycorrhizae. Powell, C.L. and D.J. Bagyaraj (Eds.), CRC Press, Florida, USA 1984, pp: 95-112.
- 7. Janos DP. Vesicular arbuscular mycorrhizae affect lowland tropical rain forest plant growth. *Ecology* 1980, 61: 151-162.
- 8. Koide RT, Mosse B. A history of research on arbuscular mycorrhiza. *Mycorrhiza* 2004, 14: 145-163.
- 9. Morton JB. Taxonomy of VA mycorrhizal fungi: Classification, nomenclature, and identification. *Mycotaxon* 1988, 37: 267-324.
- Onguene NA, Kuyper TW. Mycorrhizal associations in the rain forest of South Cameroon. For. Ecol. Manage 2001, 140: 277-287.



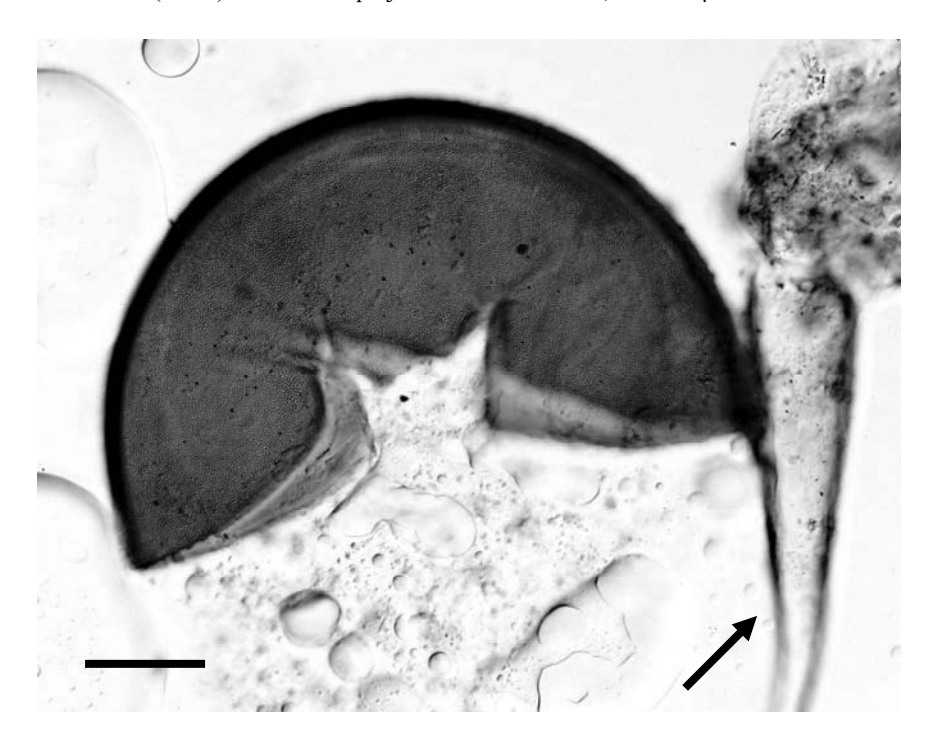


Fig. 2 Acaulospora elegans: Craked spore with sporiferous saccule (arrow) and crowded spines on the surface, bar = $50 \mu m$.

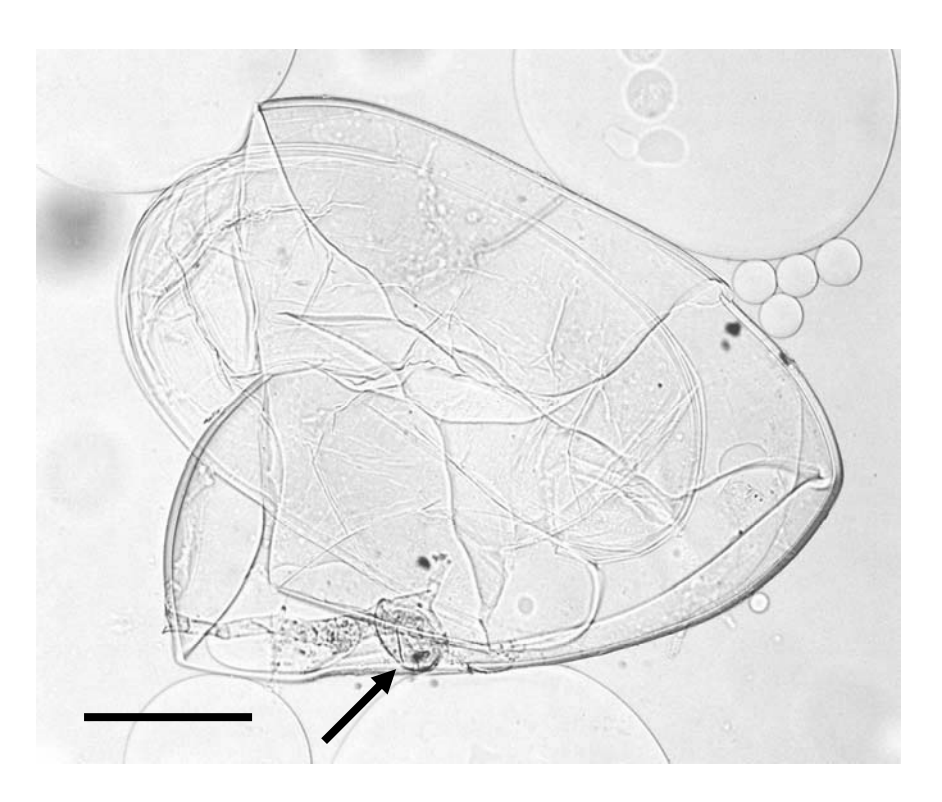


Fig. 3 Scutellospora pellucida: Cracked hyaline spore with hyaline bulbous subtending hypha, bar = $50~\mu m$.

Table 1 Diversity of AM fungi from the rhizosphere soils of 24 indigenous tree species in the forest restoration area of Doi Suthep-Pui National Park, northern Thailand.

Code of AM species	Genus	Species
	Acaulospo	ora -
1	•	A. bireticulata Rothwell & Trappe
2		A. elegans Trappe & Gerd.
3		A. foveata Trappe & Janos
4		A. laevis Gerd. & Trappe
5	2	A. mellea Spain & Schenck
6	2	A. scrobiculata Trappe
	Glomus	
7		G. aggregatum Schenck & Smith
8		G. ambisporum Smith & Schenck
9		G. clavisporum Trappe
10		G. coremioides Berk. & Broome
11		G. intraradices Schenck & Smith
12		G. microaggregatum Koske, Gemma & Olexia
13		G. microcarpus Iqbal & Bushra
14		G. mosseae (Nicol. & Gerd.) Gerd. & Trappe
15		G. multicaule Gerd. & Bakshi
16		G. rubiforme Gerd. & Trappe
17		G. sinuosum Gerd. & Bakshi
18		G. viscosum Nicol.
	Scutellosp	ora
19	_	S. gregaria (Schenck & Nicol.) Walker & Sanders
20	,	S. heterogama Walker & Sanders
21	Ä	S. pellucida (Nicol. & Schenck) Walker & Sanders

Table 2 Diversity of AM fungi found in the rhizospheres of 24 indigenous tree species in the forest restoration area of Doi Suthep-Pui National Park, northern Thailand.

Indigenous tree species	AM species*	
Acrocarpus fraxinifolius Wight ex Arn. (Caesalpinioideae)	3, 4, 14, 15	
Balakata baccata (Roxb.) Ess. (Euphorbiaceae)	12, 20	
Castanopsis acuminatissima (Bl.) A. DC. (Fagaceae)	1, 15	
Erythrina subumbrans (Hassk.) Merr. (Papilionoideae)	2, 7, 12, 19	
Ficus altissima Bl. (Moraceae)	2, 6, 10	
Ficus benjamina L. var. benjamina (Moraceae)	6, 19, 20	
Ficus glaberrima Bl. var. glaberrima (Moraceae)	16	
Ficus hispida L. f. var. hispida (Moraceae)	2, 5, 16, 17	
Ficus racemosa L. var. racemosa (Moraceae)	2, 8, 14, 16, 18	
Ficus subulata Bl. var. subulata (Moraceae)	2, 14, 16, 20	
Glochidion kerrii Craib (Euphorbiaceae)	21	
Gmelina arborea Roxb. (Verbenaceae)	2, 6, 13, 15	
Heynea trijuga Roxb. ex Sims (Meliaceae)	2, 3, 8, 10, 20	
Hovenia dulcis Thunb. (Rhamnaceae)	2, 7, 15	
Macaranga denticulata (Bl.) MA. (Euphorbiaceae)	9, 10, 16, 20	
Machilus bombycina King ex Hk.f. (Lauraceae)	2, 10, 16, 20	
Melia toosendan Sieb. and Zuc. (Meliaceae)	2, 9, 20	
Michelia baillonii Pierre (Magnoliaceae)	16, 17	
Nyssa javanica (Bl.) Wang. (Nyssaceae)	6, 15, 20	
Prunus cerasoides D. Don (Rosaceae)	7, 10, 13, 15, 16	
Rhus rhetsoides Craib (Anacardiaceae)	2, 6, 13, 16	
Sapindus rarak DC. (Sapindaceae)	2, 20	
Sarcosperma arboreum Bth. (Sapotaceae)	10, 11, 20	
Spondias axillaris Roxb. (Anacardiaceae)	15	

 $^{^{*}}$ Numbers in column refer to the codes of AM species in Table 1.

Some Hematological Values and Ultrastructure of Blood Cells in *Piper sarmentosum* Roxb. and *Tinospora crispa* Miers ex Hook. F & Thoms. Treated Diabetic Rats

Areeya Suchantabud^{1*}, Chusri Talubmook^{1,2}, Sanong Chomko¹, Nual-anong Narkkong³

¹ Department of Biology, Faculty of Science, Mahasarakham University,

Maha Sarakham 44150, Thailand

² Faculty of Environment and Resource Studies, Mahasarakham University, Maha Sarakham 44150, Thailand

³ Central Instrumentation Unit, Faculty of Science, Mahasarakham University,

Maha Sarakham 44150, Thailand

e-mail: areeya30@hotmail.com

Abstract

The present study was carried out to investigate the effects of the powder from *Piper sarmentosum* Roxb. leaves and *Tinospora crispa* Miers ex Hook. F & Thoms. stems on packed cell volume, hemoglobin concentration, red and white blood cell counts and ultrastructure of blood cells in streptozotocin-induced diabetic rats. The experiments were performed by daily oral administration of the powder the from *P. sarmentosum* and *T. crispa* at a dosage of 250 mg/kg to diabetic rats for eight weeks. The results showed that the packed cell volume, hemoglobin concentration and red and white blood cell counts in diabetic rats received the powder from *P. sarmentosum* and *T. crispa* were not different, but the hemoglobin concentration and red blood cell count were significantly higher than control. However, the white blood cell count was significantly less than controls. Furthermore, the length of the red blood cells in rats treated with the powder from *T. crispa* was longer than those treated with *P. sarmentosum*. However, they were not different from controls. In contrast, the width of the red blood cells in rats treated with *P. sarmentosum* and *T. crispa* were not different and were not different from controls.

The findings indicated that long-term administration of the powder from these plants changed some hematological values in diabetic rats compared with controls.

Background

Diabetes mellitus is a common metabolic disorder. It is often associated with several complications, such as cataract and retinopathy, gastrointestinal diseases with a high recurrence of pancreatitis, neuropathy, nephropathy, myocardial, and dermatitis, as well as various infectious diseases, both in human and in veterinary medicine. Hematological complications consist mainly of abnormalities in the function, morphology and metabolism of erythrocytes, leukocytes and platelets [1]. By the year 2025, the World Health Organization (WHO) predicts that 300 million people will have diabetes mellitus. Treatment of diabetes mellitus and its complications in the recent context have focused on the usage of plant extracts [2]. Piper sarmentosum Roxb. (Piperaceae, Thai name: Chaplu) The leaves of P. sarmentosum are used as food and traditional medicine in Thailand [3]. Tinospora crispa Miers ex Hook. F & Thoms. (Menispermaceae, Thai name: Boraphet), a plant used to treat diabetics, was able to reduce blood glucose level in moderately diabetic rats, and the hypoglycaemic effect was probably due to its

insulinotropic activity [4]. The effects of P. sarmentosum and T. crispa on hematological values and ultrastructure of blood cells have not yet been reported. Therefore, the purpose of the present study was conducted to examine some hematological values and ultrastructure of blood cells in diabetic rats treated with P. sarmentosum and T. crispa.

Materials and Methods

Extract Preparation

Fresh *P. sarmentosum* leaves and *T. crispa* stems were collected locally, Botanical identification was performed by Dr. Sanong Chomko in Department of Biology, Faculty of Science, Mahasarakham University. The plants were sliced into small pieces, air dried at ambient temperature and ground into powder form.

Animals

Thirty male albino Wistar rats weighting 200-250 g purchased from the Animal Center at Mahidol University in Nakhon-pathom were using in this study. They were acclimatized and housed in an air conditioned room at 22-28 °C for five days. The were fed with standard chow and watered ad libitum prior to the commencing experiments. The rats used in the present study were maintained in accordance with the guidelines of the Committee on Care and Use of Laboratory Animal Resource, National Research Council Thailand. The experiments performed on the rats were conducted in accordance with the advice of the Institutional Animal Care and Use Committee MSU.

Diabetes Induction

The rats were injected intraperitonealy with a single dose of 65 mg/kg streptozotocin (STZ, Sigma Chemicals, St. Louis, MO) freshly dissolved in 20 mM citrate buffer (pH 4.5). After STZ injection, they were provided with a 2% sucrose solution as their drink for 48 hours to alleviate the severity after initial hypoglycaemic phase. Blood glucose levels were assessed 48 hours after STZ injection to confirm the diabetic stage. Only rats with blood glucose at or above 200 mg/dl were used in the experimentation [5].

Experimental Design

The experiment consisted of 5 groups (6 rats per group); Group 1: Control given 2 ml distilled water, Group 2: Streptozotocin induced diabetic given 2 ml distilled water, Group 3: Diabetic rats treated with 0.25 mg/kg glibenclamide, Group 4: Diabetic rats treated with 250 mg/kg of *P. sarmentosum* powder and Group 5: Diabetic rats treated with 250 mg/kg of *T. crispa* powder.

The rats were treated once daily for eight weeks. At the end of the experiment the rats were anesthetized with ether and blood samples were drawn from the tail vein of each animal to determine the hematological values and ultrastructure of blood cells.

Hematological Values

The packed cell volume was determined by microhematocrit centrifugation, centrifuged at 1,500 rpm for 5 min. Hemoglobin concentration was measured using Sahli method. Total red blood cells and white blood cells were counted manually using hematocytometer. Red blood cells were diluted using Gower's solution but total white blood cells using Turk's solution [6].

Ultrastructure of Blood Cells

Ultrastructure of blood cells were studied using Transmission Electron Microscope (TEM). For TEM technique, blood samples were centrifuged in capillary tubes at 1,500 rpm for 15 min. Buffy coats were dropped in 2.5% glutaraldehyde in 0.1 M phosphate buffer, pH 7.2 overnight at 4 °C and then washed in the same buffer. They were postfixed with 1% osmium tetroxide for 2 h, rinsed by distilled water, dehydrated in 20%, 40%, 60%, 80%, 100% and 100% acetone and embedded in Epon resin. Lead citrate and uranyl acetate stained ultrathin sections on copper grid were examined with TEM (JEM 1230) [7].

Statistical Analysis

The results of hematological values were presented as the mean \pm standard error of the mean (SEM). Comparions were made between control and treatment groups using one-way analysis of variance (ANOVA) followed by Duncan's New Multiple Range Test. Values of p < 0.05 were regarded as statistical significant.

Results and Discussion

The results of hematological values as well as the the length and the width of red blood cells of rats in control and treatment groups are given in Table 1 and 2, respectively.

Table 1 showed that the packed cell volume from all experimental groups were not different. The hemoglobin concentration from diabetic rats treated with P. sarmentosum and T. crispa were not different and were not different from rats treated with glibenclamide but were significantly (p < 0.05) more than controls and diabetic controls. The red and white blood cell counts of rats treated with both types of the plant powders were not different but were significantly (p < 0.05) different from controls. However, the red blood cells count of the rats treated with plant powder was significantly greater than that in controls (p < 0.05), while the white blood cells count was significantly less than that in controls (p < 0.05).

Table 2 the length of the red blood cells from T. crispa treated rats was significantly (p < 0.05) longer than that from P. sarmentosum treated rats but it was similar to those from controls, diabetic controls and diabetic rats treated with glibenclamide. The width of red blood cells from P. sarmentosum treated rats was not different from controls, diabetic rats treated with glibenclamide and diabetic rats treated with T. crispa, but was significantly (p < 0.05) less than that from diabetic controls.

These results showed the hematological effect of powder from *P. sarmentosum* and *T. crispa* in diabetic rats. However, compare of hematological

values treated with extract from *Morus alba* in diabetic rats; Packed cell volume 47.17±1.02 %, Hemoglobin concentration 21.80±0.20 g/dl and RBCs 7.48±0.64 x10⁶cell/μl [6] were lower than rats treated with *P. sarmentosum* and *T. crispa*. Hemoglobin is a major constituent of erythrocytes which function in oxygen transport and can therefore be used to evaluate the physical condition of an animal [8]. In addition, male albino rats treated with 50 mg/kg *Teucrium polium* extract; RBCs 6.23±0.82 x10⁶/mm³, WBCs 15.35±3.50 x10³/mm³ and HCT 37.52±2.68 % [9].

TEM micrographs showed that the ultrastructure of red blood cells from the diabetic controls was clearly different from the controls (figure 1). The hemoglobin protein contents in the red blood cells of control rat were homogenous (figure 1 A-B), but the aggregation of hemoglobin was clearly found in the red blood cells of the diabetic controls shown by the electron loose and electron dense area (figure 2 A-B). The ultrastructure of red blood cells from glibenclamide treated *P. sarmentosum* treated were similar to control than *T. crispa* treated rats rats (figure 1 A-B, 3 A-B, 4 A-B, 5 A-B).

The ultrastructure of leukocyte i.e. lymphocyte, monocyte, neutrophil and eosinophil of all rat group were not different (figure 2).

Conclusion

In conclusion, the packed cell volume, hemoglobin concentration, red and white blood cell counts in diabetic rats received the powder from P. sarmentosum leaves and T. crispa stems were not different. Furthermore, the width but not the length of red blood cells in rats treated with the powder from P. sarmentosum and T. crispa were not different and not different from controls. The ultrastructure of red blood cells in controls and P. sarmentosum and T. crispa treated rats were not different but were different from diabetic controls. Moreover, the ultrastructure of white blood cells in rats treated with P. sarmentosum, T. crispa and glibenclamide and controls were not different. The findings indicated that long-term administration of the powder from two types of the plant changed some hematological values and ultrastructure in diabetic rats compared with controls.

Acknowledgment

The authors would like to thank the Development Research Division, Mahasarakham University, Thailand for partly research financial supports.

References

- 1. Comazzi, S., Spagnolo, V. and Bonfanti, U. Erythrocyte changes in canine diabetes mellitus: in vitro effects of hyperglycaemia and ketoacidosis. *J. Comp Clin Path.* 2004, 12: 199-205.
- 2. Kamalakkannan, N. and Mainzen, Prince P. S. Rutin improves the antioxidant status in streptozotocin-induced diabetic rat tissues. *J. Mol Cell Biochem.* 2006, 293: 211-219.
- 3. Peungvicha, P., Thirawarapan, S. S., Temsiririrkkul, R., Watanabe, H., Prasain, J. K. and Kadota S.. Hypoglycemic effect of the water extract of *Piper sarmentosum* in rats. *J. Ethnopharmacol.* 1998, 60: 27-32.
- 4. Noor, H. and Ashcroft, S. J. H. Pharmacological characterisation of the antihyperglycaemic properties of *Tinospora crispa* extract. *J. Ethnopharmacol.* 1998, 62: 7-13.
- 5. Talubmook, C., Forrest, A. and Parsons, M. Streptozotocin-induced diabetes modulates presynaptic and postsynaptic function in the rat ileum. *Eur. J. Pharmacol.* 2003, 469: 153-158
- 6. Chomko, S. and Talubmook, C. Effect of leaf extracts from *Morus alba* and *Annona squamosa* on haematological values in diabetic rats. *J. Sci and Technol MSU*. 2007, 26:167-173.
- 7. Ponsen, S., Narkkong, N-A. and Angwanich, W. Morphological and ultrastructural observations on the blood cells of sand lizards (*Leiolepis belliana* Rubritaeniata) mertens 1961. *J. Anim Vet. Adv.* 2007, 6(4): 522-527.
- 8. Chang, G-R., Mao, F. C., Yang, C-C. and Chan, F-T. Hematological profiles of the formosan black bear (*Ursus thibetanus formosanus*). *J. Zool. Studies*. 2006, 45: 93-97.
- 9. Khleifat, K., Shakhanbeh, J. and Tarawneh, K. The chronic effects of *Teucrium polium* on some blood parameters and histopathology of liver and kidney in the rats. *Turk J. Biol.* 2002, 26:65-71.

Table 1 Hematological values of controls, diabetic controls, diabetic rats treated with glibenclamide and diabetic rats treated with P. sarmentosum and T. crispa.

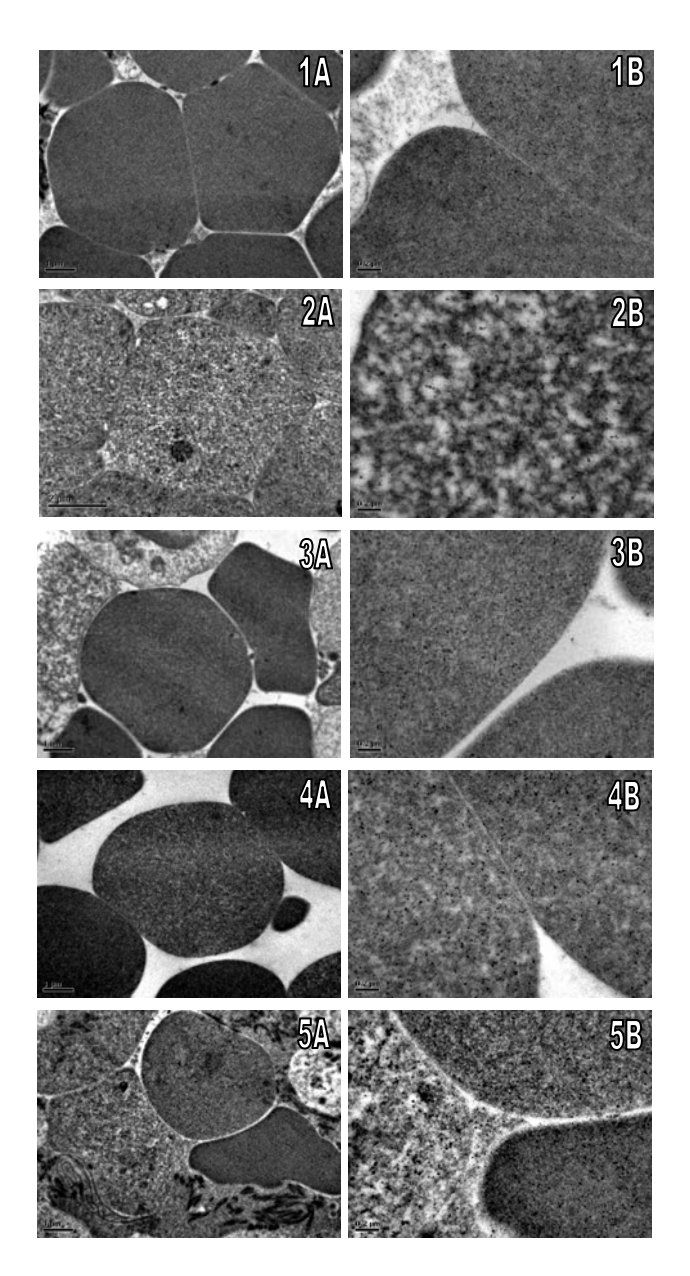
Group	Packed cell volume (%)	Hemoglobin concentration (g/dl)	Red blood cells (x10 ⁶ cell/μl)	White blood cells (x10 ³ cell/μl)
controls	52.00 <u>+</u> 1.37	23.00 ± 0.44^{a}	7.35 <u>+</u> 0.10 bc	9.40 <u>+</u> 0.92 bc
diabetic controls	51.20 <u>+</u> 0.96	23.00 ± 0.94^{a}	5.62 <u>+</u> 0.46 ^a	7.50 <u>+</u> 1.09 ab
glibenclamide	50.40 <u>+</u> 0.40	25.20 <u>+</u> 1.06 ^{ab}	6.97 <u>+</u> 0.18 ^b	10.02 <u>+</u> 0.70 °
P. sarmentosum	50.60 <u>+</u> 0.50	27.00 <u>+</u> 0.31 ^b	8.06 <u>+</u> 0.14 ^{cd}	6.58 <u>+</u> 0.42 ^a
T. crispa	49.60 <u>+</u> 0.24	26.20 <u>+</u> 0.37 ^b	8.82 <u>+</u> 0.25 ^d	5.67 <u>+</u> 0.17 ^a

Means \pm SEM within the same column followed by the different letters are significantly different at p<0.05.

Table 2 Length and width of the red blood cells in controls, diabetic controls, diabetic rats treated with glibenclamide and diabetic rats treated with P. sarmentosum and T. crispa (measured from the thick section).

Group (20 cells/ rat)	Length (µm)	Width (µm)
Controls (n=3)	5.40 ± 0.10^{ab}	4.52+0.11 ^a
diabetic controls (n=3)	5.62 <u>+</u> 0.10 ^b	$4.92 + 0.08^{b}$
Glibenclamide (n=3)	5.57 <u>+</u> 0.11 ^b	$4.72 + 0.11^{ab}$
P. sarmentosum (n=3)	5.17 <u>+</u> 0.12 ^a	$4.45 + 0.10^{a}$
<i>T. crispa</i> (n=3)	5.52 <u>+</u> 0.11 ^b	4.62+0.13 ^{ab}

Means \pm SEM within the same column followed by the different letters are significantly different at p<0.05.



 $\label{eq:Fig.1} \begin{tabular}{ll} Fig.1 Ultrastructrue of red blood cells wistar rats after 8 weeks; group 1 : controls, group 2 : diabetic controls, group 3 : glibenclamide, group 4 : P. sarmentosum and group 5 : T. crispa A; whole cell at 4,500x, B; high magnification at the same area of A (20,000x) \\ \end{tabular}$

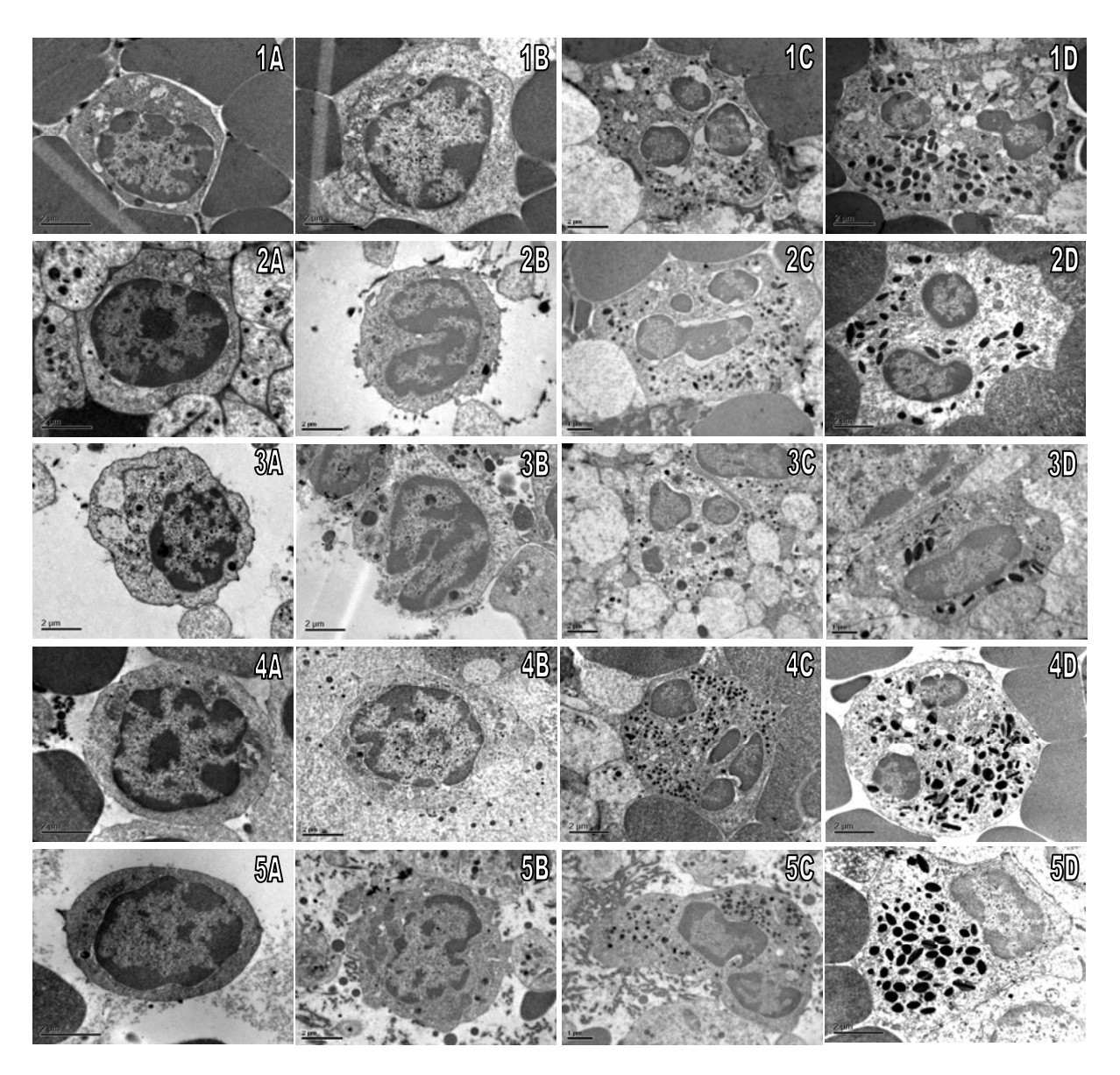


Fig.2 Ultrastructrue of white blood cells of wistar rats after 8 weeks; group 1 : controls; group 2 : diabetic controls; group 3 : glibenclamide; group 4 : P. sarmentosum and group 5 : T. crispa including A : lymphocyte, B : monocyte, C : neutrophil and D : eosinophil.

Hematological Values and Morphological Observation of Blood Cells in Balloon Frog, *Glyphogloossus molossus*

Siripan Ponsen¹, Nual-anong Narkkong², Supaporn Pamok¹, Kunyarut Sappaso² and Worapol Aengwanich¹ Stress and Oxidative Stress Research Unit, Faculty of Veterinary Medicine and Animal

Science Mahasarakham University, Maha Sarakham 44000, Thailand

² Central Instrumentation Unit, Faculty of Science, Mahasarakham University, Maha Sarakham 44150, Thailand

e-mail: siri.pan.p@hotmail.com

Abstract

Eighteen balloon frogs, *Glyphogloossus molossus* were collected from forest and rice field in Maha Sarakham Province, northeastern Thailand during March-May, 2007. Hematological values, morphological structures and blood cell sizes were determined under light and electron microscope examination. The mean of packed cell volume, hemoglobin concentration, total red blood cells, total white blood cells, mean corpuscular volume, mean corpuscular hemoglobin, mean corpuscular hemoglobin concentration, percentage of lymphocyte, monocyte, heterophil, eosinophil and basophil of balloon frogs were 26.94 ± 1.42 %, 8.62 ± 0.70 g/dL, $1.04\pm0.18 \times 10^6$ cells/µl, $1.37\pm0.16 \times 10^3$ cells/µl, 409.29 ± 78.17 fL, 142.11 ± 34.18 pg, 32.96 ± 13.15 g/dL, 41.62 ± 3.07 %, 22.77 ± 1.89 %, 26.27 ± 2.25 %, 1.07 ± 0.29 % and 8.27 ± 0.85 %, respectively. Moreover, the mean of erythrocyte length and width, erythrocyte nucleus length and width, diameter of lymphocyte, monocyte, heterophil, eosinophil, basophil, and thrombocyte of balloon frogs were 15.42 ± 1.04 and 11.47 ± 0.82 ; 6.06 ± 0.78 and 4.02 ± 0.45 ; 13.89 ± 3.34 , 8.56 ± 2.74 , 13.76 ± 3.59 , 15.00 ± 7.08 , 6.90 ± 2.03 and 12.29 ± 2.52 micrometers, respectively. Finally, the morphologic features of blood cell characteristics of balloon frogs were similar to those of other species of frogs.

Background

Balloon frogs, Glyphogloossus molossus is an important protein source for people in northeastern part of Thailand which are caught from forest and rice field for making the food. Balloon frogs are classified in kingdom Animalia, phylum Chrodata, class Amphibia, order Anura, family Microhylidae, species Glyphogloossus and genus spp. Glyphogloossus molossus. At beginning of rainy season, Asian painted frogs leave from their holes for breeding and people catch them for making food. At present, the habitats of balloon frogs have been on the decrease. Whereas, data regarding their blood cell characteristics, blood cell sizes and hematological values have not been reported. therefore, the objective of this study was to establish the blood cell characteristics, blood cell dimension and hematological values of balloon frogs. Basic knowledge from this study is important for hematological research, conservation, clinical diagnosis and in-depth study of this frog.

Materials and Methods

Animals: Eighteen balloon frogs were captured from forest and rice field in Maha Sarakharm Province, northeastern part of Thailand during March–May 2007, and then took to Laboratory of Faculty of Veterinary Medicine and Animal

Science, and Central Instrumentation Unit, Faculty of Science, Mahasarakham University.

Hematological techniques: 0.5 milliliter of blood sample were collected from heart using a 1 ml syringe, 26-gauge needle and 1.5 inch of length then placed in microtube with EDTA for determining hematological values. The samples were cooled to approximately 4 °C, using icepacks and transferred to the laboratory within 2 hours after blood collection. Differential white blood cell counts were performed on blood films prepared, fixed in 95% ethyl alcohol for 5 min and then were stained with Giemsa-Wright' stain and then took photos with camera under light microscope. Blood cell dimensions determined by using a stage and ocular micrometer. The packed cell volume (PCV) was determined after the blood had been transferred to microcapillary tubes and centrifuged at 2,500g for 5 min. Total white blood cell counts were determined manually with the improved Neubauer counting chamber after the blood was diluted with Natt and Herrick's solution. Total red blood cell counts were performed by diluting balloon frog blood with Grower's solution and then counted red blood cell in 5 red blood cells square of the improved Neubauer counting chamber (Campbells, 1995). The hemoglobin concentration was determined by the cyanomethemoglobin method (Ritchie et al, 1994).

Scanning electron microscopic (SEM) technique: Blood sample was dropped in 2.5% glataraldehyde in 0.1 M phosphate buffer, pH 7.2 overnight at 4 °C and washed in the same buffer. Samples were postfixed with 1% osmium tetroxide for 2 hours, rinsed with distilled water, dehydrated in 20%, 40%, 60%, 80%, 100%, 100% acetone and left to air dry. Gold coated blood films were examined under a SEM (JSM 6460LV).

Results and Discussion

The hematological values and blood cell sizes of balloon frogs are shown in Tables 1 and 2. Blood cell characteristics of ballon frogs examined under light microscopic and SEM are shown in figures 1 and 2.

Conclusion

Lastly, blood cell characteristics of balloon frogs were similar to Asian painted frog (Ponsen et al, 2007) and those of other species of frogs that reported by Desser (2001) and Wojtaszek and Adamowicz (2003).

Acknowledgment

We would like to thank to the Mahasarakham University Research and Development Unit, Mahasarakham University for support this project.

References

- Campbell TW. Avian Hematology and Cytology. *Iowa State University Press*, Ames, Iowa 1995.
- 2. Desser, SS. The blood parasites of anurans from Costa Rica with reflections on the taxonomy of their trypanosomes. *J. Parasitol* 2001, 87(1): 152-160.
- Ponsen S, Narkkong N-A, Pamok S, Sappaso K, Aengwanich W. Hematological values and morphological observation of blood cells in Asian painted frogs, Kaloula pulchra 1831. Proceeding in The First International Conference on Sustainable Animal Agriculture and Developing Countries (SAADC 2007) at Yunnan Agricultural 27th-30th University, China, September, 2007, 345-348.
- 4. Ritchie, BW, Harrison G.J, Harrison RL, Avian Medicine: Principle and Application. Wingers Publishing, Inc, Florida 1994.
- 5. Wojtaszek J, Adamowicz A. Haematology of the fire-bellied toad, *Bombina bombina* L. *Comp. Clin. Path* 2003, 12: 129-134.

Table 1. Hematological values (mean \pm SE) of balloon frogs (n=18).

Hematological value	Mean ± SE
PCV(%)	26.94 ± 1.42
HB(g/dL)	8.62 ± 0.70
RBC ($x10^6$ cell/ μ l)	1.04 ± 0.18
$WBC(x10^3 \text{ cell/}\mu\text{l})$	1.37±0.16
MCV (fL)	409.29±78.17
MCH (pg)	142.11±34.18
MCHC (g/dL)	32.96±13.15
Lymphocyte (%)	41.62±3.07
Monocyte (%)	22.77±1.89
Heterophil (%)	26.27±2.25
Eosinophil (%)	1.07 ± 0.29
Basophil (%)	8.27±0.85

PCV=packed cell volume; HB=hemoglobin concentration; RBC=red blood cell; WBC=white blood cell; MCV=mean corpuscular volume; MCH=mean corpuscular hemoglobin; MCHC=mean corpuscular hemoglobin concentration

Table 2. Cell sizes (mean \pm SE) of balloon frogs (n=18).

Blood cell size (µm)	Mean ± SE
Erythrocyte: length	15.42 ± 1.04
: width	11.47 ± 0.82
: nucleus length	6.06 ± 0.78
: nucleus width	4.02 ± 0.45
Lymphocyte	8.56 ± 2.74
Monocyte	13.89 ± 3.34
Heterophil	13.76 ± 3.59
Eosinophil	15.00 ± 7.08
Basophil	6.90 ± 2.03
Thrombocyte	12.29 ± 2.52

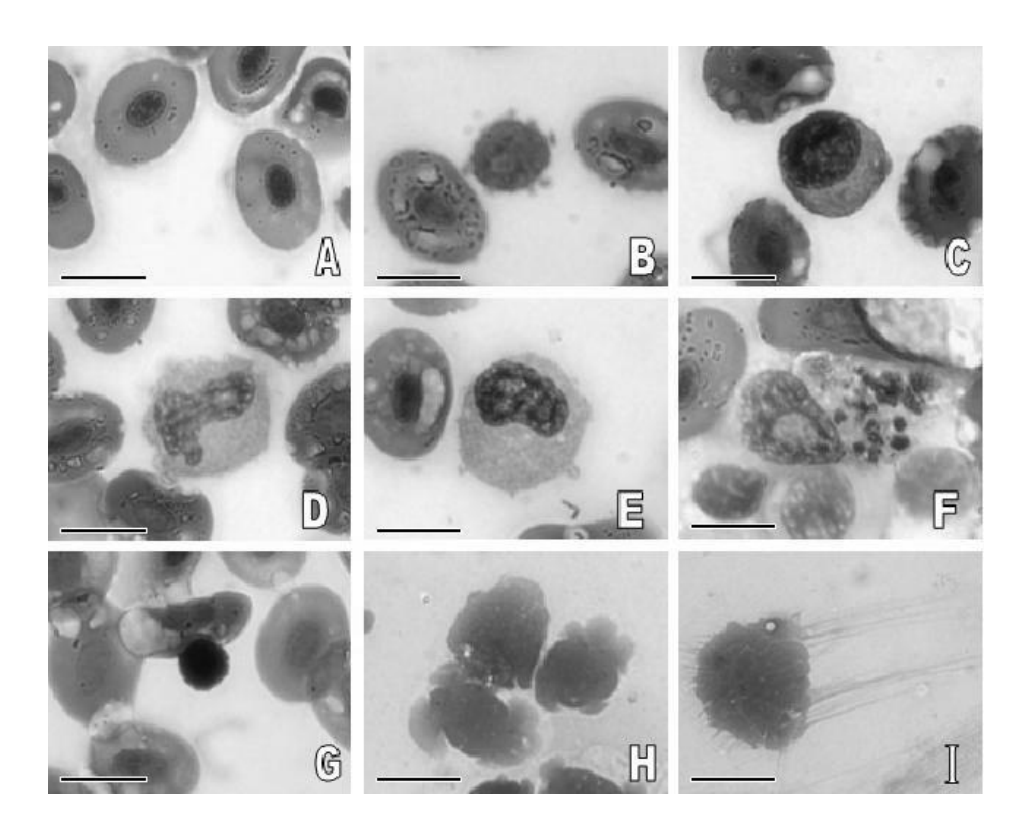


Fig. 1 LM micrographs of balloon frog blood cells (A, Erythrocyte; B, lymphocyte; C, monocyte; D-E, heterophil; F, eosinophil; G, basophil; H-I, thrombocyte; Geimsa-Wright's stain, bar = 10 μ m).

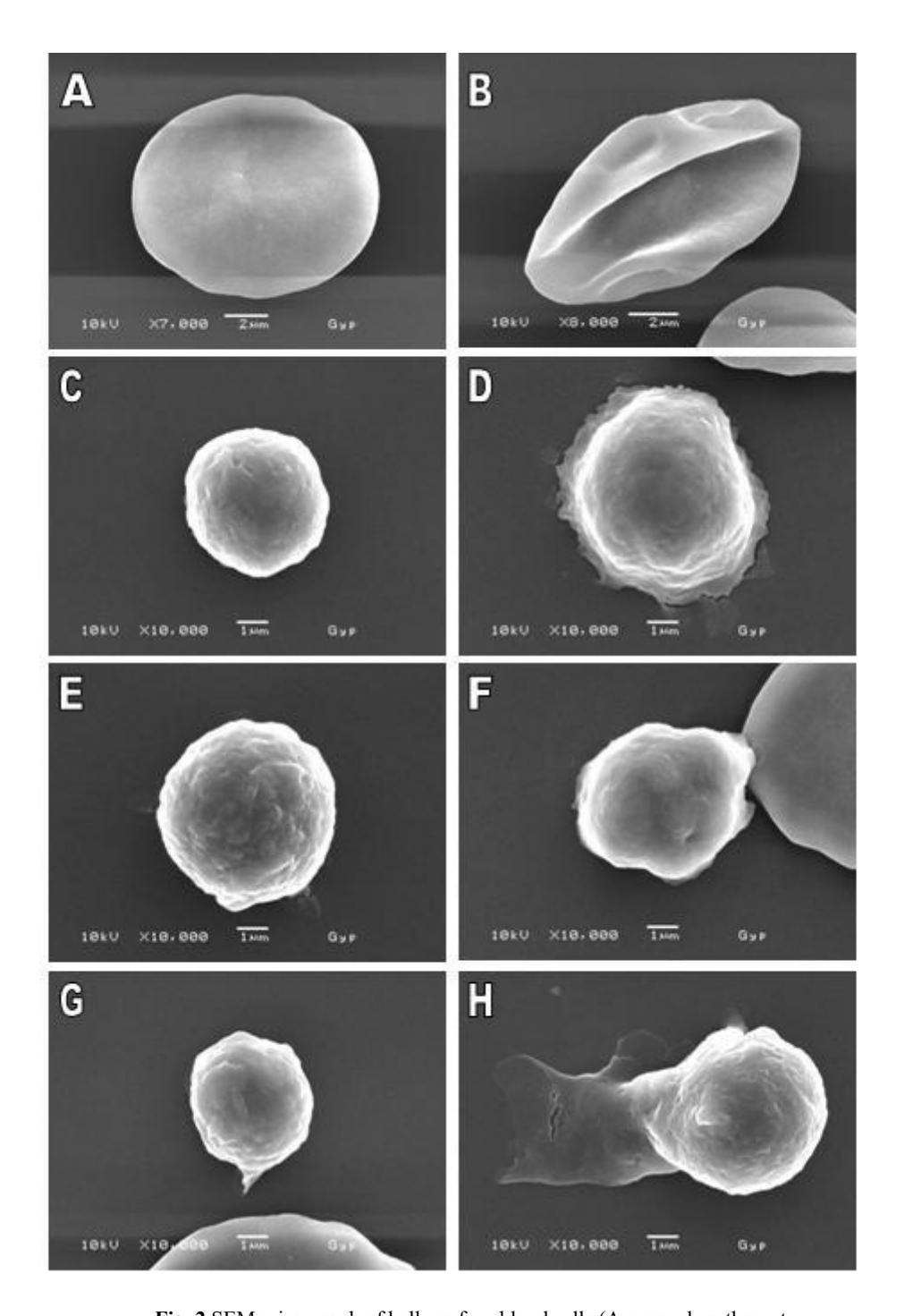


Fig. 2 SEM micrograph of balloon frog blood cells (A, normal erythrocyte; B, abnormal erythrocyte C, lymphocyte; D, monocyte; E, heterophil; F, eosinophil; G, basophil; H, thrombocyte; from A,B bar = 2 μ m and C-H, bar = 1 μ m)

Morphological Changes of Rice Starch during Grain Development

Pachongchit Poochinya 1*, Onanong Naivikul², Yupadee Poapun¹, Patcharee Umrung¹

- Scientific Equipment Center, Kasetsart University Research Development Institute
- ² Faculty of Agro-Industry, Kasetsart University

e-mail: psdpcc@ku.ac.th

Abstract

Microscopic examination of the developing rice grains provides information on morphology and composition, which influences processing behavior of the grains. PathumThani1 rice variety was studied. Maturation period of rice seeds was about 30 days after flowering. Scanning electron microscopy and light microscopy were used to examine development of rice grains in the early broom, milky, dough, yellow ripe, and mature stages. Starch granule size increased during grain development. The size of the granule increased most rapidly during 10-18 days after flowering. Starch was present essentially only in the endosperm cells of mature brown rice, where it existed as compound polyhedral granules 3 to 5 μ m in size. The cluster of starch granules within an amyloplast was spherical to ellipsoidal in shape. Rice starch was very tightly packed in the endosperm cells, and the starch granules had sharp edges.

Background

The rice spikelet consists of a single floret because the spikelet meristem is converted into a floret meristem after producing two pairs of sterile glumes. Rice florets comprise lemma, palea and three kinds of organs: two lodicules (pedals), six stamens and one pistil constituted by a single carpel (Itoh et al., 2005). Flowering in rice includes the opening of the palea and lemma, shedding of pollen by the anthers, and closing of the palea and lemma. The floret remains open for at least 30 min. Generally, florets open in the morning. It takes about 7 days for all spikelets in a panicle to open. Pollination takes place before or as the florets open, and fertilization is completed 30 min after pollination. Rice is essentially selfpollination. After fertilization, the rice caryopsis develops much faster in the longitudinal than in the transverse axis. It attains full length by 4 days after flowering (DAF), maximum width by 14 DAF, and maximum thickness by 21 DAF. The consistency of the endosperm goes through progressive stages, termed milky, dough, yellow, and mature (Juliano, 1985). During grain development, produced from photosynthesis is then transported in the phloem to the developing grains. Starch accumulates in the rice grain during the grainfilling period. Its deposition involves a suite of enzymes and several processes. (Ishimaru et al., 2003; Fitzgerald, 2004).

The aims of this study were to establish the pattern of starch development in the early broom stage, milky, dough, yellow ripe, and mature stages.

Materials and Methods

Sample

Samples of developing rice grains (*Oryza sativa* L., variety Pathum Thani 1) were collected from 4 to 28 days after flowering at 4-day intervals from Chachoengsoa Service Center for Crops and Production Resources, Chachoengsoa Province, Thailand. The grains were cooled to 0 ° C in an ice bath immediately after sampling and were stored at -20 ° C until used for analysis.

Sample Preparation for Electron and Light Microscopic Studies

Early broom and milky stages of rice seeds were cut into halves with a razor blade. Dough and mature stages, rice grains were manually snapped in two parts in the transverse direction. The fractured grain was mounted on aluminum stub using double-sided adhesive tape, with the broken surface oriented upwards. All specimens were stored in desiccator about a week. The specimens later were sputter coated with gold and viewed under a JSM 5600 LV (JEOL, Japan) scanning electron microscope at an accelerating voltages of 10 kV. For light microscopy, the grains were viewed under ZEISS stereoscopic microscope.

Results and Discussion

The developing grains grew very rapidly during the first ten days after flowering. Between 4 and 10 days after flowering the grain was sometimes called 'Water-ripe' or 'Pre-milk'. Milky stage, the grain started to fill with a white, milky liquid. The panicle looked green and started to bend. Dough stage, the milky portion of the grain first

turned into a soft dough and later a hard dough. The grains in the panicle began to change from green to yellow. Mature stage, the individual grain was mature, fully development, hard and had turned yellow (figure 1). Pigments in coloured rices were in the pericarp or the seed coat. The green colour was dued to chloroplasts in the 'cross cell' layer. Starch granules were first noticed in the endosperm cells of the four-day grain. The size of the granule increased most rapidly during the period 10-18 days after flowering. Individual starch granules increased in size from 3 to 5 m during grain development (figure 2).

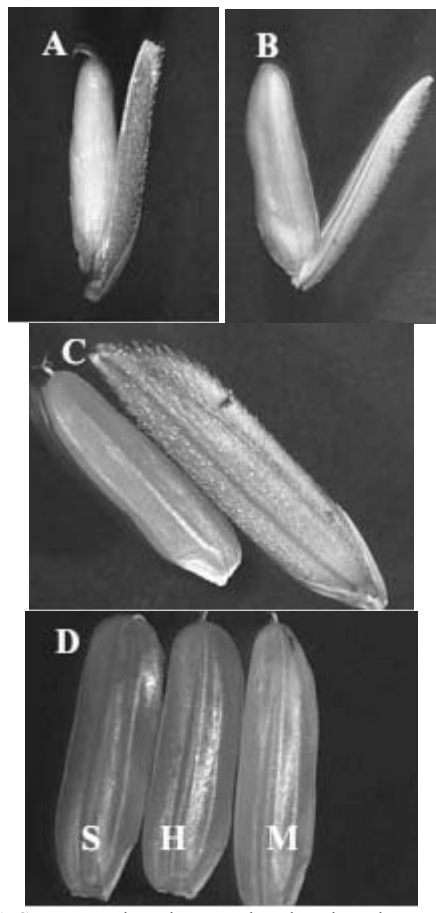


Fig. 1 Stereoscopic micrographs showing the stages of grain development. A: Early broom (4-10 DAF), B: Milky stage (14-15 DAF), C: Soft dough stage (17-18 DAF), D: Soft dough stage, S, (17-18 DAF) Hard dough stage, H, (20-23 DAF) and Mature stage, M, (28-30 DAF).

Mature grain became hardened and translucent as it lost moisture. The starch granules had sharp edges (figure 3).

Conclusion

Starch granules of rice were small, about 3-5 μm in diameter, and each granule was angular. The granules were compound. Each compound starch granule was polyhedral and contained many individual granules. Starch accumulated in the rice grain during the grain-filling period. Its deposition involved a suite of enzymes and several processes. During starch synthesis, sucrose produced from photosynthesis was transported in the phloem to the developing grains. The first process was the acquisition of the precursor sugars. The second process was the synthesis of the amylose and the amylopectin. The third process was the starch granules formation. The fourth process was the compound starch granules formation. The pattern of the developing rice grain in the early broom, milky, dough, yellow ripe, and mature stages were established in series of the starch synthesis. Starch granules size increased during grain development. The size of the granule increased most rapidly during the period 10-18 days after flowering. The cluster of starch granules within an amyloplast is spherical to ellipsoidal in shape. Rice starch was very tightly packed in the endosperm cells and the starch granules had sharp edges.

Acknowledgment

Chachoengsoa Service Center for Crops and Production Resources, Chachoengsoa Province, Thailand, is gratefully thanked for voucher specimen of Pathum Thani 1 rice variety.

References

- 1. Fitzgerald, M. Rice: Chemistry and Technology Third Edition. *American Association of Cereal Chemists, Inc. St. Paul, Minnesota* 2004, 109-162.
- 2. Ishimaru, T., Matsuda T., Ohsugi R. and Yamagishi T. Morphological development of rice caryopses located at the different positions in a panicle from early to middle stage of grain filling. *Functional Plant Biology* 2003, 30: 1139-1149.
- 3. Itoh, J.I., Nonomura K.I., Ikeda K., Yamaki S., Inukai Y., Yamagishi H., Kitano H. and Nagato Y. Rice plant development: from zygote to spikelet. *Plant Cell Physiology* 2005, 46(1): 23-47.
- 4. Juliano, B.O. and Bechtel D.B. Rice: Chemistry and Technology Second Edition. *American Association of Cereal Chemists, Inc. St. Paul, Minnesota*, 1985, 17-58.

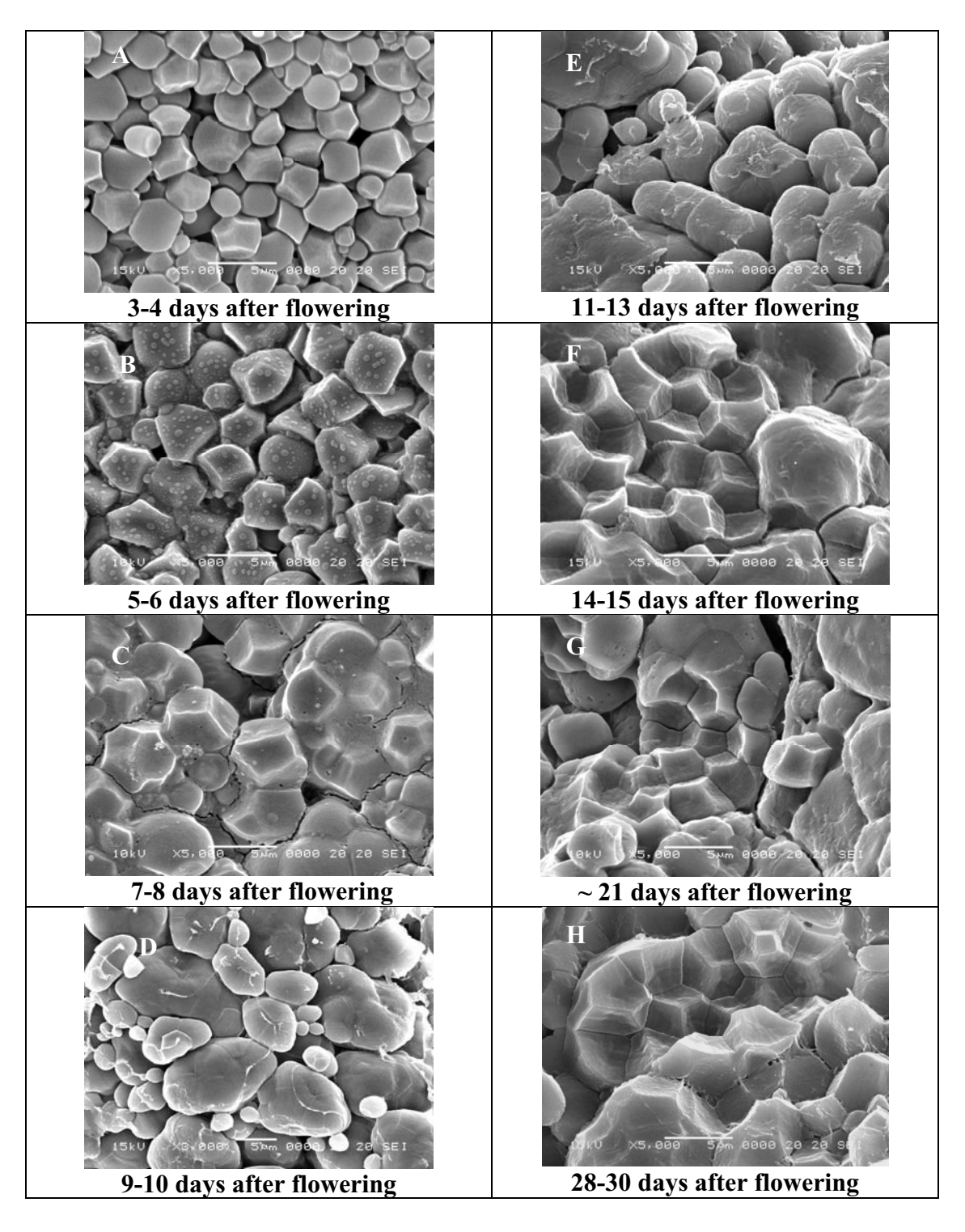


Fig. 2 Scanning electron micrographs of starch granules showing the pattern of starch granule formation from individual starch granule to compound starch granule in the amyloplast.

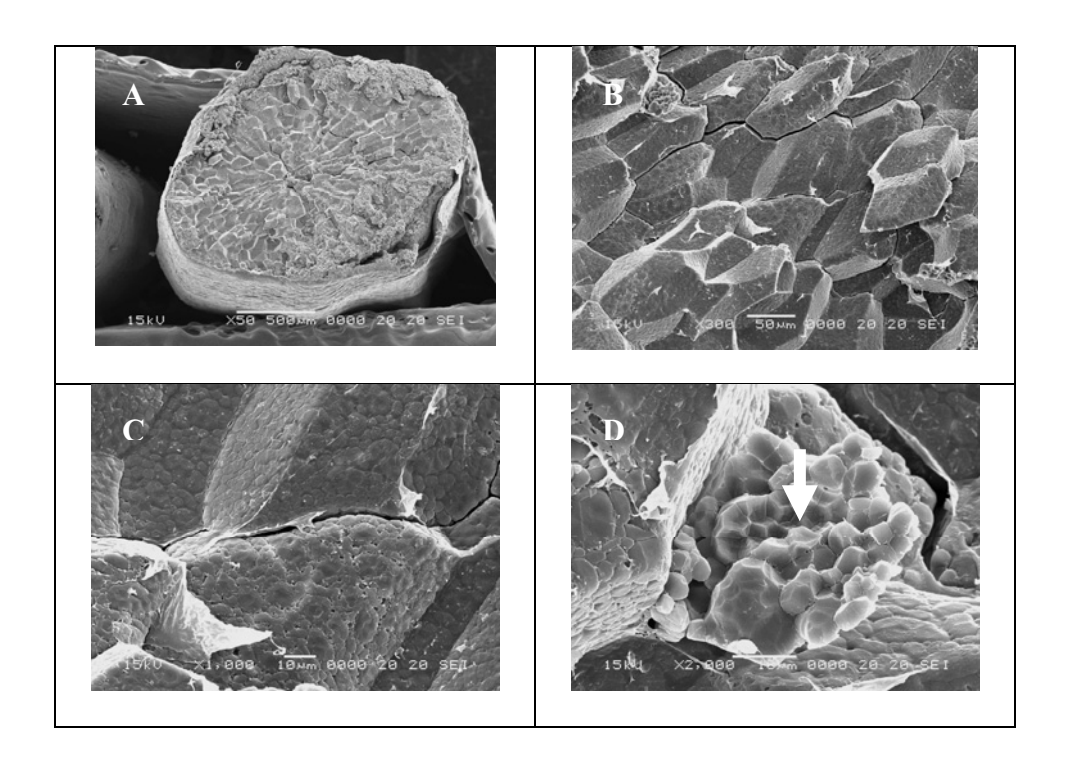


Fig. 3 Entire fracture face of the mature grain showing the starchy endosperm cells elongated radially on cross-sectional view (A) and filled with compound starch granules (B,C). D, the compound amyloplasts broken open, clearly revealing at least 16 single granules (arrows) inside the compound structure.